

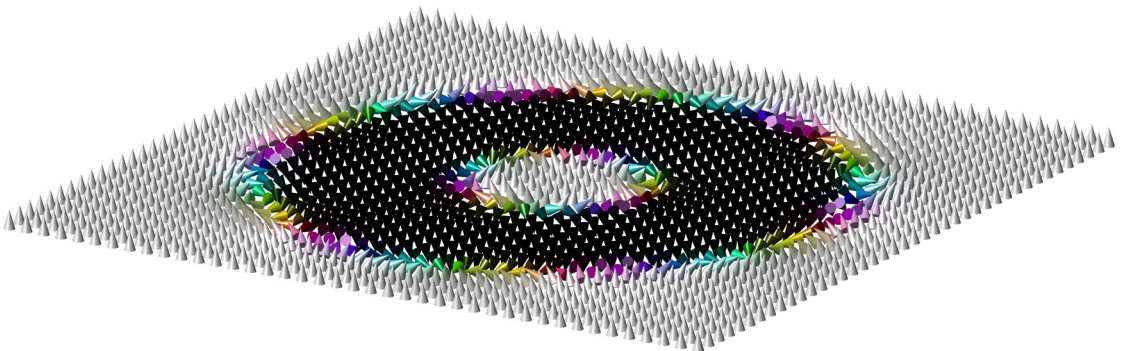


Doctoral Thesis in Physics

Numerical solutions to non-linear inhomogeneous problems in Superconductivity

From sphalerons to multi-band boundary states and
spontaneous magnetic fields

ANDREA LUDOVICO BENFENATI



Numerical solutions to non-linear inhomogeneous problems in Superconductivity

From sphalerons to multi-band boundary states and spontaneous magnetic fields

ANDREA LUDOVICO BENFENATI

Academic Dissertation which, with due permission of the KTH Royal Institute of Technology, is submitted for public defence for the Degree of Doctor of Philosophy on Tuesday the 24th May 2022, at 2:00 p.m. in FR4, Roslagstullsbacken 33, Stockholm

© Andrea Ludovico Benfenati

ISBN 978-91-8040-216-3
TRITA-SCI-FOU 2022:14

Printed by: Universitetsservice US-AB, Sweden 2022

Abstract

This thesis is a compilation of theoretical works focused on simulating and studying open questions regarding single and multiband superconductivity. In the last decades, with the discovery of multiband superconductors, the spectrum of potential applications has greatly widened. Superconductors are not only employed to realize dissipationless current carrying devices, but are used to construct quantum-based measurement instruments, such as single photon detectors as well as superconducting qubits. The properties of superconductors, as critical temperatures and vortex nucleation barriers are of key importance for applications, and still poorly understood. They are strongly affected by the physics of the boundaries, as well as by the sample's geometry and by the presence of impurities. The open questions can be answered with new theoretical methods, which can then guide and optimize the construction process of superconducting devices, which constitutes a crucial challenge today.

There are several models that can be utilized to describe superconductors, from the microscopic Bardeen Cooper Schrieffer theory, up to the macroscopic Ginzburg Landau models. Each of these theories carries advantages and limitations, making it impossible to rely only on a specific model. In this thesis we utilize microscopic and macroscopic models to answer the following questions:

1. How can we determine the free energy barriers to vortex nucleation in single band and multiband superconductors without relying on uncontrolled approximations?
2. What are the properties of the superconducting states which spontaneously break time reversal symmetry?
3. How do boundaries and interfaces influence the critical temperatures of superconductors?

We answer these questions in eight papers, which we shortly summarize in the following.

In Paper 1, *Magnetic signatures of domain walls in $s + is$ and $s + id$ superconductors: Observability and what that can tell us about the superconducting order parameter*, we consider an effective two-band anisotropic Ginzburg Landau model, describing a superconductor breaking time reversal symmetry. There is high interest on spontaneous time reversal symmetry breaking due to recent muon-spin rotation experiments [1, 2], claiming to measure spontaneous magnetic field in Fe-based superconductors such as $\text{Ba}_{1-x}\text{K}_x\text{Fe}_2\text{As}_2$. However, the symmetry of the superconducting order parameters remains undetermined, and the most promising candidates are $s + is$ and $s + id$ states. In the work, we obtain solutions for domain walls within the Ginzburg Landau model. By studying the spontaneous magnetic signatures of domain walls, having different orientations with respect to the crystalline axes, for both $s + is$ and $s + id$ order parameters, we demonstrate their

differences and propose a procedure to infer the order parameter's symmetry from magnetic field measurements.

In Paper 2, *Vortex nucleation barrier in superconductors beyond the Bean-Livingston approximation: A numerical approach for the sphaleron problem in a gauge theory*, we address the long standing problem of calculating the energy barriers for the vortex nucleation in a superconductor. The only available tool to do so, was the Bean-Livingston theory, which relies on uncontrollable approximations. This does not allow to take into account the non-linear nature of the Ginzburg Landau model, or the presence of impurities and surface roughness. Therefore, we develop the *gauged string method*, a gauge invariant numerical framework, based on the simplified string method [3], which enables us to accurately compute the minimum free energy path for the vortex nucleation. Moreover, we present a study of how the nucleation energy barrier changes in the presence of impurities and surface roughness.

In Paper 3, *Vortex nucleation barriers and stable fractional vortices near boundaries in multicomponent superconductors*, we extend the gauged string method to multiband superconductors, where the energy landscape is much broader than in the single band case, and the number of possible processes is higher. In multiband superconductors the topological excitations are fractional vortices, which once bounded, form composite vortices. Fractional vortices are energetically unfavorable, as they are associated to an energy cost which scales logarithmically with the system size. Once they bind and form a composite vortex, the extra energy cost is canceled. However, it was previously shown in the London model that fractional vortices can be stabilized near boundaries. In this paper, we study the energy barriers for the nucleation of fractional vortices, and for the formation composite vortices. Moreover, we show how the presence of anisotropies can influence such barriers. Then we study how the same processes are influenced by the interband Josephson interactions. By using the gauged string method, we demonstrate how the fractionalized nucleation process results in multiple saddle points and intermediate metastable configurations.

In Paper 4, *Boundary effects in two-band superconductors*, we study microscopically the behavior of the superconducting order parameters near the boundaries of a two band *s*-wave superconductor. We describe the system using a tight binding Bardeen Cooper Schrieffer model with interband interaction. We show the existence of surface states, and calculate how the difference between bulk and surface critical temperatures depends on the strength of the interband coupling. Then, we focus the analysis on weak interband interactions to show, at the level of a fully microscopic theory, how the variations of the gaps near the boundaries occur with multiple length scales.

In Paper 5, *Spontaneous edge and corner currents in $s+is$ superconductors and time-reversal-symmetry-breaking surface states.*, we consider a three band superconductor, described with a microscopic tight binding Bardeen Cooper Schrieffer model with interband interaction. In the current classification scheme, an *s + is* state is a non-topological and non-chiral state, which does not exhibit topological surface

states and therefore no spontaneous surface currents. In the article, we consider a system where the three bands have slightly different intraband pairing potential but the same interband coupling, resulting in slightly asymmetric bands. We show that, as the temperature is increased, the state which spontaneously break time reversal symmetry becomes localized near the sample boundaries, and generate spontaneous magnetic signatures. Finally, we show how, by changing the sample geometry, the magnetic signatures can be enhanced. We underline that, this phenomenon is not a general property of time reversal symmetry breaking states, but can account for the presence of spontaneous magnetic fields in $s + is$ superconductors and cannot be predicted using the macroscopic Ginzburg Landau theory. Moreover, the paper shows that spontaneous surface currents can arise for non-topological reasons.

In Paper 6, *Demonstration of $\mathbb{C}P^2$ skyrmions in three-band superconductors by self-consistent solutions to a Bogoliubov-de-Gennes model*, we continue the study of three component $s+is$ superconductors, described using a microscopic tight binding Bardeen Cooper Schrieffer model. In this work, we consider three symmetric bands, and we study the $\mathbb{C}P^2$ skyrmionic topological excitations of the system. We present not only the configurations of the superconducting order parameters, but also the respective magnetic field and density of states. Moreover, the simulation of $\mathbb{C}P^2$ skyrmions in superconductors, described a with fully microscopic model, had not been done before. In the context of superconductivity, $\mathbb{C}P^2$ skyrmion solutions were previously described only within the phenomenological macroscopic Ginzburg-Landau theory [4, 5].

In Paper 7, *Pair-density-wave superconductivity of faces, edges, and vertices in systems with imbalanced fermions* we analyze the boundary effects in superconductors exhibiting Fulde-Ferrell-Larkin-Ovchinnikov states. We do so by employing and comparing Bogoliubov-de-Gennes and Ginzburg Landau formalisms. We show that, within the Ginzburg Landau theory, in a three dimensional superconductor, there is a sequence of phase transitions as the temperature increases. Then, we perform the same sequence of simulations for two dimensional samples described using the Bogoliubov-de-Gennes formalism, showing the same sequence of phase transitions.

In Paper 8, *Elevated critical temperature at BCS superconductor-band insulator interfaces*, we study the physics of interfaces between a superconductor, described using a tight-binding mean field Hamiltonian, and a band insulator. We limit the study to one-dimensional samples and demonstrate that, within certain parameter ranges, it is indeed possible to enhance the critical temperature in the vicinity of the interface. This occurs without changing the strength of the superconducting-pairing interaction. Then we present the parameters regimes in which the near-interface critical temperature exceeds the critical temperature of a conventional superconductor-vacuum interface.

Sammanfattning

Denna avhandling är en sammanställning av teoretiska arbeten med fokus på att simulera och studera öppna frågor angående enbands- och flerbands-supraledning. Under de senaste decennierna, med upptäckten av flerbands-supraledare, har antalet potentiella tillämpningar ökat avsevärt. Supraledare används inte bara för att realisera resistansfria elektriska ledare, utan används i kvantbaserade mätinstrument, som till exempel enfotondetektorer och supraledande kvantbitar.

Egenskaper som kritiska temperaturer och virvel-energi-barriärer, är av huvudsaklig betydelse för tillämpningar, och fortfarande dåligt förstådda. De påverkas starkt av gränsernas, såväl som av supraledarens geometri och av förekomsten av föroreningar. Dessa frågor kan besvaras med nya teoretiska metoder, som sedan kan vägleda och optimera konstruktionsprocessen av supraledande enheter, vilket utgör en avgörande utmaning idag.

Det finns flera modeller som kan användas för att beskriva supraledare, från den mikroskopiska Bardeen Cooper Schrieffer-teorin, till de makroskopiska Ginzburg Landau-modellerna. Var och en av dessa teorier har fördelar och begränsningar, vilket gör det omöjligt att bara förlita sig på en specifik modell. I denna avhandling använder vi både mikroskopiska och makroskopiska modeller för att svara på följande frågor:

1. Hur kan vi bestämma fri-energi-barriärer för virvelkärnbildning i enbands- och flerbands-supraledare utan att förlita oss på okontrollerbara approximationer?
2. Vilka egenskaper har supraledande tillstånd som spontant bryter tidsinversionssymmetri?
3. Hur påverkar ränder och gränssnitt supraledares kritiska temperatur?

Vi besvarar dessa frågor i avhandlingen med åtta artiklar; dessa artiklar sammanfattas nedan.

I artikel 1, *Magnetic signatures of domain walls in $s + is$ and $s + id$ superconductors: Observability and what that can tell us about the superconducting order parameter*, betraktar vi en Ginzburg-Landau-modell, som beskriver en anisotrop tvåbandssupraledare som spontant bryter tidsinversionssymmetrin. Det finns ett stort intresse för det spontana tidsinversionssymmetribrottet på grund av nyligen genomförda muon-spin-rotationsexperiment [1, 2], som påstår sig mäta spontana magnetfält i järnbaserade supraledare som $\text{Ba}_{1-x}\text{K}_x\text{Fe}_2\text{As}_2$. Supraledarnas symmetri förblir dock obestäm, och de mest lovande kandidaterna är tillstånden $s + is$ och $s + id$. I arbetet får vi fram lösningar för domänväggar inom Ginzburg-Landau modellen. Genom att studera de spontana magnetiska signaturerna för domänväggar, med olika orienteringar, för både $s + is$ och $s + id$ ordningsparametrar, visar vi deras skillnader och föreslår en procedur för att härleda ordningsparameterns symmetri från magnetfältsmätningar.

I artikel 2, *Vortex nucleation barrier in superconductors beyond the Bean-Livingston approximation: A numerical approach for the sphaleron problem in a gauge theory*, tar vi upp det långvariga problemet med att beräkna energibarriärerna för virvelkärnbildning i en supraledare. Det enda tillgängliga verktyget för att göra det var Bean-Livingston-teorin, som bygger på okontrollerbara approximationer. Det tillåter inte att ta hänsyn till den icke-linjäriteter i Ginzburg Landau-modellen, såväl som närvaron av föroreningar och ytojämnhet. Därför utvecklar vi den *gauged string method*, ett gaugeinvariant numeriskt ramverk, baserat på *simplified string method* [3], som gör det möjligt för oss att exakt beräkna den minsta fria energivägen för virvelkärnbildning. Dessutom presenterar vi en studie av hur kärnbildningsenergi-barriären förändras i närvaro av föroreningar och ytojämnhet.

I artikel 3, *Vortex nucleation barriers and stable fractional vortices near boundaries in multicomponent superconductors*, tillämpar vi *gauged string method* på flerbandsupraledare, där energilandskapet är mycket större än i enbandsfallet, och antalet möjliga processer är större. I flerbandsupraledare är de topologiska excitationerna fraktionerade virvlar, som binder ihop och bli en kompositvirvell. Fraktionerade virvlar är energimässigt ogynnsamma, eftersom de är förknippade med en energikostnad som skalas logaritmiskt med systemets storlek. När de har bundits bildar de en kompositvirvel utan denna extra energikostnad. Tidigare har det dock visat sig, i London-modellen, att fraktionerade virvlar kan stabiliseras nära systemens ränder. I den här artikeln studerar vi energibarriärerna för kärnbildning av fraktionerade virvlar och kompositvirvlar. Dessutom visar vi hur anisotropi kan påverka sådana barriärer. Sedan studerar vi hur samma processer påverkas av Josephson-samverkan mellan banden. Genom att använda *gauged string method* demonstrerar vi hur den fraktionerade kärnbildningsprocessen resulterar i flera sadelpunkter och mellanliggande metastabila konfigurationer.

I artikel 4, *Boundary effects in two-band superconductors* studerar vi mikroskopiskt beteendet av de supraledande ordningsparametrarna nära ränderna för en tvåbands *s-wave* supraledare. Vi beskriver systemet med en Bardeen Cooper Schrieffer-gittermodell med samverkan mellan banden. Vi visar förekomsten av yt-tillstånd och beräknar hur skillnaden mellan bulk- och ytkritiska temperaturer beror på styrkan hos bandsamverkan. Sedan fokuserar vi analysen på svaga bandsamverkningsför att visa, på nivån av en helt mikroskopisk teori, hur variationerna av ordningsparametrarna nära gränserna uppstår med flera längdskalor.

I artikel 5, *Spontaneous edge and corner currents in $s + is$ superconductors and time-reversal-symmetry-breaking surface states.*, betraktar vi en trebandsupraledare, beskriven med en mikroskopisk Bardeen Cooper Schrieffer-gittermodell med samverkan mellan banden. I det nuvarande klassificeringsschemat är ett *s + is*-tillstånd ett icke-topologiskt och icke-kiralt tillstånd, som inte uppvisar topologiska yttillstånd och därför inga spontana ytströmmar. I verket betraktar vi ett system där de tre banden har något olika parbildningsinteraktion men samma bandsamverkan, vilket resulterar i något asymmetriska band. Vi visar att när temperaturen höjs blir tillståndet, som bryter tidsinversionsymmetri spontant, lokaliserat nära provgränserna och genererar spontana magnetiska signaturer. Slutligen visar vi hur

de magnetiska signaturerna kan förstärkas genom att ändra provgeometrin. Vi understryker att detta fenomen inte är en allmän egenskap hos supraledare som bryter tidsinversionsymmetri, utan kan förklara närvaron av spontana magnetfält i $s + is$ supraledare, och kan inte förutsägas med hjälp av makroskopisk Ginzburg Landau-teori. Arbetet visar att spontana ytströmmar kan uppstå av icke-topologiska skäl.

I artikel 6, *Demonstration of $\mathbb{C}P^2$ skyrmions in three-band superconductors by self-consistent solutions to a Bogoliubov-de-Gennes model*, fortsätter vi studien av treband $s + is$ supraledare, beskrivna med hjälp av en mikroskopisk Bardeen Cooper Schrieffer-gittermodell. I detta arbete undersöker vi tre symmetriska band, och vi studerar $\mathbb{C}P^2$ skyrmioner - topologiska excitationer i systemet. Vi presenterar inte bara konfigurationerna av parametrarna för supraledande ordning, utan också magnetfält och tillståndstäthet. Dessutom hade simuleringen av $\mathbb{C}P^2$ skyrmioner i supraledare, beskrivna en helt mikroskopisk modell, inte genomfört tidigare. I samband med supraledning har $\mathbb{C}P^2$ skyrmionlösningar tidigare beskrivits bara i den makroskopiska Ginzburg-Landau-teorin [4, 5].

In artikel 7, *Pair-density-wave superconductivity of faces, edges, and vertices in systems with imbalanced fermions* analyserar vi gränseffekterna i supraledare med Fulde-Ferrell-Larkin-Ovchinnikov tillstånd. Vi gör det genom att använda och jämföra Bogoliubov-de-Gennes och Ginzburg-Landau formalism. Vi visar att det inom Ginzburg-Landau-teorin, i en tredimensionell supraledare, finns en sekvens av fasövergångar när temperaturen ökar. Sedan utför vi samma sekvens av simuleringar för tvådimensionella prover som beskrivs med Bogoliubov-de-Gennes-formalismen, som visar samma sekvens av fasövergångar.

I artikel 8, *Elevated critical temperature at BCS superconductor-band insulator interfaces* studerar vi fysiken för gränssnitt mellan en supraledare, beskriven med hjälp av en Bardeen Cooper Schrieffer-gittermodell och en bandisolator. Vi begränsar studien till endimensionella prover och visar att det, inom vissa parameterintervall, är möjligt att öka den kritiska temperaturen i närheten av gränssnittet. Detta sker utan att ändra styrkan hos supraledares parbildningsinteraktion. Sedan presenterar vi parametrarnas regimer där den kritiska temperaturen nära gränssnittet överstiger den kritiska temperaturen för ett konventionellt supraledare-vakuumgränssnitt.

Preface

This thesis is the result of my research at the Department of Physics from September 2018 to May 2022.

The first part of the thesis briefly summarizes the research field, introduces some fundamental concepts, and outlines the numerical work I developed through my PhD.

The second part contains the results I obtained in my research activity, presented in the form of eight papers.

My PhD was supported by the Swedish Research Council Grants No. 2016-06122 and No. 2018-03659.

List of papers

The scientific papers included in this thesis are:

1. *Magnetic signatures of domain walls in $s + is$ and $s + id$ superconductors: Observability and what that can tell us about the superconducting order parameter* [6]
A. Benfenati, M. Barkman, T. Winyard, A. Wormald, M. Speight and E. Babaev
[Phys. Rev. B 101, 054507](#)
2. *Vortex nucleation barrier in superconductors beyond the Bean-Livingston approximation: A numerical approach for the sphaleron problem in a gauge theory* [7]
A. Benfenati, A. Maiani, F. N. Rybakov, E. Babaev
[Phys. Rev. B 101, 220505\(R\)](#)
3. *Vortex nucleation barriers and stable fractional vortices near boundaries in multicomponent superconductors* [8]
A. Maiani, **A. Benfenati**, E. Babaev
[arXiv:2111.01061](#)

4. *Boundary effects in two-band superconductors* [9]
A. Benfenati, A. Samoilenka, and E. Babaev
[Phys. Rev. B 101, 054506](#)

5. *Spontaneous edge and corner currents in $s + is$ superconductors and time reversal symmetry breaking surface states* [10]
A. Benfenati and E. Babaev
[Phys. Rev. B 105, 134518](#)

6. *Demonstration of CP^2 skyrmions in three-band superconductors by self-consistent solutions to a Bogoliubov-de-Gennes model* [11]
A. Benfenati, M. Barkman, and E. Babaev
[arXiv:2204.05242](#)

7. *Pair-density-wave superconductivity of faces, edges, and vertices in systems with imbalanced fermions* [12]
A. Samoilenka, M. Barkman, **A. Benfenati**, and E. Babaev
[Phys. Rev. B 101, 054506](#)

8. *Elevated critical temperature at BCS superconductor-band insulator interfaces* [13]
A. Samoilenka, M. Barkman, **A. Benfenati**, and E. Babaev
[arXiv:2201.11614](#)

The thesis author's contribution to the papers

1. In this paper I handled the overall research direction, wrote the paper and co-developed the code utilized to run the simulations together with Mats Barkman.
2. In this work, I supervised the work of the master student Andrea Maiani, and wrote the article.
3. In this paper, I am the correspondent author. My contribution consisted of assisting Andrea Maiani in the choice of the systems to study. Moreover, I provided insights on the theoretical model, and collaborated in the paper composition.
4. In this work, I handled the research on the topic, developed the code used for the simulations and wrote the article.
5. In this work, I handled the research on the topic, developed the code used for the simulations and wrote the article.
6. In this paper, I handled the research direction and wrote the paper together with Mats Barkman, moreover I developed the numerical framework enabling us to obtain the presented results.
7. My contributions to this paper consisted of the realization of the simulations in the Bogoliubov-de-Gennes formalism.
8. In this paper I contributed to the discussions on the topics and in the choice of the physical systems to simulate.

Acknowledgements

I would like to start by thanking my supervisor Egor Babaev. I am very grateful to him for giving me the opportunity to be in his research group as well as being always encouraging and enthusiast. I would also like to thank all the professors in the Condensed Matter Theory division that I met as a master student and got to know better through my PhD. A special thanks goes to Jens Bardarson, not only for being the pre-reviewer of this thesis and providing valuable feedback, but also for the countless discussions and coffee breaks, as well as for the amazing collaboration which lead to a fantastic Espresso machine in our division. A sincere thank you goes to all my colleagues, especially Robert Vedin, Julia Hannukainen, Ilaria Maccari, Mattias Jönsson, Albert Samoilenka, David Aceituno and Anton Talkachov, with whom I had meaningful discussions and always a great time. I am deeply grateful to Mats Barkman, who has been a great friend since I moved to Sweden, and the colleague whom I shared most of my research activity with. A special thanks goes to Daniel Qvarngård, colleague but especially great friend of mine, who thought me all the secrets of the Swedish culture, while appreciating the most iconic moments of Italy's contemporary history. Speaking about Italy, I would like to thank Maestro Bini and my long time friend Alessandro Prencipe, who, at this point, is probably offended that he had to read this far to be acknowledged. A huge thank you goes to my dearest friends Federico Baldassarre, Luca Guastoni and Marco Spanghero, who had been my "little Italy" and with whom I shared great moments since I moved to Sweden. I am also grateful to all my friends from ARF rowing club. Dulcis in fundo, I would like to thank my family, especially my sister Bianca, my mother Paola and my father Fabio. It is not easy to live two thousands kilometers far apart, but I always felt them close to me. They always supported me, encouraged me and backed my choices, I could not wish for more.

Contents

Abstract	iii
Sammanfattning	vi
Preface	ix
List of papers	ix
The thesis author's contribution to the papers	xi
Acknowledgements	xii
Contents	xiii
I Introduction and background material	1
1 Introduction	3
2 Classics never die: The Ginzburg-Landau Theory	5
2.1 The Ginzburg Landau Theory for a single band superconductor . . .	5
2.1.1 Equations of motion for a single band superconductor . . .	8
2.2 Type-II superconductors	14
2.2.1 Quantum vortices	14
2.3 Nucleation barriers in single band type-II superconductors	20
2.4 Type-I superconductors	24
2.5 Multiband GL theory	25
2.5.1 Fractional quantum vortices	26
2.5.2 Composite quantum vortices	27
2.5.3 Type 1.5 superconductivity	28
2.5.4 Josephson interaction	29
2.5.5 Time reversal symmetry breaking states	29
2.5.6 Domain walls	30
2.6 Spatially anisotropic GL theory	33
2.7 Research activity	35

3	Navigating uncharted energy landscapes: The gauged string method	37
3.1	The String Method: an overview	38
3.1.1	The simplified string method	39
3.1.2	The gauged string method	40
3.2	Application to a mechanical system	43
4	Safari in the microscopic world	47
4.1	The mean field theory	47
4.2	The variational approach	48
4.2.1	The Hubbard model	53
4.3	Multiband superconductivity	57
4.4	Chebyshev polynomial expansion	61
4.4.1	Chebyshev polynomials	61
4.4.2	BdG-Chebyshev decomposition	63
4.5	Research activity	66
5	Conclusion	69
6	Appendix	71
6.1	Details on Eq. 4.3.19	71
	Bibliography	73
II	Scientific Papers	85

Part I

Introduction and background material

Chapter 1

Introduction

Superconductivity is a state of matter, which is characterized by two main phenomena: the perfect diamagnetism, i.e., the complete screening of the magnetic field, and zero electrical resistance. The discovery of superconductivity dates back to 1911, when the dutch physicist Heike Kamerlingh Onnes, measured a sudden drop in the electrical conductivity of Mercury at the temperature of 4.2 K [14]. In 1933, Onnes was awarded the Nobel prize for the discovery of liquid Helium, which was a key element to study materials in their superconducting regime, which requires criogenic temperatures. The second hallmark of superconductivity, i.e., the perfect diamagnetism, also called Meissner effect, was discovered two decades later, in 1933 by Meissner and Ochsenfeld [15, 16]. Two more years were needed to obtain the first theoretical model accounting for the experimental results. In 1935, the brothers Fritz and Heinz London showed that the Meissner effect is a consequence of the minimization of the thermodynamic potential of the system [17]. The London equations became the first theoretical explanation of the perfect diamagnetism in superconductor. We need to fast forward to 1950 to record further significant advancements in the field, in the form of a rapid sequence of experimental and theoretical discoveries. E. Maxwell and C. A. Reynolds discovered that the critical temperature, at which the superconducting transition occurs, depends on the element's isotopic mass [18, 19], suggesting, for the first time, that the origin could lie in an electron-phonon interaction. At the same time, V. L. Ginzburg and L. D. Landau published the homonymous theoretical model describing conventional superconductors [20]. The Ginzburg Landau model was based on Landau's theory of second order phase transitions and was not microscopically justified. The first microscopic model for superconductivity was published in 1957 by J. Bardeen, L. Cooper and J. R. Schrieffer and named BCS theory after them [21]. The BCS theory relies on a phonon-electron interaction which, below the critical temperature, conveys the formation of electron pairs (Cooper pairs [21]) which are responsible for superconductivity. In 1972 Bardeen Cooper and Schrieffer were awarded the Nobel prize in Physics. Finally, in 1959 L. P. Gor'kov showed that, in the vicinity of the

critical temperature, the BCS theory could be reduced to the Ginzburg Landau model [22].

Three years after the publication of the BCS theory, it was understood that it was possible for a material to have more than one superconducting component. Two years later, the first multiband superconductor was theorised [23, 24]. The model relied on the presence of distinct Fermi surfaces yielding multiple gaps, with different critical temperatures. It took forty years to experimentally confirm the existence of multiband superconductors, with the first experimental evidence found in MgB_2 [25–28]. In 2004 multiband superconductivity was discovered in Iron-based compounds, which are now among the most common and numerous multiband superconductors [1, 2, 29–33]. Today single and multiband superconductors are among the main candidates for cutting edge technologies, such as quantum based sensors, e.g., single photon detectors, and qubits. The challenges entailed with such applications, as well as the complexity of the theoretical models, urge the development of reliable simulation frameworks which could assist the design of physical devices and clarify the origin of new phenomena, such as the presence of spontaneous magnetic fields.

In this thesis, we aim answering some questions that are relevant in the field of superconducting device modelling. We begin by focusing on the process of vortex nucleation in superconductors, in the context of the Ginzburg Landaus theory, and develop a numerical framework to calculate the nucleation energy barriers, with the possibility of accounting for different geometries, presence of impurities and surface roughness. Then, we switch to the microscopic BCS theory and investigate numerous phenomena, ranging from the structure of surface states in multiband superconductors to the formation of skyrmion topological excitations.

In Chapter 2 we present the Ginzburg Landau theory, for a single band and a multiband superconductor. Moreover, we describe the properties of Type-I, Type-II and Type-1.5 superconductors.

In Chapter 3 we describe the *gauged string method*, which we utilize to numerically determine the vortex nucleation energy barriers in superconductors. Finally, in Chapter 4, we derive the BCS theory for a superconductors starting from the mean field approximation of a quartic Hamiltonian. Then, we present the numerical framework which we developed.

Part II of this thesis contains all the papers I realised during my PhD.

Chapter 2

Classics never die: The Ginzburg-Landau Theory

2.1 The Ginzburg Landau Theory for a single band superconductor

In this section, we introduce the one-band Ginzburg Landau (GL) theory which describes a single component superconductor close to its critical temperature T_c . The Ginzburg-Landau theory [20] represents an extremely successful theoretical model able to provide a phenomenological description of superconductivity as well as a macroscopic, but microscopically-derived one [22]. The GL theory accounts for the formation of the electrically charged cooper-pair condensate, and describes its interaction with an external electromagnetic field, giving rise to the Meissner effect, i.e., a complete expulsion of the magnetic field from the bulk of the superconductor. Moreover, the GL theory fully accounts for the existence of *type-I* and *type-II* superconductors. The different behavior is described by a single parameter, conventionally called κ , whose value embeds the surface tension between normal and superconductive areas. If $\kappa < 1$, the surface tension is positive, allowing only the complete screening of the external magnetic field, as the inclusion of non-condensate areas is energetically unfavorable, yielding the Meissner state. In this condition, any external magnetic field $H < H_c$, where H_c is the critical field, is completely screened in the bulk. Above H_c the superconducting state is lost.

If the GL model has $\kappa > 1$ instead, the surface tension is negative, making normal zones in the bulk energetically favorable, giving rise to the appearance of vortices. These vortices, also named quantum vortices, are topological solitons, i.e., localized field solutions, with a well defined energy, a quantized magnetic flux and particle-like interactions. Each vortex can be fully described by its winding number (or topological charge) N . Vortices with same winding number repel each

other, while vortices with opposite winding attract each other and annihilate. In this situation, the relevant magnetic fields to describe the full phenomenology of the superconductor are two, namely H_{c1} and H_{c2} . For $H < H_{c1}$ the magnetic field is completely screened in the bulk. For $H_{c1} < H < H_{c2}$, quantum vortices nucleate from the boundaries and form a triangular lattice, known as Shubnikov phase [34]. The vortex-nucleation phenomenon can be seen as a nucleation barrier which needs to be overcome to allow the entrance of a vortex in the bulk. The transition between Meissner state and Shubnikov phase is first-order-like since both phases can have metastable survival. Finally, when $H > H_{c2}$ superconductivity is lost.

Let us consider a three dimensional superconductor, occupying a domain Ω ; its state is described by a complex-valued order parameter $\psi(\mathbf{r})$, whose free energy, expressed in dimensionless units, reads

$$F[\psi, \mathbf{A}] = F_N \tag{2.1.1}$$

$$+ \int_{\Omega} d^3x \left[\frac{1}{2} |(\nabla + iq\mathbf{A})\psi|^2 + a(T)|\psi|^2 + \frac{b(T)}{2} |\psi|^4 \right] + \int_{\mathbb{R}^3} d^3x \frac{(\nabla \times \mathbf{A})^2}{2}.$$

F_N is the free energy of the material when it is in the normal state, i.e., when the temperature exceeds the critical temperature. q is the charge of the condensate carriers, which couples the vector potential \mathbf{A} to the order parameter ψ . Finally, the coefficient a and b are, in general, temperature dependent and define the ground state of the model. The physical interpretation of the order parameter ψ is that $|\psi(\mathbf{r})|^2$ is proportional to the superconductor carrier density. It is important to note that the free energy expansion is carried up to the fourth order, which makes it justified as long as ψ is small, i.e., in the vicinity of the critical temperature T_c . The parameter κ we introduced above, depends on the model's parameters and we derive it in the next section. As we are considering only equilibrium solutions, where there is no time dynamics involved, we do not consider the electric potential. Since the considered GL model describes a second order phase transition, at the critical temperature the coefficient a needs to change sign, hence it will be of the form $a(T) = a_1(T - T_c)$. In this way, for $T < T_c$, having a non-zero $|\psi|$ will lower the energy, while at $T > T_c$ it will increase it. In this scenario b remains positive in the entire considered temperature range. Moreover the Ginzburg Landau theory fully accounts for all the results contained in the London theory of superconductivity.

As an example, we can consider a superconductor in the absence of vector potential \mathbf{A} . From Eq. 2.1.1 it is then clear that a uniform order parameter lowers the free energy. The free energy then becomes¹

$$F = F_N + a|\psi|^2 + \frac{b}{2}|\psi|^4. \tag{2.1.2}$$

¹Here we assume a unit volume, i.e., $\int_{\Omega} d^3x = 1$

To obtain the equations of motion for the order parameter we minimise the free energy $\frac{\partial F}{\partial |\psi|} = 0$, obtaining

$$(a + b|\psi_0|^2)|\psi_0| = 0, \quad (2.1.3)$$

which has $|\psi_0| = 0$ and $|\psi_0| = \sqrt{\frac{-a}{b}}$ as possible solutions. The first solution yields $F = F_N$ and therefore describes the material in its normal state. The second solution exists only for $a < 0$ and leads to

$$F = F_N - \frac{a^2}{2b}, \quad (2.1.4)$$

which is lower than the normal state. By studying the second derivative of the free energy, we can confirm that for $a < 0$, i.e., $T < T_c$ the superconducting state is the minimal energy state. If $T > T_c$ instead, the normal state $|\psi| = 0$ becomes the favoured one.

The phase transition

To analyse more precisely how the GL free energy functional describes a phase transition, let us leverage on the analytic nature of the a and b coefficients and expand them around the critical temperature, i.e.,

$$a(T) = a_0 + a_1(T - T_c) + a_2(T - T_c)^2 + \dots \quad (2.1.5)$$

$$b(T) = b_0 + b_1(T - T_c) + b_2(T - T_c)^2 + \dots \quad (2.1.6)$$

Moreover, given the relative freedom in the choice of these parameters, it is possible to assume $a_0 = 0$ and that b 's temperature dependence can be neglected. By inserting these expansions in Eq. 2.1.3 we obtain:

$$(a_1(T - T_c) + b_0|\psi_0|^2)\psi_0 = 0. \quad (2.1.7)$$

Hence, the only solution which allows for a non-trivial ground state, is for $T < T_c$ and yields

$$|\psi_0| = \sqrt{\frac{a_1(T_c - T)}{b_0}} \propto \sqrt{T_c - T}, \quad (2.1.8)$$

where the mean-field theory's characteristic temperature scaling is obtained. Every solution with this order parameter modulus minimises the free energy functional below the critical temperature. Since the order parameter is a complex-valued field, and the free energy minimization involves only the modulus, there is a global $U(1)$ symmetry that is spontaneously broken by the ground state.

Finally, the difference between the free energy of the superconducting state and of the normal state is $F - F_N = -a^2/(2b)$, and represents the amount of energy

needed to bring the system from superconducting to normal. One can use this to define the *thermodynamic critical field* H_c as the externally applied field able to destroy superconductivity by providing the system the required energy to transition to normal state. For this to happen, we need to fulfill

$$\frac{H_c^2}{2} = \frac{a^2}{2b} \quad \Rightarrow \quad H_c = \sqrt{\frac{a^2}{b}}. \quad (2.1.9)$$

This definition comes from a purely thermodynamic argument and does not take into account the orbital effects.

2.1.1 Equations of motion for a single band superconductor

Let us now derive the full equations of motion for a single band superconductor described by the free energy functional in Eq. 2.1.1. In this case, we allow also inhomogeneous solutions, and the order parameter has the structure $\psi(\mathbf{r}) = |\psi(\mathbf{r})|e^{i\theta(\mathbf{r})}$. Since the functional in Eq. 2.1.1 depends both on the order parameter and on the vector potential, we obtain two equations of motion. Let us begin by taking the functional derivative $\delta F/\delta\psi^* = 0$ which yields:

$$\frac{1}{2}(-i\nabla + q\mathbf{A})^2\psi + a\psi + b|\psi|^2\psi = 0, \quad (2.1.10)$$

with the following boundary condition

$$(-i\nabla + q\mathbf{A})\psi \cdot \mathbf{n}_{sc} = 0, \quad (2.1.11)$$

where \mathbf{n}_{sc} is the normal unit vector to the superconductor's surface. The boundary condition has a direct physical interpretation which is zero normal current flowing in or out of the system. These boundary conditions, which describe a superconductor vacuum interface, were initially derived, in the context of the BCS theory [21] by Cairoli, de Gennes and Matricon [35,36], with the assumption that the superconducting gap vanishes on the boundary at the same temperature at which it vanishes in the bulk. As shown in [37,38] this assumption is not correct, due to the existence of surface states with a higher critical temperature than for bulk states. The presence of these states opens numerous questions concerning the validity of previously used models, which we address in Papers 4-8.

Let us now vary the free energy functional 2.1.1 with respect to the vector potential, i.e., $\delta F/\delta\mathbf{A}$, obtaining

$$q \operatorname{Im}\{\psi^*\nabla\psi\} + q^2|\psi|^2\mathbf{A} + \nabla \times \nabla \times \mathbf{A} = 0. \quad (2.1.12)$$

Since $\nabla \times \mathbf{A} = \mathbf{B}$, we can use the Maxwell equation $\nabla \times \mathbf{B} = \mathbf{J}$ together with Eq. 2.1.12, to identify the supercurrent density as

$$\mathbf{J} = -q\left(\operatorname{Im}\{\psi^*\nabla\psi\} + q|\psi|^2\mathbf{A}\right). \quad (2.1.13)$$

In the case of a non-uniform superconducting field ψ , as described by Eq. 2.1.10, the global $U(1)$ symmetry becomes a local $U(1)$ symmetry, defined by the gauge transformations

$$\theta'(\mathbf{r}) = \theta(\mathbf{r}) + \phi(\mathbf{r}), \quad \mathbf{A}(\mathbf{r})' = \mathbf{A}(\mathbf{r}) - \frac{\nabla\phi(\mathbf{r})}{q}. \quad (2.1.14)$$

The magnetic penetration depth

As we said in the opening of this chapter, the phenomenological behaviour of a superconductor described with a Ginzburg Landau free energy depends on the value of a parameter conventionally called κ . In turn, this parameter is obtained as ratio of two fundamental characteristic lengths, the magnetic field penetration depth λ and the superconducting coherence length ξ . In this section we focus on deriving λ and understand its physical meaning. To derive the penetration depth, we solve the Ginzburg Landau equations in the London limit [17], which is enough to account for the electrodynamics effects between a superconductor and the magnetic field. Within the London limit, the order parameter modulus is uniform and equal to $|\psi_0|$ (solution of Eq. 2.1.3), while its phase is spatially dependent, i.e., $\psi = |\psi_0|e^{i\theta(\mathbf{r})}$. Let us begin by plugging this form for the order parameter in Eq. 2.1.12 and 2.1.13, obtaining

$$\nabla \times \nabla \times \mathbf{A} = \mathbf{J}, \quad \mathbf{J} = -\frac{1}{\lambda^2} \left(\frac{\nabla\theta}{q} + \mathbf{A} \right), \quad (2.1.15)$$

where we introduced the magnetic penetration depth λ

$$\lambda = \frac{1}{q|\psi_0|}. \quad (2.1.16)$$

To understand its physical meaning, let us take another curl of the equation for the vector potential and substitute $\nabla \times \mathbf{A} = \mathbf{B}$ obtaining,

$$\lambda^2 \nabla \times \nabla \times \mathbf{B} + \mathbf{B} = -\frac{1}{q} \nabla \times \nabla \theta. \quad (2.1.17)$$

If we assume our sample is simply connected, i.e., without vortices or other wound topological defects, then $\nabla \times \nabla \theta = 0$. Together with the identity $\nabla \times \nabla \times \mathbf{B} = -\nabla^2 \mathbf{B}$ we obtain

$$\lambda^2 \nabla^2 \mathbf{B} - \mathbf{B} = 0. \quad (2.1.18)$$

This equation describes the behaviour of the magnetic field in the inside of a superconductor. Let us consider, for simplicity, a superconductor which is infinite along

y and z , and starts along x for $x > 0$; $x < 0$ is the vacuum. Let us assume that $\mathbf{B} = B_0 \mathbf{e}_z$ for $x < 0$, then the solution for the equation above becomes

$$\mathbf{B}(x) = B_0 e^{-\frac{x}{\lambda}} \mathbf{e}_z. \quad (2.1.19)$$

Hence the magnetic field is exponentially suppressed when penetrating into the superconductor and λ is the characteristic length of the dampening process. Finally, we can study the temperature scaling of the penetration depth. Using the expansions for a and b used in Eq. 2.1.8 together with Eq. 2.1.3 we obtain

$$\lambda \sim \left(1 - \frac{T}{T_c}\right)^{-1/2}. \quad (2.1.20)$$

Hence for $T \rightarrow T_c$ the penetration depth diverges.

The coherence length

In the previous section we studied what happens when the modulus of the order parameter is uniform and the phase instead can change. Let us now study what happens when we have a perturbation in the modulus of the order parameter. Since we are interested in the behaviour the modulus of the order parameter, we assume ψ to be real, and neglect the magnetic field. Moreover let us assume $\psi = \psi_0 u(x)$, where $u(x) = 0$ for $x = 0$ and $u(x) = 1$ for $x \gg 1$, and ψ_0 is the solution of Eq. 2.1.3. We are now interested in studying the spatial profile of the order parameter. Hence, by inserting ψ in Eq. 2.1.10, we obtain:

$$-2\xi^2 \nabla^2 u - u + u^3 = 0, \quad (2.1.21)$$

where

$$\xi = \frac{1}{2\sqrt{|a|}} \quad (2.1.22)$$

is called the *coherence length*. In 1D this equation has solution

$$u = \tanh\left(\frac{x}{2\xi}\right), \quad (2.1.23)$$

which can be approximated, for $x \gg 1$, as

$$1 - u(x) \sim 2e^{-\frac{x}{\xi}}. \quad (2.1.24)$$

Hence, ξ is the characteristic length at which the modulus of the field recovers. Also in this case, we can study the scaling of ξ as a function of the temperature T . Let us insert in the definition of the coherence length the expansions for the a coefficient used in Eq. 2.1.8, yielding

$$\xi \sim \left(1 - \frac{T}{T_c}\right)^{-1/2}, \quad (2.1.25)$$

which diverges too as $T \rightarrow T_c$.

We are now ready to define the κ parameter, i.e.,

$$\kappa = \frac{\lambda}{\xi}. \quad (2.1.26)$$

Note that κ does not scale with the temperature T , as λ and ξ follow the same scaling law. Now that we introduced both the penetration depth and the coherence length, using equation Eq. 2.1.9, we can write the thermodynamic critical field as

$$H_c = \frac{\Phi_0}{4\pi\lambda\xi}, \quad (2.1.27)$$

where $\Phi_0 = 2\pi/q$ is the flux quantum, which we are about to introduce.

Flux quantization

To continue our overview of the basic characteristics of the Ginzburg Landau theory for a single band superconductor, let us study what happens when the considered domain is not simply connected, i.e., in the presence of topological defects. It is possible to carry out this analysis within the London limit, starting from Eq. 2.1.15. Let us consider a superconducting system with a random-shaped hole in the center

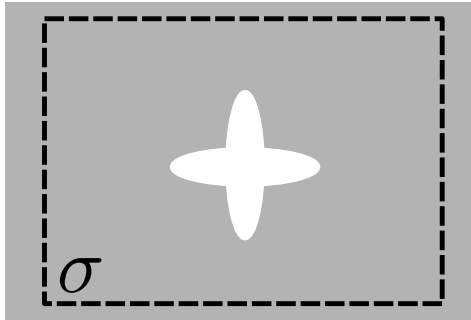


Figure 2.1: The gray area represents a superconducting sample with an exclusion in white, where we have the vacuum. The dashed black line represents the boundary that encloses the surface σ .

and calculate the magnetic flux through the surface σ displayed in Fig. 2.1. In this situation, the order parameter is defined everywhere except in the white exclusion. The magnetic flux reads:

$$\Phi = \int_{\sigma} \mathbf{B} \cdot d\mathbf{S} = \oint_{\partial\sigma} \mathbf{A} \cdot d\mathbf{l}. \quad (2.1.28)$$

We can then insert Eq. 2.1.15 obtaining

$$\Phi = \oint_{\partial\sigma} \mathbf{A} \cdot d\mathbf{l} = -\lambda^2 \oint_{\partial\sigma} \mathbf{J} \cdot d\mathbf{l} - \frac{1}{q} \oint_{\partial\sigma} \nabla\theta \cdot d\mathbf{l}. \quad (2.1.29)$$

Since we have some freedom in the choice of σ , we can assume it deep enough in the bulk so that the current \mathbf{J} is exponentially small². Hence the magnetic flux becomes

$$\Phi = -\frac{1}{q} \oint_{\partial\sigma} \nabla\theta \cdot d\mathbf{l}. \quad (2.1.30)$$

Since θ is the phase of the order parameter ψ , which is a complex field, its integral around a closed loop can only be 2π times a winding number N , yielding

$$\Phi = -\frac{2\pi}{q}N = -\Phi_0 N. \quad (2.1.31)$$

Where Φ_0 represents the *flux quantum*. We can therefore notice that the magnetic flux through a topological defect (i.e., a hole) embedded in our superconducting domain is quantized. The winding number N represents the topological charge trapped in the hole. This is one of the most important features of the magnetic behavior of superconductors, which is the ground for countless applications. This property becomes particularly relevant in type-II superconductors, where topological defects (vortices) are energetically favorable at certain magnetic fields. In fact, as we will shortly see, vortices are areas in the superconductor where the order parameter is locally suppressed and wound around, hence structurally equivalent to the hole we just studied. However, before diving into the physics of vortices, let us have a glance to the surface tension between a superconducting domain and a normal domain, as this is relevant to understanding why vortices nucleate in the first place.

Normal-Superconductor surface tension

Experimentally, it is possible to measure both a positive or negative surface tension between a superconducting phase and a normal phase, depending on the material studied. The Ginzburg Landau theory is able to account for both phenomena. Specifically, the materials having a positive surface tension, i.e., where normal-superconductor interface increases the free energy, are called *Type-I* superconductors. Conversely, those material where a normal-superconductor interface decreases the free energy are called *Type-II* superconductors. Within Ginzburg Landau theory, one can distinguish these two material using the parameter κ which we defined in Eq. 2.1.26. Type-I superconductors have $\kappa < 1$, while Type-II superconductors have $\kappa > 1$. Let us now see where this features comes from in the GL theory. We

²In the case of Eq. 2.1.19 we saw magnetic field decays exponentially while penetrating into the superconductor. Hence, using Maxwell's equation $\mathbf{J} = \nabla \times \mathbf{B}$ we have $\mathbf{J} = \frac{B_0}{\lambda} (0, e^{-\frac{z}{\lambda}}, 0)$, hence also the current density decays exponentially entering the bulk.

start by considering a domain wall between a superconductive phase and a normal phase. The domain wall is a solution of the 1D Ginzburg Landau equations (Eq. 2.1.10, 2.1.12) with the following boundary conditions

$$\psi \rightarrow 0 \quad H \rightarrow H_c \quad \text{for } x \rightarrow -\infty, \quad (2.1.32)$$

$$\psi \rightarrow \psi_0 \quad H \rightarrow 0 \quad \text{for } x \rightarrow +\infty. \quad (2.1.33)$$

In Fig. 2.2 we can see a schematic representation of the magnetic field and order

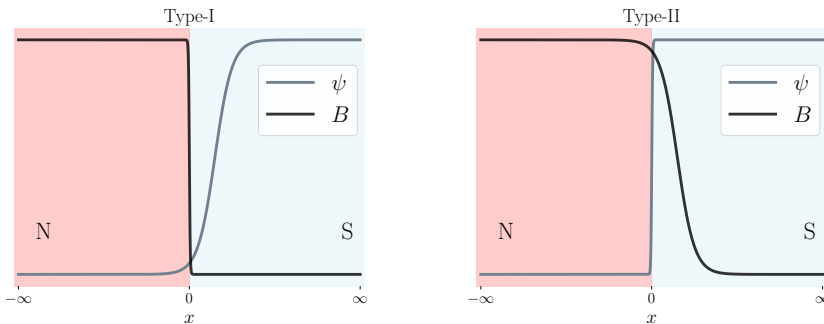


Figure 2.2: Order parameter ψ and magnetic field B profiles for the one dimensional domain wall solution of the Ginzburg Landau equations. The red area indicates the normal phase (N) while the light blue area indicates the superconducting phase (S).

parameter profiles in the case of a type-I and type-II superconductors. Following the derivation in [39], we calculate the free energy difference³ with respect to the normal state when the external magnetic field ($x \rightarrow \infty$) is equal to the thermodynamic critical field H_c . We therefore have

$$\begin{aligned} \sigma_{ns} = \Delta G &= G[\mathbf{A}, \psi] - \Omega \left(f_n + \frac{H_c^2}{2} \right) \\ &= \frac{H_c^2}{2} \int_{\Omega} d^3x \left[\left(1 - \frac{\nabla \times \mathbf{A}}{H_c} \right)^2 - \frac{|\psi|^4}{|\psi_0|^4} \right], \end{aligned} \quad (2.1.34)$$

where Ω defines the superconducting domain. For a strongly type-I material we have $\kappa \ll 1 \Rightarrow \lambda \ll \xi$, hence magnetic field is nearly immediately screened as the order parameter grows. Let us approximate then the magnetic field profile as an

³Since we consider a system with external magnetic field, the free energy to minimise is the Gibbs free energy, defined as $G = F - \mathbf{H} \cdot \mathbf{B}$, where F is the Helmholtz free energy.

Heaviside function $B \sim \Theta(x)$ and the order parameter as a smooth exponential $|\psi| \sim 1 - e^{-\frac{x}{\xi}}$. Then $\sigma_{ns}^{\kappa \ll 1}$ reads

$$\sigma_{ns}^{\kappa \ll 1} \simeq \frac{4}{3} \frac{H_c^2}{2} \xi, \quad (2.1.35)$$

which results in a positive-energy cost for the creation of normal-superconducting interfaces. Hence, the system will minimise the number of interfaces in its ground state. Let us now consider the opposite case, namely $\kappa \gg 1 \Rightarrow \lambda \gg \xi$, which describes a type-II superconductor. In this situation, we can assume that the order parameter behaves as an Heaviside function, i.e., $\psi \sim \Theta(x)$, while the magnetic field follows a smooth exponential profile $B(x) \sim e^{-\frac{x}{\lambda}}$. In this case, the interface energy reads:

$$\sigma_{ns}^{\kappa \gg 1} \simeq -\frac{3}{2} \frac{H_c^2}{2} \lambda. \quad (2.1.36)$$

Hence, we can notice that $\sigma_{ns}^{\kappa \gg 1}$ is negative, which implies that the formation of normal-superconducting interfaces is energetically beneficial. This negative surface tension is a key factor which allows vortices to nucleate. Let us then study the simplest model describing vortices in superconductors.

2.2 Type-II superconductors

Over the next few sections, we will focus on the properties of single band type-II superconductors. We begin by analyzing the structure of the vortices, i.e., topological solutions which are the characteristic signature of these materials. Then, we study the external magnetic conditions necessary for vortices to nucleate, concluding the section with a phase diagram for these superconductors.

2.2.1 Quantum vortices

A quantum vortex, within the Ginzburg Landau theory, is a *soliton*, i.e., a solution of the equations of motion which is localised in space, has a finite energy and has particle-like interaction with other solitons. The reason soliton-solutions are stable arises from the non-linearity of the model. Away from the center of the soliton, i.e., the center of the vortex, the order parameter recovers its bulk value, given by the uniform solution. Moreover, in the case of vortices, the soliton is also characterized by a topological charge, which corresponds to the winding of the vortex. There are multiple ways to create vortices in a superconductor, but the most typical one is to apply a sufficiently high external magnetic field. The vortices resulting from this nucleation process are also called quantum vortices, and the superconducting phase hosting many of them is called Shubnikov phase [34]. From a fluid-dynamics perspective, quantum vortices are irrotational structures, since the circulation of their superfluid velocity (directly proportional to the supercurrent \mathbf{J} defined in Eq. 2.1.13) is non zero only when the integration contour encloses the vortex itself.

When it does, the integral is quantized as we have seen in the previous section. Since the superconducting carriers are Cooper pairs, they are charged, which means that a circulating supercurrent does, in turn, generate a magnetic field, which decays in the superconductor with the magnetic penetration depth λ . Let us now study the main features of quantum vortices within the London limit [17]. In the London limit, a vortex is seen as a Heaviside-shaped cylinder of radius ξ , where superconductivity is suppressed and with a phase winding around it. Hence, it is particularly convenient to consider a 2D cylindrical superconducting system. Let us take Eq. 2.1.17, and assume we have a vortex with winding N in the origin. In this case the $\nabla \times \nabla\theta$ is not zero anymore, but is a generalised function which is zero everywhere except in the origin, where it is infinite, i.e., $\nabla \times \nabla\theta = 2\pi\delta(\mathbf{r})\mathbf{e}_z$. Hence Eq. 2.1.17 becomes

$$\lambda^2\nabla^2\mathbf{B} - \mathbf{B} = \Phi_0 N\delta(\mathbf{r})\mathbf{e}_z, \quad (2.2.1)$$

which has the solution

$$\mathbf{B}(\mathbf{r}) = \frac{\Phi}{2\pi\lambda^2} K_0\left(\frac{r}{\lambda}\right) \mathbf{e}_z. \quad (2.2.2)$$

Here, $\Phi = N\Phi_0$ and K_0 is the modified Bessel function of the second kind, which only depends on the radius r . We can now check the asymptotic limits of the magnetic field, namely

$$B_z(r) = \frac{\Phi}{2\pi\lambda^2} \sqrt{\frac{\pi\lambda}{2r}} e^{-r/\lambda} \quad r \rightarrow +\infty \quad (2.2.3)$$

$$B_z(r) = \frac{\Phi}{2\pi\lambda^2} \ln\left(\frac{\lambda}{r}\right) \quad r \rightarrow 0. \quad (2.2.4)$$

As expected the magnetic field decays exponentially for $r \gg \lambda$. We notice that B_z diverges when $r \ll \lambda$, which is a nonphysical divergence introduced by the London limit. In fact, we assumed the considered vortex to have a Heaviside-like profile of radius ξ , which sets a cutoff value for r . Hence, when the order parameter density goes to zero, the magnetic field value becomes

$$B_z(0) \approx B_z(\xi) = \frac{\Phi}{2\pi\lambda^2} \ln\left(\frac{\lambda}{\xi}\right), \quad (2.2.5)$$

where the approximation $B_z(0) \approx B_z(\xi)$ holds because we are in a strongly Type-II regime with $\lambda \gg \xi$. A schematic representation of a vortex in London limit is given by Fig. 2.3. Once the magnetic field is computed, it then possible to compute the superconducting current density as $\mathbf{J} = \nabla \times \mathbf{B}$, which results

$$\mathbf{J}(r) = \frac{\Phi}{2\pi\lambda^3} K_1\left(\frac{r}{\lambda}\right) \mathbf{e}_\phi. \quad (2.2.6)$$

We can now proceed to calculate the energy of this vortex structure (which is energy per unit of length considering the translational invariance in z). To do so,

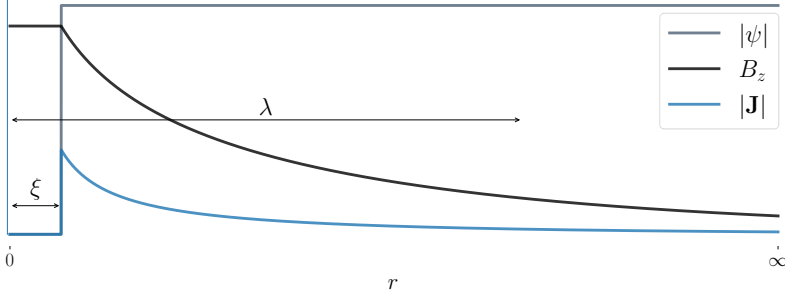


Figure 2.3: Radial plot parameter ψ , magnetic field B and current density modulus $|\mathbf{J}|$ for a superconductor described in the London limit with $\lambda \gg \xi$.

we spatially integrate the kinetic and magnetic terms of the free energy obtaining, together with Eq.2.2.1:

$$E_v = \frac{1}{2} \int d^2x (\lambda^2 \mathbf{J}^2 + \mathbf{B}^2) = \frac{\Phi}{2} B_z(0), \quad (2.2.7)$$

which is divergent due to Eq. 2.2.4, hence we introduce the cutoff at $r = \xi$ and add a correcting term for the vortex core as follows

$$E_v = \frac{\Phi}{2} B_z(\xi) + E_c. \quad (2.2.8)$$

To estimate E_c we can take the energy needed to nullify the superconducting field in the core, which is equal to the thermodynamic critical field times the area of the core $\frac{\pi \xi^2 H_c^2}{2} = \frac{1}{32\pi} \left(\frac{\Phi_0}{\lambda}\right)^2$ obtaining,

$$E_v = \frac{\Phi_0^2}{4\pi\lambda^2} \left(N^2 \ln \kappa + \frac{1}{8\pi} \right), \quad (2.2.9)$$

where we used $\Phi = N\Phi_0$ and $\kappa = \lambda/\xi$. We can see how, in the London limit, the magnetic field energy is dominant if compared to the core energy. In fact it depends on the square of the winding, and is proportional to $\ln \kappa$, with $\kappa \gg 1$, while the core energy remains a constant factor. This stops to hold, together with the London limit, when $\xi \sim \lambda$. Moreover in this limit E_v is positive, which suggests that the nucleation of a vortex will increase the energy of the system.

Lower critical magnetic field

To understand in which condition the vortex nucleation becomes energetically beneficial, let us study the difference in free energy when a vortex is added and external

magnetic field applied. Assuming the external magnetic field \mathbf{H} is parallel to the vortex line, the Gibbs free energy of a single-winded one-vortex system is

$$\Delta G = E_v - \int d^3x \mathbf{B} \cdot \mathbf{H} = E_v - \Phi_0 H, \quad (2.2.10)$$

where \mathbf{B} is the magnetic field generated by the vortex. To make the vortex nucleation energetically beneficial, we need $\Delta G < 0$ which results in the *lower critical magnetic field* $H_{c1} = E_v/\Phi_0$. Using 2.2.9 together with the definition of the thermodynamic critical field $H_c = \Phi_0/(4\pi\xi\lambda)$ we obtain

$$H_{c1} = \frac{H_c}{\kappa} \left(\ln \kappa + \frac{1}{8\pi} \right), \quad \kappa = \frac{\lambda}{\xi} \gg 1. \quad (2.2.11)$$

Hence, for applied magnetic fields $H > H_{c1}$ vortex nucleation decreases the energy of the system, and since in type-II superconductors the surface tension is negative, vortices begin to nucleate from the boundaries and populate the system. Here, we can see how type-I and type-II superconductors can differ in terms of high magnetic field behavior. As long as H remains below H_{c1} both materials exhibit a similar Meissner state, but as $H > H_{c1}$, a type-II material enters a new phase, called *Shubnikov phase*, which is characterised by the presence of quantized vortices in the bulk.

The Shubnikov phase

Let us assume the external magnetic field lies slightly above H_{c1} . Then vortices start nucleating and interact with the Meissner current running near the sample boundaries and with each other deep down in the bulk. It becomes therefore important to study which kind of interaction there is between pairs of vortices, and how it depends on their winding number. Since in type-II materials $\lambda > \xi$, it is reasonable to assume that the intervortex forces are mostly magnetic field mediated, hence we can study them within the comforts of the London limit. In the case of two vortices in positions \mathbf{r}_1 and \mathbf{r}_2 with winding $N_1 = N_2 = 1$ Eq. 2.2.1 becomes

$$\lambda^2 \nabla^2 \mathbf{B} - \mathbf{B} = \Phi_0 [\delta(\mathbf{r} - \mathbf{r}_1) + \delta(\mathbf{r} - \mathbf{r}_2)] \mathbf{e}_z, \quad (2.2.12)$$

which, thanks to the linearity of the London model results in

$$\mathbf{B}(\mathbf{r}) = \frac{1}{2\pi} \frac{\Phi_0}{\lambda^2} \left[K_0 \left(\frac{|\mathbf{r} - \mathbf{r}_1|}{\lambda} \right) + K_0 \left(\frac{|\mathbf{r} - \mathbf{r}_2|}{\lambda} \right) \right]. \quad (2.2.13)$$

As we did in the case of a single vortex, we can now calculate the energy of this configuration and study its contributing terms. The energy per unit of length is

$E^{1+1} = \frac{1}{2} \int d^2x [\lambda^2 (\nabla \times \mathbf{B})^2 + \mathbf{B}^2]$, and using the expression for \mathbf{B} that we just derived we have

$$E^{1+1} = 2E_v + \frac{1}{2\pi} \frac{\Phi_0^2}{\lambda^2} K_0 \left(\frac{|\mathbf{r}_1 - \mathbf{r}_2|}{\lambda} \right), \quad (2.2.14)$$

where E_v is the single vortex energy, for a single-winded vortex, derived in Eq. 2.2.9. The third term is the inter-vortex energy. Let us study the inter-vortex force, by defining $\mathbf{r}_{12} = |\mathbf{r}_1 - \mathbf{r}_2|$, we obtain

$$F_{12} = -\frac{\partial E^{1+1}}{\partial \mathbf{r}_{12}} = \frac{1}{2\pi} \frac{\Phi_0^2}{\lambda^2} K_1 \left(\frac{|\mathbf{r}_{12}|}{\lambda} \right) \frac{\mathbf{r}_{12}}{\|\mathbf{r}_{12}\|}. \quad (2.2.15)$$

Hence, if the vortices have opposite winding they attract each other and annihilate, while equally-winded vortices repel each other. This results describes uniquely the magnetic field mediated interaction. While in high κ regimes this approximation is very accurate, in low- κ materials an attractive core-core interaction may appear. To fully account for these effects it is necessary to solve the non-linear Ginzburg Landau model and further details are provided in [39]. Therefore, the vortices that nucleate from the boundaries repel each other, but at the same time they are contained in the bulk by the external magnetic field. To minimise the repulsion, the vortices form a spatially ordered lattice, and given a certain value of the external magnetic field, we expect a certain density of vortices in the sample. Numerical simulations show how the triangular vortex lattice represents the minimal energy solution.

The upper critical magnetic field H_{c2}

Let us suppose that we continue to increase the external magnetic field. At a certain point, when $H = H_{c2}$, the superconducting state will disappear entirely, and the material transitions to the normal state. This upper bound of the Shubnikov phase is called *upper critical magnetic field*, and was firstly derived by Abrikosov. Due to the presence of quantum vortices, we cannot neglect the magnetic orbital effects, which means that H_{c2} , is different from the thermodynamic critical field H_c . When the external magnetic field is high, the vortex density in the superconductor increases too. Near the critical point, the vortex cores overlap, resulting in a general suppression of the order parameter ψ and the magnetic field almost uniformly penetrating in the bulk. Given the small value of ψ , we can solve the linearized version of Eq. 2.1.10, i.e.,

$$(-i\nabla + q\mathbf{A})^2\psi = -2a\psi. \quad (2.2.16)$$

which is identical to Schrödinger's equation for a charged particle in an external field. The lowest eigenvalue solving this problem is $-a = qH/2$. For at least one solution to exist, we require $-a \geq qH/2$ therefore the upper critical field is

$$H_{c2} = -\frac{2a}{q} = \frac{\Phi_0}{4\pi} \frac{1}{\xi^2} = \kappa H_c, \quad (2.2.17)$$

Since this holds in type-II superconductors, where $\kappa > 1$ we have that $H_{c2} > H_c$.

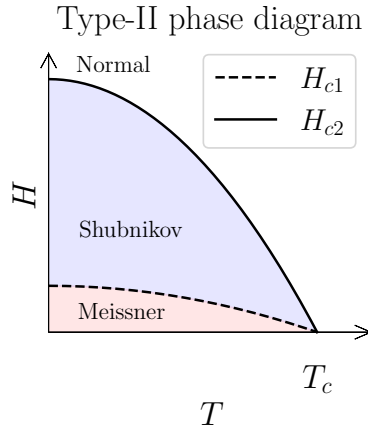


Figure 2.4: Phase diagram for a type-II superconductor as a function of temperature T and external magnetic field H . The Meissner phase is red-colored, while the Shubnikov phase is in blue.

Type-II superconductor phase diagram

In Fig. 2.4 we sketch a qualitative phase diagram for a type-II superconductor. For external magnetic fields smaller than $H_{c1}(T)$, the superconductor lies in a Meissner state, but as H surpasses the lower critical field, there is a transition to the Shubnikov phase, and vortices begin to populate the superconductor. As the field keeps growing, the material transitions to the normal phase and superconductivity is lost. Fig. 2.5, schematically depicts the magnetization curve of a type-II superconductor. For magnetic fields below the lower critical field H_{c1} , the superconductor is in the Meissner phase, having therefore a perfectly diamagnetic response. As $H_{c1} < H < H_{c2}$ we enter in the Shubnikov phase, where vortices nucleate and form the Abrikosov lattice, yielding a gradual decrease of the magnetization.

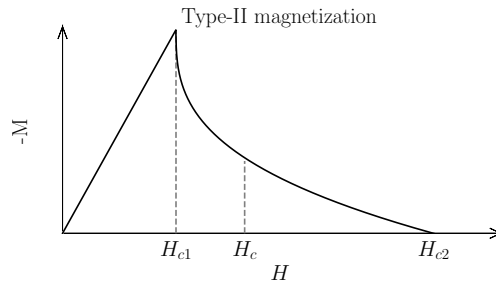


Figure 2.5: Schematic magnetization response for a type-II superconductor.

2.3 Nucleation barriers in single band type-II superconductors

Now that we have seen the phase diagram for a single band type-II superconductor, as well as the physics of quantum vortices, let us introduce the concept of vortex nucleation barrier. Let us suppose that the considered superconducting system can host only one vortex in the Shubnikov phase. Then, for external magnetic field $H < H_{c1}$ the global minimum of the system is a Meissner state, while for $H > H_{c1}$ the global minimum becomes a single winded vortex. However, it turns out that at $H = H_{c1}$ the Meissner state does not become unstable, but transitions from being the global minimum to being a metastable state. In fact, the Ginzburg Landau theory can sustain different local minima, which means that there can be different metastable states in addition to the global minimum. Hence, if not perturbed, the system can remain in the Meissner state for fields higher than H_{c1} , process known as *magnetic superheating* [40]. One can interpret the superheating process towards nucleation as if there was an energy barrier to overcome to start nucleating vortices in the system [40, 41]. The presence of perturbations is normally the triggering event. We can therefore define a *nucleation magnetic field* H_n , above which, the barrier is nullified and vortices are free to enter. Similarly, when we do a field-cooled experiment, and transition from a Shubnikov state to a Meissner state, the presence of vortices in the bulk becomes metastable and the Meissner state becomes the global minimum. In this case, we talk of *magnetic supercooling*, and it can be seen as there being an energy barrier to the complete expulsion of the vortices from the bulk. In this case, we can define an expulsion magnetic field H_e , below which vortex states become unstable. Including the expulsion and nucleation fields, the phase diagram in Fig. 2.4 qualitatively becomes Fig. 2.6. Below the expulsion field H_e , the only state possible is the Meissner one, which is also the global minimum of the phase. For $H_e < H < H_{c1}$, the Meissner state is the global minimum, however quantum vortices are allowed in a metastable configuration. In fact, if one does a field-cooling experiments, starting from a Shubnikov state, the vortices are likely to remain in the system until the external magnetic field reaches H_e ⁴. Above the lower critical field, i.e., for $H_{c1} < H < H_n$, the situation is flipped: the Meissner state is metastable while the Shubnikov state becomes the global minimum. In a field-heating experiment, the Meissner state persists up to the nucleation field. For $H \geq H_n$, vortices begin to nucleate and the only possible states present quantum vortices. Several analytical and numerical methods have been proposed to compute the nucleation magnetic field [42–52], however the problem of computing the vortex entry energy barrier was uniquely addressed by Bean and Livingston in 1964 [41]. They analyze a semi infinite two dimensional⁵ strongly type-II single band superconductor, where the London-limit [17] calculations carried out before, represent a good approximation. They first study the interaction between

⁴In this case, we are neglecting any type of fluctuation

⁵or equivalently three dimensional with z -translational invariance

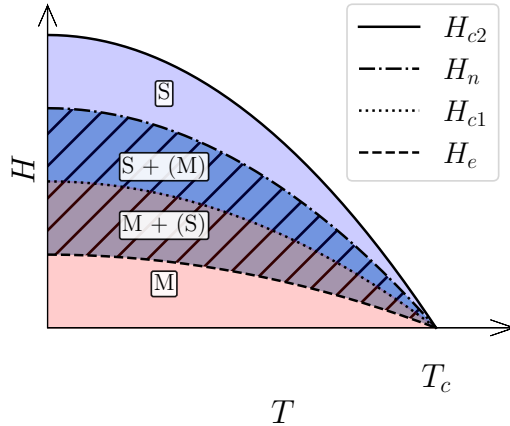


Figure 2.6: Schematic representation of the $H - T$ phase diagram for a type-II superconductor. "M" stands for Meissner phase, while "S" indicates the Shubnikov phase. The dashed areas allow metastable states (written in parenthesis) in addition to the global minimum one.

a single-winded vortex in the bulk at a distance d from the boundary and the boundary itself, in the absence of the Meissner current. To respect the boundary conditions of zero normal current, they utilize the image method, where an image anti-vortex effectively replaces the role of the boundary, allowing a convenient way to write the interaction energy. Then, using the linearity of the London limit, the Meissner current, arising due to the external magnetic field, is superimposed. The Gibbs free energy for this configuration reads

$$G \simeq -\frac{1}{2} \frac{1}{2\pi} \frac{\Phi_0^2}{\lambda^2} K_0 \left(\frac{2d}{\lambda} \right) + \Phi_0 H e^{-\frac{d}{\lambda}} + H_{c1} \Phi_0 - H \Phi_0. \quad (2.3.1)$$

The first term is the interaction energy between the vortex at distance d from the boundary and the image antivortex, the second term is the interaction between the vortex and the Meissner current, the third term is the energy contribution of the magnetic field of the vortex, and the last term is the energy of the magnetic field. By rescaling $d' = \lambda d$, $H' = H_c H$ and $G' = H_c^2 \lambda^2 G$, we can rewrite the system's energy as

$$G \simeq \frac{4\pi}{\kappa} \left[H(e^{-d} - 1) - \frac{1}{\kappa} K_0(2d) + \frac{1}{\kappa} \left(\ln(\kappa) + \frac{1}{8\pi} \right) \right]. \quad (2.3.2)$$

The force acting on the vortex is given by $F = -\partial G / \partial d$

$$F_{BL} \simeq \frac{4\pi}{\kappa} \left[H e^{-d} - \frac{2}{\kappa} K_1(2d) \right]. \quad (2.3.3)$$

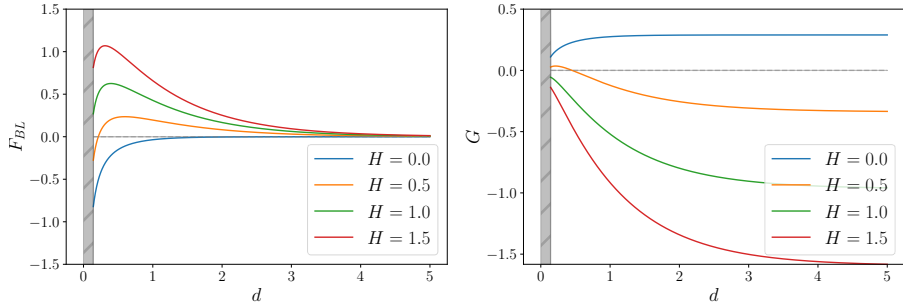


Figure 2.7: Net force acting on a vortex at a distance d from the boundary, and Gibbs free energy associated to the position of the vortex. The different curves show the same quantities for different values of the external magnetic field H . The gray area represents the cutoff region of this model.

However, it is important to consider that Eq. 2.3.2 is divergent for $d \rightarrow 0$, due to the fact that the London model has a cutoff at the vortex core. This represents an extremely limiting factor, since, in the nucleation process, the vortex core undergoes deformations. Moreover, to determine the nucleation field in the Bean Livingston model, it is necessary to assume a cutoff, which in [41] is chosen at $d = \sqrt{2}\xi$. Then, it is possible to study the sign of the force acting on the vortex, to determine whether it is repelled or attracted into the bulk. By doing so, Bean and Livingston find $H_n \simeq H_c/\sqrt{2}$ as nucleation field. It is of fundamental importance to underline that this value strongly depends on the choice of the cutoff distance from the boundary, which is essentially arbitrary, and is limited to $\kappa \gg 1$ regimes. Fig. 2.7 shows an example of the force acting on the vortex and the Gibbs energy of the system, for various values of the external magnetic field. The gray area represents the cutoff region of this model. The presence of metastable states introduces an hysteresis in the magnetization curve of Fig. 2.5, which qualitatively becomes as in Fig. 2.8.

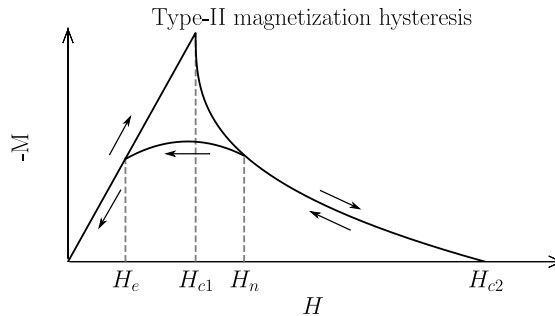


Figure 2.8: Schematic magnetization curve of a type-II superconductor taking into account the metastability of the Meissner and Shubnikov phases.

To correctly model the nucleation of a vortex in a superconductor, the Ginzburg Landau theory in Eq. 2.1.1 needs to be employed. However, due to the non-linear nature of the model, it is not amenable to analytical treatments. Moreover, the effects of impurities and surface roughness cannot be accounted for in a controllable way within the London model, due to the alterations of the vortex core structure during the nucleation process. In the context of the Ginzburg Landau theory, finding the energy barrier and determining its maximum is equivalent to finding the saddle point between two metastable states, also called *sphaleron* [53–57], i.e., the maximum of the minimum free energy path between the two minima. Being able to numerically determine the vortex nucleation energy barrier, without uncontrollable approximations, is crucial for superconductor applications. A deeper understanding of the nucleation processes, in the presence of impurities and/or surface roughness would strongly improve the modelling abilities of superconducting devices, such as superconducting current transmission lines or superconducting RF cavities [49]. Moreover, the problem of vortex nucleation is now relevant in quantum technologies, where devices like superconducting single photon detector claim to create a current carrying state with a low vortex nucleation barrier: as a single photon perturbs the system, a vortex is created and its presence detected [58, 59]. Finally, having at disposal a method to study the dependence of the nucleation barriers on the sample geometry, would be a crucial advantage in designing more efficient topological qubits [60–64]. This represents a strong motivation for further research activity, aimed at building a systematic method to compute the vortex nucleation and expulsion barriers, as well as H_n and H_e , taking into account the full non-linearity of the Ginzburg Landau theory, arbitrary geometries and the presence of surface roughness and impurities. During my PhD, this research topic has been addressed, and resulted in two papers being realised together with Andrea Maiani [65], a dear friend, and at the time master student in our group, and Filipp N. Rybakov. The papers we realised are Paper 2 and Paper 3. They focus on the numerical computation of the nucleation barrier for various nucleation processes and Ginzburg Landau parameters. To achieve the accuracy required for this calculation we developed a numerical framework which applies the *string method* to gauge theories. Chapter 3 will provide the reader the necessary background information to fully appreciate our work.

2.4 Type-I superconductors

We conclude this introduction on superconductivity with type-I superconductors. All the superconducting elements in the periodic table, except Niobium, are type-I superconductor [40]. As we saw in Eq. 2.1.35, the normal-superconducting surface tension is positive in type-I superconductors, hence quantum vortices are not energetically stable. Hence, only the Meissner state is energetically favourable, and the magnetic field is entirely screened from the bulk by the superconducting current. In a type-I superconductors, there is only one critical magnetic field, and it is equal to the thermodynamic critical field H_c . The phase diagram is displayed in the left panel of Fig. 2.9 Since the magnetic field is entirely screened from the bulk,

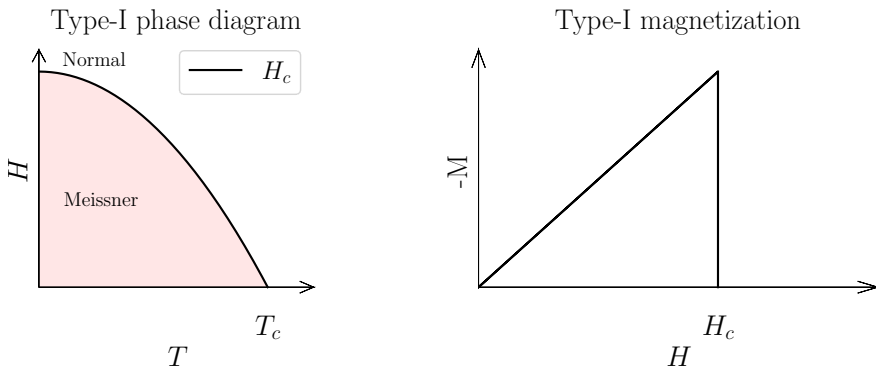


Figure 2.9: The left image displays the phase diagram for a type-I superconductor as a function of temperature T and external magnetic field H , where Meissner phase is red-colored. The right panel shows the magnetization response for the same type-I superconductor as a function of the external magnetic field H

type-I superconductors exhibit perfect diamagnetism, where the magnetization of the sample perfectly cancels the externally applied field. The right panel of Fig. 2.9 shows the magnetization curve as a function of the external magnetic field H ; we can notice its perfectly linear behavior, and a first order phase transition to normal state at $H = H_c$. As we have seen in type-II superconductor, also in type-I it is possible to obtain superheated and supercooled states. In this situation however, the possible states are fewer, as the only two allowed phases are the Meissner phase and the normal one. Hence, it is possible to maintain a Meissner state for fields higher than H_c , up to a superheating field H_{sh} , in a metastable way, by slowly increasing the external magnetic field. Similarly, it is possible to maintain the superconductor in its normal state for magnetic fields lower than H_c , down to the supercooling field H_{sc} , if the external magnetic field is adiabatically decreased in a field-cooling experiment. However, in this thesis, we do not study type-I superconductors, hence we will not go into further details.

2.5 Multiband GL theory

It did not take much time, after the publication of the BCS theory [21] in 1957, to understand that it was indeed possible for a material to have more than one superconducting gap. Two years later, the first multiband superconductor was theorised [23, 24]. The model relied on the presence of distinct Fermi surfaces yielding multiple gaps, with different characteristics and critical temperatures. It took forty years to experimentally confirm the existence of multiband superconductors. The first multiband properties were claimed in MgB₂ [25–28]. In 2004 multiband superconductivity was discovered in Iron-based compounds, which now are among the most common and numerous multiband superconductors [1, 2, 29–33]. In a multiband superconductor, different bands have electron pairing giving raise to multicomponent order parameter. In the following sections we dive into the main properties of multiband superconductors, underlining their fundamental properties and what is still unknown.

From a theoretical perspective, as for single band superconductors, there are different models which can be used to describe these materials. Here, we extend the Ginzburg Landau theory to multiband materials [39], which provides a *macroscopic* description. In Chapter 4 we show how to describe and treat multiband superconductors microscopically.

Within the Ginzburg Landau framework, one can describe multiple superconducting gaps using multiple order parameters, each having an Eq. 2.1.1-like free energy functional [39]. It is indeed possible to prove this microscopically, as shown in [66–69]. In this thesis we only consider two band superconductors within the Ginzburg Landau model, therefore, let us write the free energy density for a 2-band superconductor:

$$f[\psi, \mathbf{A}] - f_N = \sum_{\alpha=1}^2 \left[\frac{1}{2} |(\nabla + iq\mathbf{A})\psi_{\alpha}|^2 + a_{\alpha}(T)|\psi_{\alpha}|^2 + \frac{b_{\alpha}(T)}{2} |\psi_{\alpha}|^4 \right] + V_{\text{int}} + \frac{(\nabla \times \mathbf{A})^2}{2}. \quad (2.5.1)$$

Here, the letter α indicates the superconducting band. By comparing this expression to the single-band case, we can notice that we have the simultaneous presence of multiple order parameters. In contrast to typical unconventional superconductors [70] here multiple components of the order parameter can arise without multiple broken symmetries. This clearly complicates the description of the superconductor. In general, for multiband superconductors it is not possible to define independent κ parameters for each band, and this is due to the presence of V_{int} . V_{int} arises in multiband models and represents the interband interaction, which takes the form of a Josephson coupling (originating from the Josephson tunnelling effect [71, 72]). The two types of Josephson interaction which we consider are

$$V_{\text{int}} = \eta(\psi_1\psi_2^* + \psi_1^*\psi_2) \quad \text{Bilinear} \quad (2.5.2)$$

$$V_{\text{int}} = \eta(\psi_1^2\psi_2^{*2} + \psi_1^{*2}\psi_2^2) \quad \text{Biquadratic} . \quad (2.5.3)$$

The presence of Josephson terms yields new phenomena, such as the presence of passive bands⁶ or phase frustration situations. The multicomponent Ginzburg Landau model has also been used to describe other physical systems, such as neutron stars [73], metallic hydrogen [74], or superconductors with unconventional pairing symmetries [70].

Ground states

As long as $V_{\text{int}} = 0$, it is possible to analytically find the ground states solution of the system. Similarly to Eq. 2.1.3, the ground states are uniform and read:

$$|\psi_\alpha^0| = u_\alpha = \sqrt{\frac{-a_\alpha}{b}}. \quad (2.5.4)$$

Moreover, with no interband coupling, each matter field can be associated to a specific coherence length, namely

$$\xi_\alpha = \frac{1}{2\sqrt{-a_\alpha}}. \quad (2.5.5)$$

However, as soon as $V_{\text{int}} \neq 0$ this is no longer possible due to the so called *coherence length hybridization*, which mixes the coherence lengths of the various bands.

2.5.1 Fractional quantum vortices

Due to the presence of multiple order parameters, there are several possible topological solutions. A singularity with a 2π winding in one component and none in the other is called *fractional vortex*.

Let us start by assuming $V_{\text{int}} = 0$; this implies there is no direct coupling between the order parameters. However, each order parameter is coupled to the vector potential \mathbf{A} , hence they interact with each other through it. Since this interaction is magnetic, it is possible to study it within the London limit [17, 39], where the order parameters' modulus are uniform and equal to the ground state values $u_{1,2}$, the vortex core is Heviside-shaped and the magnetic penetration depth λ , much bigger than each coherence length ξ_α . By taking the functional derivative of Eq. 2.5.1 with respect to the vector potential, we obtain

$$\nabla \times \nabla \times \mathbf{A} + q \sum_{\alpha=1}^2 u_\alpha (\nabla \theta_\alpha + q\mathbf{A}) = 0, \quad (2.5.6)$$

where we wrote the order parameters as $\psi_\alpha = u_\alpha e^{i\theta_\alpha}$. We can then identify the superconducting current density as

$$\mathbf{J} = \sum_{\alpha=1}^2 \mathbf{j}_\alpha = -q \sum_{\alpha=1}^2 u_\alpha^2 (\nabla \theta_\alpha + q\mathbf{A}), \quad (2.5.7)$$

⁶One talks of passive bands when $a_\alpha > 0$ but the order parameter is non-zero, thanks to the Josephson interaction

where in this context, the magnetic penetration length is defined as

$$\lambda = \frac{1}{\sqrt{q^2(u_1^2 + u_2^2)}} = \frac{1}{\sqrt{q^2\rho^2}}, \quad (2.5.8)$$

with $\rho^2 = u_1^2 + u_2^2$. By taking the curl of Eq. 2.5.6, together with $\nabla \times \mathbf{A} = \mathbf{B}$, we obtain the closed equation for the magnetic field

$$\lambda^2 \nabla^2 \mathbf{B} - \mathbf{B} = \lambda^2 q \sum_{\alpha=1}^2 u_{\alpha}^2 \nabla \times \nabla \theta_{\alpha}. \quad (2.5.9)$$

To have a fractional vortex in the system, let us assume $\nabla \times \nabla \theta_1 = 2\pi\delta(\mathbf{r})$ and $\nabla \times \nabla \theta_2 = 0$. Then Eq. 2.5.9 becomes

$$\lambda^2 \nabla^2 \mathbf{B} - \mathbf{B} = \underbrace{\Phi_0 \frac{u_1^2}{\rho^2}}_{\Phi} \delta(\mathbf{r}) \quad \Rightarrow \quad \mathbf{B}(\mathbf{r}) = \frac{\Phi}{2\pi\lambda^2} K_0\left(\frac{r}{\lambda}\right) \mathbf{e}_z. \quad (2.5.10)$$

By computing the flux of the magnetic field through the domain, we obtain $\Phi = \Phi_0 u_1^2 / \rho^2$ which is a fraction of the flux quantum since $\rho^2 = u_1^2 + u_2^2$. Hence the name fractional vortices. The energy of this vortex configuration is given by [39] and reads

$$E_{FV} = \frac{1}{4\pi} \frac{u_1^4 \Phi_0^2}{\rho^4 \lambda^2} \ln \frac{\lambda}{\xi_1} + \frac{\pi}{2} u_1 u_2 \ln \frac{R}{\xi_1}, \quad (2.5.11)$$

where R indicates the macroscopic linear size of the system. We can see how the energy of fractional vortices scales with the logarithm of the system size, which represents a strong energy penalization [75]. Stable fractional vortices have been theoretically demonstrated in two band superconductors both within the London limit [76] and in the full Ginzburg Landau model [77]. However, a crucial aspect, to deepen the understanding of these topological excitations, is the structure of the nucleation barrier for fractional vortices, which we address in Paper 3. Another relevant factor, which influences the formation of fractional vortices, is their interaction with the boundaries of the system. In fact, for temperatures above the bulk critical temperature, superconductors exhibit surface states, as demonstrated in [12, 37, 38] for the single band case. In Paper 4, we investigate the presence of surface states in two band superconductors, described using a microscopic theory, laying the grounds for further investigations of fractional vortices.

2.5.2 Composite quantum vortices

Still under the assumption of $V_{\text{int}} = 0$, let us suppose we have fractional vortices, in the same position, in both superconducting bands, i.e., $\nabla \times \nabla \theta_1 = \nabla \times \nabla \theta_2 = 2\pi\delta(\mathbf{r})$. In this scenario, the fractional vortices interact with each other through

their coupling to the vector potential \mathbf{A} , forming a so-called *composite vortex* [39]. In this case Eq. 2.5.9 becomes

$$\lambda^2 \nabla^2 \mathbf{B} - \mathbf{B} = \Phi_0 \delta(\mathbf{r}) \quad \Rightarrow \quad \mathbf{B}(\mathbf{r}) = \frac{\Phi_0}{2\pi\lambda^2} K_0\left(\frac{r}{\lambda}\right) \mathbf{e}_z. \quad (2.5.12)$$

Here the magnetic field flux is equal to the flux quantum, yielding back the of the magnetic flux. The energy of the composite vortex reads

$$E_{CV} = \frac{1}{4\pi} \frac{\Phi_0^2}{\lambda^2} \ln \frac{\lambda}{\xi}. \quad (2.5.13)$$

By comparing Eq. 2.5.11 and Eq. 2.5.13, it is possible to see how, for a large system, the composite vortex has the minimal energy compared.

2.5.3 Type 1.5 superconductivity

In the previous section we saw that, in a multicomponent superconductor, the composite vortex is the thermodynamically stable topological excitation. In the absence of interband coupling, the system is characterized by the three length scales

$$\lambda = \frac{1}{|q|\sqrt{u_1^2 + u_2^2}} \quad \xi_1 = \frac{1}{2\sqrt{-a_1}} \quad \xi_2 = \frac{1}{2\sqrt{-a_2}}. \quad (2.5.14)$$

Differently from the single component case, we now have one more length scale, which has strong physical implications. The spontaneous question arising is: how do multiband superconductors fit the type-I and type-II classification scheme with an extra length scale?

In a type-I superconductor the coherence length is larger than the magnetic penetration depth, hence we can classify a two-band superconductor as type-I when $\xi_{1,2} > \lambda$. In this situation, external magnetic fields are completely screened, while strong fields give rise to the formation of macroscopic normal domains. Similarly, a two-band superconductor classifies as type-II when we have $\xi_{1,2} < \lambda$. In this regime the interactions are mainly magnetic-field mediated, and the vortices repel each other once they begin nucleating, as we saw in the single band case. For magnetic fields lower than H_{c1} the global minimum is a Meissner state, while for $H_{c1} < H < H_{c2}$ the global minimum is a Shubnikov state.

In contrast to the single component case, in a two band superconductor, we can have the situation $\xi_1 < \lambda < \xi_2$. This regime is named *type-1.5*, due to the fact that one band is type-I-like while the other is type-II-like [39, 78, 79]. The experimental works in [80–83] claim to find type-1.5 superconductivity in the materials MgB_2 , Sr_2RuO_4 and ZrB_{12} . In a type-1.5 superconductor, a (concentric) composite vortex sees the core of the second component being much larger than the core of the first component. Hence, the first component has a mostly density-mediated attractive interaction with other vortices, while the second component exhibits a mainly

magnetic-mediated repulsive interaction. However, these opposite interactions occur at different length scales, resulting in a regime with short-range repulsive, long-range attractive interactions. Following the calculations in [39], we can show that the interaction energy between two widely separated composite vortices is

$$E_{int} = 2\pi \left[C_B^2 K_0 \left(\frac{r}{\lambda} \right) - C_1^2 K_0 \left(\frac{r}{\xi_1} \right) - C_2^2 K_0 \left(\frac{r}{\xi_2} \right) \right]. \quad (2.5.15)$$

The first term is the magnetic repulsion, while the second and third come from the core-core attractive interactions. The coefficients C_B, C_1, C_2 depend on the GL free energy parameters. The long range attractive, short range repulsive nature of the interaction can yield the formation of stable vortex clusters, which are not possible in type-I and type-II regimes. The multiband Ginzburg Landau theory represents an effective theoretical framework to numerically investigate the properties of type-1.5 superconductors as shown in [84–86]. Moreover, it is possible to derive GL models for multiband type-1.5 superconductors from microscopic theories [87].

2.5.4 Josephson interaction

The Josephson interaction couples the order parameters of the different bands, it can involve only their moduluses or both moduluses and phases. In either case, the superconducting condensates are not independently conserved. The simplest Josephson interaction for a two band superconductor introduces a bilinear coupling between the two components, which reads

$$V_{int} = \eta(\psi_1 \psi_2^* + \psi_1^* \psi_2) = 2\eta |\psi_1| |\psi_2| \cos(\theta_1 - \theta_2). \quad (2.5.16)$$

We can see how this penitential term couples not only the densities of the order parameters but also the difference between their phases. Depending on the sign of η a phase difference of $\theta_1 - \theta_2 = \pi$ can be energetically preferable over $\theta_1 - \theta_2 = 0$. Moreover, the presence of this terms prevents us to associate coherence lengths to individual bands, but yields the coherence length hybridization [39, 85]. To fully appreciate the effects of the Josephson coupling on vortex interactions, it is necessary to turn to numerical simulations. When, in a two band superconductor, the Josephson interaction is biquadratic, i.e.,

$$V_{int} = \eta(\psi_1^2 \psi_2^{*2} + \psi_1^{*2} \psi_2^2), \quad (2.5.17)$$

a new class of states emerges, namely those breaking the time reversal symmetry [39]. Given their strong physical implications, we will dedicate the two next sections to present them.

2.5.5 Time reversal symmetry breaking states

As we have seen in the first chapter, for a single component superconductor, the ground state spontaneously breaks the continuous $U(1)$ symmetry of the model. In

the two band case, without V_{int} , the system has a $U(1) \times U(1)$ symmetry, since the phases of the two order parameters are independently coupled to the gauge field. When we introduce the bilinear Josephson coupling, however, we add a $\cos(\theta_1 - \theta_2)$ coupling between the two phases which reduces the model symmetry to $U(1)$.

Let us now study what happens when we introduce the biquadratic Josephson coupling

$$V_{\text{int}} = \eta(\psi_1^2 \psi_2^{*2} + \psi_1^{*2} \psi_2^2) = 2\eta |\psi_1|^2 |\psi_2|^2 \cos[2(\theta_1 - \theta_2)]. \quad (2.5.18)$$

If $\eta > 0$, to minimize the energy the $\cos[2(\theta_1 - \theta_2)] = -1$, which is obtained for $\theta_1 - \theta_2 = \pm\pi/2$. This means that there are two ground states possible, which are equivalent in energy. The two states are related by a complex conjugation operation, which introduces a Z_2 symmetry in the model. The two states are schematically represented in Fig. 2.10. In this case, the system's symmetry



Figure 2.10: Energetically equivalent ground states breaking time reversal symmetry.

is $U(1) \times Z_2$, which is broken by the ground state, hence the name time reversal symmetry breaking. Also the bilinear Josephson coupling can lead to time reversal symmetry breaking, however three bands are necessary. Superconducting states which break time reversal symmetry have been an extremely active field of research over the last decades, due to the strong physical implications that this phenomenon entails. Numerous theoretical works analyzed some of the expected phenomena in two and three band superconductors breaking time reversal symmetry, such as domain walls and skyrmions formation [4, 5, 84, 88–93]. On the experimental side, the results presented in [1, 2, 94] claim to find Fe-based superconductors in time reversal symmetry breaking states. However, even if a number of candidate materials have been identified, the nature of their order parameters still remains unknown and a topic of active research. In the next section, we present the most remarkable signature of time reversal symmetry breaking, namely the *domain wall* and explain its experimental signatures.

2.5.6 Domain walls

In a two band superconductor with biquadratic Josephson coupling, it is possible to have a new type of topological excitation, namely a *domain wall* [39]. One has a domain wall when the system is in different ground states in different areas. Fig. 2.11

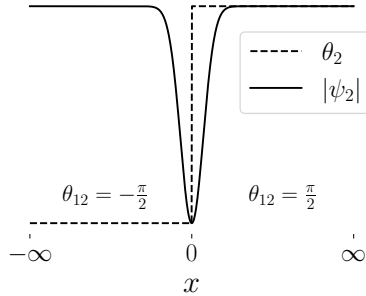


Figure 2.11: Schematic representation of a domain wall in a two band superconductor with biquadratic Josephson coupling. In this case, the phase of the first band is set to zero and spatially uniform, while the phase of the second component changes from $-\pi/2$ to $\pi/2$ at $x = 0$. To avoid divergences in the free energy, $|\psi_2| = 0$ at $x = 0$.

shows a schematic representation of such structure. As we can see, the phase difference between the two components is $\pi/2$ for $x > 0$ and $-\pi/2$ for $x < 0$. To allow for the change of the phase difference from $-\pi/2$ to $\pi/2$, the order parameter whose phase changes value needs to locally nullify its density to avoid energy divergences. The presence of domain walls is generally hard to detect. However, their formation can be facilitated by the presence of pinning sites, in correspondence of which, spontaneous magnetic fields are generated [6, 88]. Spontaneous magnetic field arising from domain walls are one of the most promising explanations to account for the spontaneous magnetic fields that are experimentally measured, through muon-spin rotation [1, 2] in Fe-based superconductors such as $\text{Ba}_{1-x}\text{K}_x\text{Fe}_2\text{As}_2$. Also the presence of impurities can yield spontaneous magnetic fields [93]. Hence, it becomes crucial to carefully study the properties of the domain-wall-generated fields, to understand their origin.

States naming convention

Depending on the GL model parameters there can be different ground states, where the phase difference between components gives important information concerning the system broken symmetries. Hence, a standard naming convention was introduced. Assuming to have an s -wave superconductor

$$s_{++} \quad \text{state} \quad \rightarrow \quad \theta_1 - \theta_2 = 0, \quad (2.5.19)$$

$$s_{+-} \quad \text{state} \quad \rightarrow \quad \theta_1 - \theta_2 = \pi, \quad (2.5.20)$$

$$s \pm is \quad \text{state} \quad \rightarrow \quad \theta_1 - \theta_2 = \pm \frac{\pi}{2}. \quad (2.5.21)$$

It is indeed possible that the two superconducting fields have different symmetries, e.g., the first band could have s -wave symmetry while the second d -wave symmetry⁷. In this case, one indicates a time reversal symmetry breaking state as $s \pm id$. In the case of a three band superconductor, any non-trivial phase difference between the bands, breaks time reversal symmetry and therefore constitutes an $s + is$ state. Moreover, when the phase difference between the bands is non-zero the superconductor is said to be *frustrated*.

The leading candidates for time reversal symmetry breaking in Fe-based superconductor are, in fact, $s + is$ and $s + id$ states [78, 84, 89–91, 94]. If the domain wall formation can be associated to the presence of spontaneous magnetic fields, then it could be a candidate explanation for the magnetic signatures measured in [1, 2]. To this end, the questions that need to be answered are:

1. How can one distinguish $s + is$ from $s + id$ states?
2. How do crystalline anisotropies influence the formation of spontaneous magnetic fields?

Several theories to answer the first question were proposed in the case of impurity-generated magnetic fields [95–99], however, a systematic study for the case of domain walls was not proposed. We present such analysis in Paper 1 for the case of an anisotropic superconductor, described by a microscopically derived Ginzburg Landau model.

In the next section, we present how to introduce anisotropies in a GL theory and show how the spontaneous magnetic field can arise.

⁷A d -wave superconductor can be treated by a GL theory with terms respecting the d -wave pairing symmetry.

2.6 Spatially anisotropic GL theory

To complete this introduction on the Ginzburg Landau theory, it is important to mention how the Ginzburg Landau free energy functional, i.e., Eq. 2.5.1, changes when the system is spatially anisotropic (e.g., lattice anisotropies). Simply speaking, having spatial anisotropies means that different spatial directions are not equivalent. Therefore, in the context of a field theory, it implies that the gradients of the fields have different energy costs in different directions. Hence, the version of Eq. 2.5.1 in an anisotropic s -wave two bands superconductor reads:

$$F = \int d^3x \left[\frac{1}{2} \sum_{\alpha ij} (D_i \psi_\alpha)^* Q_{ij}^\alpha (D_j \psi_\alpha) + \mathcal{V}_p + \frac{(\nabla \times \mathbf{A})^2}{2} \right], \quad (2.6.1)$$

where we absorbed all the potential terms into \mathcal{V}_p and introduced the covariant derivative $D_j = \partial_j + iqA_j$. The tensor Q_{ij}^α reflects the symmetry of the lattice, and contains the coefficients which indicate the energy cost of having derivatives along certain directions. The index α is the band index, while i, j are spatial indices. In the crystalline frame of reference, all the Q_{ij}^α are diagonal. The superconducting current density $\mathbf{J} = -\delta F / \delta \mathbf{A}$ is affected and becomes

$$J_k = - \sum_{\alpha j} q^2 Q_{kj}^\alpha \left[\frac{1}{q} \text{Im}(\psi_\alpha^* \partial_j \psi_\alpha) + |\psi_\alpha|^2 A_j \right]. \quad (2.6.2)$$

To fully appreciate this model, numerical simulations are essential. However, the London model can provide some hints on the origin of the spontaneous magnetic fields. Let us consider the current density when $\psi_\alpha = |\psi_\alpha^0| e^{i\theta_\alpha}$, with $|\psi_\alpha^0|$ being the uniform ground state value of the α -band, i.e.,:

$$J_k = - \sum_{\alpha i} q^2 |\psi_\alpha^0|^2 Q_{ki}^\alpha \left(\frac{1}{q} \partial_i \theta_\alpha + A_i \right). \quad (2.6.3)$$

Due to the new couplings, we cannot define a unique magnetic penetration depth, hence let us define the tensor $(\hat{\lambda}_\alpha^{-2})_{ij} = q^2 |\psi_\alpha^0|^2 Q_{ij}^\alpha$, yielding

$$\mathbf{J} = - \sum_{\alpha} \hat{\lambda}_\alpha^{-2} \left(\frac{1}{q} \nabla \theta_\alpha + \mathbf{A} \right). \quad (2.6.4)$$

Taking the curl of this expression and using $\nabla \times \mathbf{A} = \mathbf{B}$ we have

$$\mathbf{B} = \nabla \times \left(\hat{\lambda}_L^2 \mathbf{J} \right) - \frac{1}{q} \nabla \times \left(\sum_{\alpha} \hat{\lambda}_L \hat{\lambda}_\alpha^{-2} \nabla \theta_\alpha \right), \quad (2.6.5)$$

where $\hat{\lambda}_L^2 = \left(\sum_{\alpha} \hat{\lambda}_\alpha^{-2} \right)^{-1}$. Assuming not to have windings in any of the components, i.e., $\nabla \times \nabla \theta_\alpha = 0$. One can re-write the magnetic field as

$$\mathbf{B} = \nabla \times \left(\hat{\lambda}_L^2 \mathbf{J} \right) + \frac{1}{q} \sum_{\alpha > \beta} \nabla \times \left[\hat{\lambda}_L \left(\hat{\lambda}_\alpha^{-2} - \hat{\lambda}_\beta^{-2} \right) \nabla (\theta_\alpha - \theta_\beta) \right], \quad (2.6.6)$$

which shows how, in anisotropic materials, gradients of the phase difference can yield spontaneous magnetic fields. When time reversal symmetry is broken and domain walls form, the gradient of the phase difference is not a spatially uniform function, and therefore can lead to spontaneous field, as we show in Paper 1. Finally, is also possible to embed in the anisotropy tensor different pairing symmetries for the different bands. For example, let us consider the following Ginzburg Landau free energy for a two band superconductor

$$F = \int d^3x \left[\frac{1}{2} \sum_{\alpha\beta ij} (D_i \psi_\alpha)^* Q_{ij}^{\alpha\beta} (D_j \psi_\beta) + \mathcal{V}_p + \frac{(\nabla \times \mathbf{A})^2}{2} \right]. \quad (2.6.7)$$

For the free energy to be real, we have $Q_{ij}^{\alpha\beta} = Q_{ji}^{\alpha\beta}$ and $Q_{ij}^{\alpha\beta} = Q_{ij}^{\beta\alpha}$. In this model, having $Q_{xx}^{12} = Q_{yy}^{12}$ leads to an $s + is$ state, while $Q_{xx}^{12} = -Q_{yy}^{12}$ yields an $s + id$ state. This model is the starting point for the study on spontaneous magnetic fields outlined in Paper 1. Moreover, in Paper 1 we determine all the model's parameter following the microscopic derivation outlined in [98, 100].

2.7 Research activity

Paper 1

$\text{Ba}_{1-x}\text{K}_x\text{Fe}_2\text{As}_2$ is a material which spontaneously breaks time reversal symmetry, as claimed by [1, 2] with muon-spin rotation experiments. Moreover, [1, 2] also reported signatures of spontaneous magnetic fields. However, it is still not understood whether $\text{Ba}_{1-x}\text{K}_x\text{Fe}_2\text{As}_2$ is an $s + is$ or an $s + id$ superconductor. In Paper 1, we consider a microscopically derived version [98, 100] of the Ginzburg Landau model in Eq. 2.6.7, describing a two band superconductor with lattice anisotropies and use it to study time reversal symmetry breaking in both $s + is$ and $s + id$ states. Specifically, we investigate the differences in spontaneous magnetic fields generated by domain walls having different orientations with respect to the crystalline axes. We show that, both models, predict spontaneous magnetic fields along the entire length of the domain wall, and we demonstrate the qualitative difference between $s + is$ and $s + id$. Then, we propose a procedure to infer the superconducting order parameter's symmetry based on the measurement of the spontaneous magnetic fields. The rationale is to provide some theoretical insights which can be helpful for scanning SQUID, scanning Hall probes and muon spin rotation experiments [1, 2, 101–103], in determining the order parameter symmetry. The simulations have been carried out using the finite-elements numerical framework FreeFEM [104] and a conjugate gradient flow energy-minimization method.

Paper 2

As we presented in Section 2.3, in type-II superconductors the Meissner state is the global minimum of the single band Ginzburg Landau model, up to the first critical magnetic field H_{c1} . However, it is possible to magnetically superheat a superconductor, namely, maintain the Meissner state for $H > H_{c1}$. This is possible up to the nucleation field H_n , at which vortices nucleate from the boundaries and bring the superconductor to its global minimum, the Shubnikov phase. The process of vortex nucleation can therefore be seen as a free energy barrier which needs to be surpassed [40, 41]. The recent and rapid advancements in the applications of superconductors, such as superconductor-based qubits or single-photon detectors, and superconductive RF cavities [58, 59, 105] pointed the spotlight on the process of vortex nucleation, and in particular on the determination of the nucleation and escape barriers. Being able to numerically predict such quantities, and how they are influenced by the sample geometry, surface roughness and impurity level, would strongly advance the modeling capabilities of real-life devices. However, to solve this problem it is not enough to find the global minimum of a GL functional, but it is necessary to identify the saddle point(s), i.e., the sphaleron(s), of the minimum free energy path connecting two minima, of which, one is the global minimum. Once the possible sphalerons configurations are found, it is possible to accurately compute the desired free energy barriers, without the uncontrollable approximations introduced by pre-existing methods, such as the Bean-Livingston model [41]. To

achieve this, we present a generalization of the simplified string method [3], which we named *gauged* string method, that allows the calculation of the sphalerons in a gauge theory, such as the one component GL model in Eq. 2.1.1. Moreover, since we take into account all the non-linearities present in the model, we present few examples of how the nucleation barrier is affected by the presence of complex geometries, surface roughness, pinning sites and multiple nucleations.

In the next chapter we outline the specifics of the gauged string method.

Paper 3

Most of the superconductors of current interest are multiband materials [1, 2, 23–25, 29, 32, 33, 39, 70, 106]. As we saw in Section 2.5, in a multiband superconductors, quantum vortex can be fractional or composite. A fractional vortex is energetically more expensive than a composite vortex due to a logarithmically divergent energy term. Hence, fractional vortices in different components interact, via the magnetic field and/or the Josephson coupling to form a composite vortex, which is energetically stable. This type of vortex formation has a more complicated nucleation process than in a single band superconductor, since it possible that the fractional vortices in different components nucleate in non-trivial sequences. Hence, being able to accurately calculate the nucleation free energy barrier plays a crucial role in accurately understanding the nucleation processes. Moreover, the existence of a second superconducting component, introduces more metastable states of the Ginzburg Landau energy functional, increasing the number of processes featuring saddle points, and therefore potential barriers to overcome. Metastable solutions of fractional vortices have been shown within the London model [76] and within the Ginzburg Landau theory [77], but no calculation of nucleation barriers has ever been attempted. In this paper we extend the gauged string method to a two-component superconductor, with Josephson interactions as well as spatial anisotropies. In this way, we are able to accurately study the nucleation free-energy barriers in the nucleation processes of fractional and composite vortices, and how lattice anisotropies influence them. Since the investigation is numerical, we are able to circumvent all the limitations introduced by the London limit and by the multiband version of Bean Livingston model. Then, we study the effect that intercomponent interactions, such as the Josephson potential terms, have on the nucleation process and on the critical magnetic fields.

Chapter 3

Navigating uncharted energy landscapes: The gauged string method

In this chapter we dive into the process of numerically computing the free energy barriers for events such as the nucleation of a vortex. In a magnetically super-heated superconductor, the vortex nucleation is a remarkable example of metastable state decay. For such process, one can define the transition rate

$$\tau^{-1} = A \exp\left(\frac{\Delta E}{k_B T}\right). \quad (3.0.1)$$

A is the so called *attempt rate* and depends on the determinant of the Hessian of the system. Its calculation requires a field theory extension of Kramers-Langer's theory [53, 107–111]. In the current thesis, we focus instead on the numerical determination of ΔE , which is the energy barrier which needs to be surpassed to achieve the transition. For a field, the peak of the energy barrier corresponds to an infinite-dimensional saddle point of the free energy functional which is called *sphaleron*, from the Greek word for "slippery". To find the sphaleron between two states, one has to determine first the Minimum Energy Path (MEP) between them, and then, identify its maximum. The minimum energy path is defined as the path in the configuration space which connects the initial and final states by crossing in each point the minimum of the free energy cotangent space. Hence, finding the sphaleron means finding the MEP between two states, and to achieve this, there are two main options: *chain-of-states* methods and the *string methods*. The most utilised chain-of-state method is the Nudge Elastic Band method [112, 113], in which a chain of systems, named *frames* is considered. The frames are copies of the initial system, with an additional synthetic potential applied, with the purpose of acting as a spring force between adjacent states. In this way, the energy of each frame is

minimised, and the result is the minimum free energy path. On the one hand, the presence of the fictitious spring potentials prevents all the frame from collapsing in the free energy minima, on the other hand it modifies the Hamiltonian of the system, which makes the implementation of this method extremely delicate.

The second class of methods, the string methods, are based on the minimization of the free energy, constrained to its cotangent space F_{\perp} , i.e.,

$$\mathbf{q}(s) = \arg \min F_{\perp}[\mathbf{q}(s)], \quad (3.0.2)$$

where \mathbf{q} is the system's configuration and s its parametrization. This method was initially presented in [114], with the first application to a one-dimensional Ginzburg-Landau model realized in [115]. In this chapter, we present the structure of the string method and its extension to local $U(1)$ gauge theories.

3.1 The String Method: an overview

The fundamental idea of the string method is to evolve a curve, between two minima separated by a sphaleron. Each point of the curve corresponds to a configuration of the physical system. To do so, we consider a system described by the free energy $F(\mathbf{q})$, where a configuration of the system is represented by the vector \mathbf{q} . Let us then consider a certain path in the configuration space $\mathbf{q}(s, t)$ parametrized by $s \in [0, 1]$ and by the pseudo-time t . To obtain the minimum free energy path, we have to evolve $\mathbf{q}(s, t)$ according to

$$\frac{d}{dt} \mathbf{q}(s, t) = -\nabla F(\mathbf{q}(s, t))_{\perp} + r(s, t) \boldsymbol{\tau}(s, t), \quad (3.1.1)$$

where $\boldsymbol{\tau} = \frac{\partial \mathbf{q}}{\partial s}$ is the tangent vector to the trajectory of the system, and $\nabla F(\mathbf{q}(s, t))_{\perp}$ is the gradient of the free energy in the cotangent space, i.e.,

$$\nabla F(\mathbf{q}(s, t))_{\perp} = \nabla F(\mathbf{q}(s, t)) - [\nabla F(\mathbf{q}(s, t)) \cdot \boldsymbol{\tau}] \boldsymbol{\tau}. \quad (3.1.2)$$

In this way, when $\nabla F(\mathbf{q}(s, t))_{\perp} = 0$, the minimum free energy path is achieved and the force acting on the system only influences the parametrization of the MEP as it is directed along the tangential direction $\boldsymbol{\tau}$. $r(s, t)$ is a Lagrange multiplier which allows to set the string parametrization, which is chosen to be an equal-arc length parametrization with $\mathbf{q}(0)$ and $\mathbf{q}(1)$, respectively, initial and final minima configurations. It is important to notice that, the forces acting in the tangential direction to the string, have no effects on its shape, but only on the parametrization, which is a degree of freedom of the model. An alternative definition to identify the minimum free energy path is

$$\left\| \nabla f \cdot \frac{\partial \mathbf{q}}{\partial s} \right\| = \left\| \nabla f \right\| \left\| \frac{\partial \mathbf{q}}{\partial s} \right\|, \quad \forall s \in [0, 1]. \quad (3.1.3)$$

The minimum free energy path identified by Eq. 3.1.1 does not correspond to the real dynamics of the system, but indicates the most energetically favorable set of

configurations to go from the initial state to the final one. More details on the string method are reported in [114].

From a numerical view-point, the computation of the free energy gradient in the cotangent space is problematic, due to arising numerical instabilities. It is in fact necessary to utilize an unwinding scheme to compute the tangent vector along the curve, which results in different computations before and after the saddle point. As explained in [3, 114, 116], this requirement lowers the accuracy of the simulation, however it can be easily bypassed by reformulating Eq. 3.1.1, and by using the freedom in the parametrization choice.

3.1.1 The simplified string method

The *simplified string method*, first introduced in [3] is based on the reformulation of Eq. 3.1.1 as

$$\frac{d}{dt}\mathbf{q}(s,t) = -\nabla F(\mathbf{q}(s,t)) + \tilde{r}(s,t)\boldsymbol{\tau}(s,t), \quad (3.1.4)$$

where

$$\tilde{r}(s,t) = r(s,t) + \nabla F(\mathbf{q}(s,t)) \cdot \boldsymbol{\tau} \quad (3.1.5)$$

still plays the role of a Lagrange multiplier, which is automatically determined by the numerical algorithm in a procedure called *reparametrization*. In this way, we can avoid the numerical calculation of the free energy gradient in the cotangent space, and achieve higher computational accuracy. The procedure to implement the simplified string method is outlined in the following.

Let us discretize the minimum energy path curve $\mathbf{q}(s)$ in N frames $\{\mathbf{q}_n\}_{n=0}^{N-1}$ such that $\mathbf{q}_n = \mathbf{q}\left(\frac{n}{N-1}\right)$ are sampled equally spaced in the parametrization parameter s . The algorithm is an iterative procedure where, at each iteration, a minimization and reparametrization steps are performed. In the minimization phase, a fixed number of steepest gradient descent are performed. This has the effect of moving each frame towards the closest minimum, i.e., it changes the locations of the frames along the string $\mathbf{q}(s)$. In the reparametrization phase, the displaced frames are interpolated, either by linear or spline interpolation, with a new curve as the result. Along the newly interpolated string, a new set of equally distanced frames is identified, and the procedure repeated. To compute the distance between frames consistently, we need define a metric, which depends on the physical properties of the system. To present this procedure in further details, let us introduce $\mathbf{q}_n^{i,k}$, as the n -th frame, at iteration i and minimization step k . The simplified string method then works as follows:

- **Minimization**

In this phase, we perform N_m gradient descent minimization steps on each frame $\mathbf{q}_n^{i,k}$ following

$$\mathbf{q}_n^{i,k+1} = \mathbf{q}_n^{i,k} + \beta_n^{i,k} \mathbf{g}_n^{i,k}, \quad (3.1.6)$$

where $\beta_n^{i,k}$ is the step length and $\mathbf{g}_n^{i,k}$ the steepest descent direction. Once the minimization step is completed, each frame has been displaced, yielding the new set of frames $\{\tilde{\mathbf{q}}_n^{i,1}\} = \{\mathbf{q}_n^{i,N_m}\}$.

- **Reparametrization**

The key element of this phase is to compute the distance between the frames $\tilde{\mathbf{q}}_n^{i,1}$, hence let $\|\cdot\|$ be the norm defined with respect to a chosen metric. Then, we can calculate the displacement between adjacent frames as $\Delta s_n = \|\tilde{\mathbf{q}}_n^{i,1} - \tilde{\mathbf{q}}_{n-1}^{i,1}\|^2$. Hence, we can compute the position of each frame along the string, i.e., the parametrization of the curve as

$$s_n = \frac{\sum_{p=1}^n \Delta s_p}{\sum_{p=1}^{N-1} \Delta s_p}. \quad (3.1.7)$$

In this way each frame $\tilde{\mathbf{q}}_n$ is associated to a coordinate s_n . Using the couple $(s_n, \tilde{\mathbf{q}}_n)$ we perform a polynomial interpolation (linear or spline), obtaining the interpolating string $\hat{\mathbf{q}}_n^{i,1}$. Hence, we sample the set of equally spaced N frames on the newly parametrized string

$$\mathbf{q}_n^{i+1,1} = \hat{\mathbf{q}}_n^{i,1} \left(\frac{n}{N-1} \right), \quad (3.1.8)$$

which becomes the input to the minimization step. This reparametrization procedure effectively computes the Lagrange multiplier in Eq. 3.1.4, and allows a numerically efficient and accurate solution. The choice between spline interpolation and linear interpolation is principally related to the number of frames utilised. In our implementation on Graphical Processing Units, working with linear interpolation and a higher number of frames has proven to be the most effective solution.

3.1.2 The gauged string method

As we will see in the next section, applying the string methods to mechanical systems is rather straightforward. However, its application to continuous field theories and fields living in infinite-dimensional Hilbert spaces, entails some technical difficulties. Among these, the most remarkable is the definition of the metric to compute Δs_n .

In the case of a single particle in a potential, where the state of the system $\mathbf{q} = \mathbf{x}(s, t)$ is represented by its position, the most natural metric is the Euclidian distance between the positions at various frames. In our case instead, we apply the simplified string method to a Ginzburg Landau model, where the state of the system is fully described by the superconducting order parameter $\psi(\mathbf{x})$ and the vector potential $\mathbf{A}(\mathbf{x})$, i.e., $\mathbf{q} = (\psi, \mathbf{A})$. Hence, to calculate the distance between adjacent frames, we need to define a metric which takes into account the differences

between the fields of adjacent frames. To do so, there are multiple choices, the simplest of which is to define

$$\Delta s_n^{\text{gd}} = \left(\|\mathbf{A}_n - \mathbf{A}_{n-1}\|^2 + \|\psi_n - \psi_{n-1}\|^2 \right), \quad (3.1.9)$$

where $\|\cdot\|$ is the L^2 norm, where the summed components correspond to the spatially discretized values of the fields at frame n . The problem rising with the choice of this metric is its intrinsic gauge dependence. Since the Ginzburg Landau model is gauge invariant it is important to maintain the metric gauge invariant as well. In fact, it can happen that the system evolves in the gauge degrees of freedom, yielding the so called *gauge twisting*. In this situation, the string evolves in a set of configurations which correspond to the same physical state. To avoid this, we can introduce the gauge invariant metric

$$\Delta s_n^{\text{ph}} = \left(\|\mathbf{B}_n - \mathbf{B}_{n-1}\|^2 + \|\mathbf{J}_n - \mathbf{J}_{n-1}\|^2 \right), \quad (3.1.10)$$

which calculates the distance between physically relevant quantities. By doing so we prevent gauge twisting from happening, obtaining more accurate results. Moreover, it is possible to weight differently the distance $\|\mathbf{B}_n - \mathbf{B}_{n-1}\|^2$ and $\|\mathbf{J}_n - \mathbf{J}_{n-1}\|^2$, however we found that it does not affect the shape of the minimum free energy path, but influences only the numerical performances. Fig. 3.1 shows a free energy barrier with respect to a certain minimum energy path between two minima of the GL free energy. The blue curve is computed using the gauge dependent metric Δs_n^{gd} while the green curve utilizes Δs_n^{ph} . We can see the gauge twisting happening in the initial part of the blue curve, which is highlighted in red. Since the green curve employs a "physical" metric, the gauge twisting does not occur. Finally, it is important to note that in both cases the height of the free energy barrier is the same, which means that both metrics yield correct results. However, employing a gauge invariant metric results in better performances, and more accurate field configurations along the minimum free energy path.

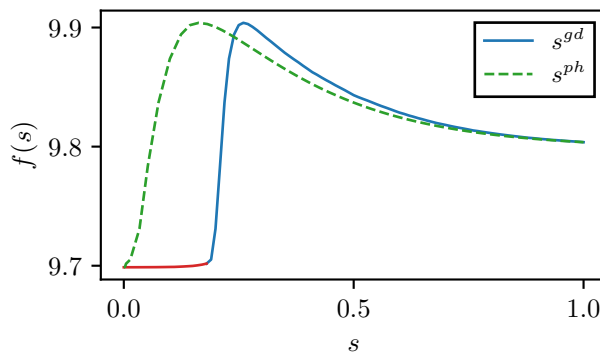


Figure 3.1: The figure displays gauge twisting happening in a energy barrier calculation. If the minimum free energy path is computed using the gauge dependent metric Δs_n^{gd} (blue curve), the initial part of the barrier (highlighted in red) sees the string evolving in the gauge degrees of freedom, yielding the same physical state. When the minimum free energy path is calculated using the gauge invariant metric Δs_n^{ph} , the string corresponding to the minimum energy path does not twist in the gauge degrees of freedom. $f(s)$ represents the free energy as a function of the string parametrization s . The image is taken from [7].

3.2 Application to a mechanical system

In this section we provide an example of the simplified string method applied to a two dimensional mechanical system composed by a single particle subjected to the Müller-Brown potential $V(\mathbf{x})$, shown in Fig. 3.2. This potential is particularly useful for this example, since it contains two deep minima, which are separated by saddle points. Moreover, the potential grows as one gets closer to the boundary, which ensures that the system evolution remains confined within the bulk. The state

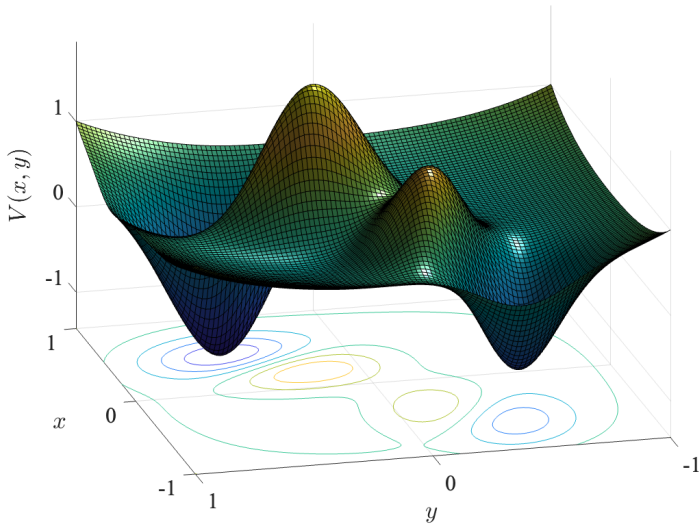


Figure 3.2: Müller-Brown-like potential landscapes used in the current example.

of the system $\mathbf{q} = \mathbf{x}$ is equal to the position of the particle, and once discretized, each frame $\{\mathbf{q}_n\} = \{\mathbf{x}_n\}$ is the position of the particle along the string at s_n . In this case, the metric used in the reparametrization step is given by the Euclidean distance

$$\Delta s_n = |x_n - x_{n-1}|^2 + |y_n - y_{n-1}|^2. \quad (3.2.1)$$

To start the minimization procedure, we have to provide an initial guess for each frame composing the string. We do so by identifying the shortest possible path between the two minima, which, as shown in Fig. 3.3, is one of the highest energy paths. It is important to note that the string is defined on the xy -plane and is represented by a red line. The white string following the potential surface $V(x, y)$ is for illustrative purposes only, as it highlights its evolution towards the potential valley. Now, we let the system evolve. Each frame does two steps of steepest descent minimization, and then the string is reparametrized. After 10 iterations, the string evolves to Fig. 3.4 and we can notice that it starts descending towards the valley

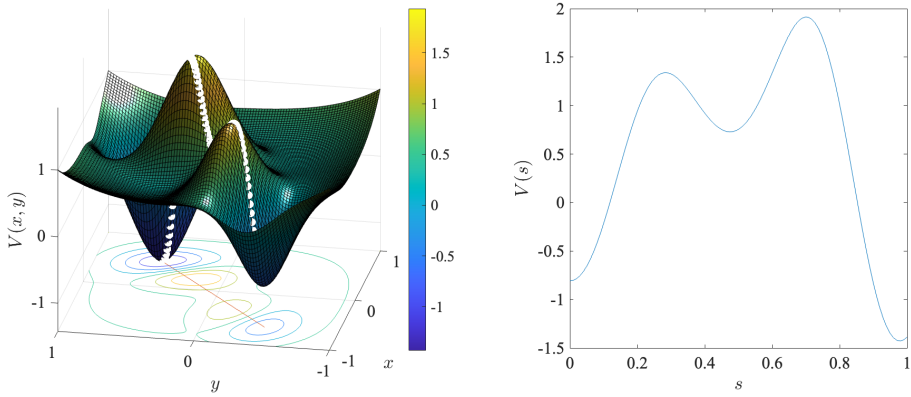


Figure 3.3: Initial guess for the $N = 100$ frames $\{\mathbf{x}_n\}$ composing the string. In this configuration, the string, displayed in red, is the shortest path connecting the two minima. It is important to note, that the string is defined on the xy -plane. We plot it following $V(x, y)$ surface for illustrative purposes only, as it highlights its evolution towards the potential valley.

of the potential landscape. Finally, we let the system evolve until full convergence,

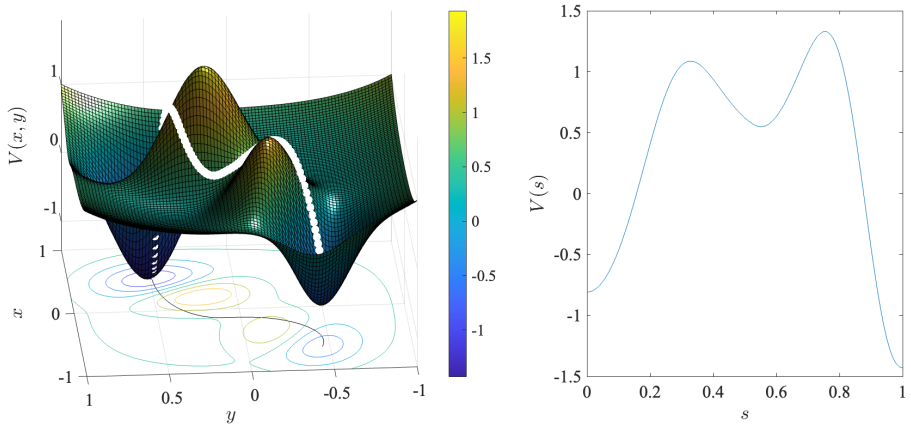


Figure 3.4: State of the system after ten iterations of (minimization + reparametrization). It is possible to see that the string is moving towards the potential valley, where the gradient of the potential in the cotangent space is zero.

i.e., around one hundred iterations. To check the convergence is achieved, we can compute the cotangent potential for each frame, and ensure it is smaller than a

threshold value. The converged state is shown, in black, in Fig. 3.5 and we can see how the string lies at the very bottom of the potential valley. Comparing the

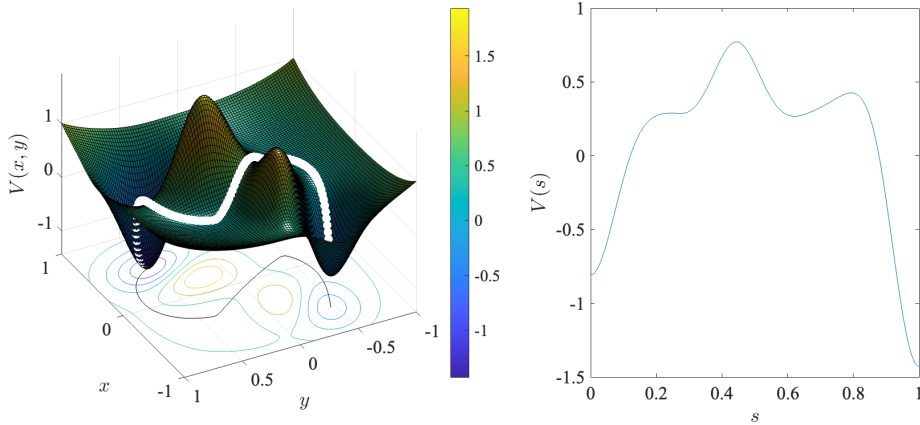


Figure 3.5: State of the system after the convergence of the (minimization + reparametrization) steps. It is possible to see that the string lies in the potential valley, where the gradient of the potential in the cotangent space is zero.

string shown in Fig. 3.3 and in Fig. 3.5, we can notice that the minimum free energy path connecting two minima does not correspond, in general, to the shortest path between them. Finally, we notice that in this minimum energy path, we have more than a single sphaleron, as there are multiple energy maxima along the minimum energy path. In Paper 2, we present further details on how we apply this method to the Ginzburg-Landau theory.

Chapter 4

Safari in the microscopic world

4.1 The mean field theory

In this chapter, we introduce the theoretical framework which represents the core part of my research activity, namely the mean field theory for the Hubbard model. We utilize the attractive Hubbard model, together with the mean field approximation to describe superconductivity at a microscopic scale in crystalline structures. We do so in real space, and within the tight-binding approximation, where the electron wave functions are localized near the lattice ions. While the derivation of the many body Hamiltonian from the full crystal Hamiltonian can be found in [117], we focus on explaining how the mean field approximation is carried out, and introduce the formalism I utilize in my research. To do so, let us start from the most general version of a quartic Hamiltonian in a d -dimensional hypercubic lattice, i.e.,:

$$H = \sum_{ij} \varepsilon_{ij} c_i^\dagger c_j + \sum_{ijkl} v_{ijkl} c_i^\dagger c_j^\dagger c_l c_k, \quad (4.1.1)$$

where c_i and c_i^\dagger are the fermionic annihilation and creation operators at site i , with the anti-commutation relations $\{c_i, c_j\} = 0$ and $\{c_i, c_j^\dagger\} = \delta_{ij}$. ε_{ij} is a general hopping term and v_{ijkl} the potential coupling for the quartic interaction. Moreover, for the Hamiltonian to be real, we have $\varepsilon_{ij}^* = \varepsilon_{ji}$ and $v_{ijkl} = v_{lkji}^*$. By considering the anticommutation relations, one can show the additional symmetry $v_{ijkl} = v_{lkji}^* = v_{klij}^*$. The indices i, j contain the position on the N -points hypercubic lattice, as well as other degrees of freedom, such as the spin of the particle. We utilize this convention to maintain the upcoming derivations as general as possible, then, we will provide some more specific examples.

As of now, Eq. 4.1.1 has no analytical solution. Neglecting the spin degree of freedom, in each site, it is possible to have one or zero particles, which means that,

per site, we have two possible states. Hence for a system with N lattice points, the number of available states is 2^N , which makes an exact solution of the Hamiltonian numerically impossible on classical computers. A very successful approximation, to treat a quartic Hamiltonian, consists of the *mean field theory* approximation. In this context, each particle is assumed to interact with a mean field, instead of all the other particles, and the Hamiltonian is reduced to a quadratic form, which is more easily treatable. In the next sections we present the details of such approximation as well as its limitations. Another possible method to solve the quartic models, despite some limitations, employs state of the art diagrammatic Monte Carlo techniques, e.g., [118].

4.2 The variational approach

The first approach one can utilize to perform a mean field approximation, on the quartic Hamiltonian of Eq. 4.1.1, is the variational method, which follows the procedure

1. Define a mean field Hamiltonian \mathcal{H}_{MF} with the necessary variational parameters.
2. Compute the free energy Ω_{MF} of the Hubbard Hamiltonian, using the quadratic mean-field Hamiltonian \mathcal{H}_{MF} in the density matrix calculation.
3. Minimize the free energy Ω_{MF} with respect to the variational parameters.
4. Insert the obtained variational parameters in \mathcal{H}_{MF} .
5. Diagonalize \mathcal{H}_{MF} .

In this way, one obtains the best possible approximating mean field quadratic Hamiltonian of the full quartic model.

Let us start by defining the various players which we are going to use; the exact free energy of the quartic Hamiltonian is given by

$$\Omega(H, \rho) = U - TS = \text{Tr} \left(\rho(H + \beta^{-1} \log \rho) \right), \quad (4.2.1)$$

where $U = \text{Tr}(\rho H)$ is the system internal energy, $S = -\text{Tr}(\rho \log \rho)$ the entropy, and ρ the density matrix, defined as

$$\rho = \frac{e^{-\beta H}}{Z(H)}. \quad (4.2.2)$$

H is the Hubbard Hamiltonian introduced in Eq. 4.1.1, Z the partition function, and $\beta = 1/T$, with T being the temperature¹. However, since we are not able to

¹We work in natural units

diagonalize H we cannot compute this free energy. Therefore, we define the mean field Hamiltonian

$$\mathcal{H}_{MF} = \sum_{ij} h_{ij} c_i^\dagger c_j + \frac{1}{2} \sum_{ij} (\Delta_{ij} c_i^\dagger c_j^\dagger + \Delta_{ij}^* c_j c_i), \quad (4.2.3)$$

with $h_{ij}^* = h_{ji}$ and $\Delta_{ij} = -\Delta_{ji}$ being the variational parameters. Then, we compute the mean field free energy

$$\Omega(H, \rho_{MF}) = \text{Tr} \left(\rho_{MF} (H + \beta^{-1} \ln \rho_{MF}) \right). \quad (4.2.4)$$

ρ_{MF} is a density matrix of the form of Eq. 4.2.2 but computed using \mathcal{H}_{MF} . One can show that $\Omega(H, \rho_H) \leq \Omega(H, \rho_{MF})$, hence the free energy in the mean field approximation is always higher than the true free energy. Nonetheless, once Ω_{MF} is computed, we determine the variational parameters h_{ij} and Δ_{ij} by

$$(h_{ij}, \Delta_{ij}) = \arg \min \Omega(H, \rho_{MF}). \quad (4.2.5)$$

We begin by diagonalizing the mean field Hamiltonian, so that we are able to compute the density matrix ρ_{MF} . To do so, let us introduce the Nambu representation

$$\Phi_i = \begin{pmatrix} c_i \\ c_i^\dagger \end{pmatrix}, \quad (4.2.6)$$

which allows us to write the mean field Hamiltonian as

$$\mathcal{H}_{MF} = \frac{1}{2} \sum_{ij} \Phi_i^\dagger \begin{pmatrix} h_{ij} & \Delta_{ij} \\ \Delta_{ji}^* & -h_{ij}^* \end{pmatrix} \Phi_j + \frac{1}{2} \sum_i h_{ii}, \quad (4.2.7)$$

which is also known as Bogoliubov-de Gennes (BdG) Hamiltonian. By introducing the vector notation $\Phi = (c_1, \dots, c_N, c_1^\dagger, \dots, c_N^\dagger)^T$, we obtain

$$\mathcal{H}_{MF} = \frac{1}{2} \Phi^\dagger \underbrace{\begin{pmatrix} h & \Delta \\ \Delta^\dagger & -h^T \end{pmatrix}}_{=\mathcal{H}} \Phi + \frac{1}{2} \text{Tr} h. \quad (4.2.8)$$

Hence, to diagonalize \mathcal{H}_{MF} we need to diagonalize \mathcal{H} , which is a $2N \times 2N$ matrix composed by the $N \times N$ submatrices h and Δ . To do so, let us introduce the unitary Bogoliubov transformation $\gamma = U^\dagger \Phi$ so that $\mathcal{H} = U \mathcal{D} U^\dagger$, where \mathcal{D} is diagonal. The γ_n -operators diagonalize the Hamiltonian, and have fermionic anticommutation relations, hence they describe quasiparticles following Fermi-Dirac statistics:

$$\langle \gamma_n^\dagger \gamma_m \rangle = \delta_{n,m} f(E_n), \quad f(E) = (1 + e^{\beta E})^{-1}. \quad (4.2.9)$$

where $f(\mathcal{H})$ is defined as $f(\mathcal{H}) = f(UDU^\dagger) = Uf(\mathcal{D})U^\dagger$, with the property $f(-\mathcal{H}) = \mathbf{1} - f(\mathcal{H})$. Doing the same calculations for the all the relevant thermal averages, one obtains:

$$\begin{aligned}\langle c_i^\dagger c_j \rangle &= \mathbf{e}^T(j) f(\mathcal{H}) \mathbf{e}(i) = \mathbf{h}^T(i) f(-\mathcal{H}) \mathbf{h}(j) \\ \langle c_i^\dagger c_j^\dagger \rangle &= \mathbf{h}^T(j) f(\mathcal{H}) \mathbf{e}(i) \\ \langle c_i c_j \rangle &= \mathbf{e}^T(j) f(\mathcal{H}) \mathbf{h}(i).\end{aligned}\tag{4.2.22}$$

With the thermal averages written down, we can start computing the mean field free energy in Eq. 4.2.4. Starting from $\text{Tr}(\rho_{MF}H)$,

$$\text{Tr}(\rho_{MF}H) = \sum_{ij} \varepsilon_{ij} \langle c_i^\dagger c_j \rangle + \sum_{ijkl} v_{ijkl} \langle c_i^\dagger c_j^\dagger c_l c_k \rangle,\tag{4.2.23}$$

where the thermal average is done with respect to the mean field Hamiltonian. Since the mean field Hamiltonian is quadratic, we can apply the Wick decomposition. Together with c_i, c_j^\dagger commutation relation and the symmetry properties of v_{ijkl} , we obtain

$$\text{Tr}(\rho_{MF}H) = \sum_{ij} \varepsilon_{ij} \langle c_i^\dagger c_j \rangle + \sum_{ijkl} v_{ijkl} \left(\langle c_i^\dagger c_j^\dagger \rangle \langle c_l c_k \rangle + 2 \langle c_i^\dagger c_k \rangle \langle c_j^\dagger c_l \rangle \right).\tag{4.2.24}$$

Then, we introduce the notation of Eq. 4.2.22 into Eq. 4.2.24, obtaining

$$\begin{aligned}\text{Tr}(\rho_{MF}H) &= \frac{1}{2} \varepsilon_{ij} [\mathbf{e}^T(j) f(\mathcal{H}) \mathbf{e}(i) + \mathbf{h}^T(i) f(-\mathcal{H}) \mathbf{h}(j)] + \\ &+ 2v_{ijkl} [\mathbf{e}^T(k) f(\mathcal{H}) \mathbf{e}(i)] [\mathbf{h}^T(j) f(-\mathcal{H}) \mathbf{h}(l)] + \\ &+ v_{ijkl} [\mathbf{h}^T(j) f(\mathcal{H}) \mathbf{e}(i)] [\mathbf{e}^T(k) f(\mathcal{H}) \mathbf{h}(l)].\end{aligned}\tag{4.2.25}$$

We can now calculate the entropy term of the free energy in Eq. 4.2.4, namely

$$\text{Tr}\{\rho_{MF} \ln \rho_{MF}\} = \sum_{n=1}^{2N} f(\mathcal{D}_n) \ln f(\mathcal{D}_n) = \text{Tr}(f(\mathcal{H}) \ln f(\mathcal{H})).\tag{4.2.26}$$

We are now ready to minimize the free energy Ω with respect to the variational parameters h_{ij} and Δ_{ij} , to find the best approximating BdG Hamiltonian. We can notice that, both Eq. 4.2.24 and Eq. 4.2.26 depend on h_{ij} and Δ_{ij} through $f(\mathcal{H})$, hence we can perform a variation in Eq. 4.2.4 with respect to $f(\mathcal{H})$, i.e., $\delta_f \Omega(H, \rho_{MF}) = \delta_f \text{Tr}(\rho_{MF}H) + \beta^{-1} \delta_f \text{Tr}(\rho_{MF} \ln \rho_{MF}) = 0$, obtaining (using the

Einstein summation convention on repeated indices)

$$\begin{aligned}
\delta_f \Omega(H, \rho_{MF}) &= \left[\frac{\varepsilon_{ij}}{2} + 2v_{ikjl} \mathbf{h}^T(k) f(-\mathcal{H}) \mathbf{h}(l) - \frac{h_{ij}}{2} \right] \mathbf{e}^T(j) \delta f \mathbf{e}(i) \\
&+ \left[v_{ijkl} \mathbf{e}^T(k) f(\mathcal{H}) \mathbf{h}(l) - \frac{\Delta_{ij}}{2} \right] \mathbf{h}^T(j) \delta f \mathbf{e}(i) \\
&+ \left[v_{lkji} \mathbf{h}^T(k) f(\mathcal{H}) \mathbf{e}(l) - \frac{\Delta_{ij}^*}{2} \right] \mathbf{e}^T(j) \delta f \mathbf{h}(i) \\
&+ \left[-\frac{\varepsilon_{ij}}{2} - 2v_{ljki} \mathbf{e}(k) f(\mathcal{H}) \mathbf{e}(l) + \frac{h_{ij}}{2} \right] \mathbf{h}^T(i) \delta f \mathbf{h}(j) \\
&= 0.
\end{aligned} \tag{4.2.27}$$

Since the variation δf is arbitrary, Eq. 4.2.27 gives us the equations defining the variational parameters

$$\begin{aligned}
h_{ij} &= \varepsilon_{ij} + 4 \sum_{kl} v_{ikjl} \mathbf{h}^T(k) f(-\mathcal{H}) \mathbf{h}(l) \\
\Delta_{ij} &= 2 \sum_{kl} v_{ijkl} \mathbf{e}^T(k) f(\mathcal{H}) \mathbf{h}(l) \\
\Delta_{ij}^* &= 2 \sum_{kl} v_{lkji} \mathbf{h}^T(k) f(\mathcal{H}) \mathbf{e}(l) \\
h_{ij} &= \varepsilon_{ij} + 4 \sum_{kl} v_{ljki} \mathbf{e}^T(k) f(\mathcal{H}) \mathbf{e}(l),
\end{aligned} \tag{4.2.28}$$

which can be summarized in the following two self consistent equations²

$$U_{ij} = 4 \sum_{kl} v_{ikjl} \mathbf{h}^T(k) f(-\mathcal{H}) \mathbf{h}(l) \tag{4.2.29}$$

$$= 4 \sum_{kl} v_{ikjl} \mathbf{e}^T(l) f(\mathcal{H}) \mathbf{e}(k) \tag{4.2.30}$$

$$\Delta_{ij} = 2 \sum_{kl} v_{ijkl} \mathbf{e}^T(k) f(\mathcal{H}) \mathbf{h}(l). \tag{4.2.31}$$

By using the definition of $f(\mathcal{H})$ together with Eq. 4.2.22, it is straightforward to prove that Eq. 4.2.30 and Eq. 4.2.31 are equal to

$$\Delta_{ij} = 2 \sum_{kl} v_{ijkl} \langle c_l c_k \rangle, \quad U_{ij} = 4 \sum_{kl} v_{ikjl} \langle c_k^\dagger c_l \rangle, \tag{4.2.32}$$

which are well known relations in this model. Physically, Δ_{ij} represents the superconducting gap field, while U_{ij} is the Hartree field.

²To do so we use the symmetries of v_{ijkl} , and Eq. 4.2.22

4.2.1 The Hubbard model

Let us consider the attractive Hubbard Hamiltonian for a system of spin-1/2 fermions in a two-dimensional square lattice with N points in the presence of a gauge field

$$H = \sum_{ij\sigma} t_{ij\sigma} c_{i\sigma}^\dagger c_{j\sigma} - V \sum_i c_{i\uparrow}^\dagger c_{i\downarrow}^\dagger c_{i\downarrow} c_{i\uparrow}, \quad (4.2.33)$$

where i, j label the lattice site, $\sigma = \uparrow, \downarrow$ labels the particle spin, $V > 0$ is the coupling potential strength, and $t_{ij\sigma}$ reads

$$t_{ij\sigma} = -\delta_{|i-j|,1} e^{iqA_{ij}} - \delta_{ij} \mu_\sigma. \quad (4.2.34)$$

The hopping is allowed between nearest neighboring sites and the model is rescaled to have unitary hopping energy, μ_σ is the effective chemical potential, which is defined as $\mu_\sigma = \mu + \sigma h_z$, where h_z is the Zeeman field. Finally, the phase term $\exp(iqA_{ij})$ accounts for interaction with the magnetic vector potential \mathbf{A} through Peierls substitution; q is the effective electrical charge and A_{ij} reads

$$A_{ij} = \int_j^i \mathbf{A} \cdot d\boldsymbol{\ell}. \quad (4.2.35)$$

With the method developed in the previous section we can perform the mean field approximation of Eq. 4.2.33. As a first thing, we map the indices of Eq. 4.1.1 as $i \rightarrow (i, \sigma)$, and write the hopping coefficient ε_{ij} and the potential v_{ijkl} as

$$\varepsilon_{i\sigma ij\sigma_j} = t_{ij} \delta_{\sigma_i \sigma_j} \quad (4.2.36)$$

$$v_{i\sigma ij\sigma_j k\sigma_k l\sigma_l} = -\frac{V}{4} \delta_{i, \{j, k, l\}} (\delta_{\uparrow\downarrow\uparrow\downarrow} + \delta_{\downarrow\uparrow\downarrow\uparrow} - \delta_{\uparrow\downarrow\downarrow\uparrow} - \delta_{\downarrow\uparrow\uparrow\downarrow}), \quad (4.2.37)$$

obtaining in this way Eq. 4.2.33. Following this mapping, we have $\mathbf{e}(i), \mathbf{h}(i) \rightarrow \mathbf{e}_\sigma(i), \mathbf{h}_\sigma(i)$ and we immediately obtain the self consistency equations from Eq. 4.2.29, namely

$$\begin{aligned} \Delta_{i\uparrow\downarrow} &= -V \mathbf{e}_\uparrow^T(i) f(\mathcal{H}) \mathbf{h}_\downarrow(i) \\ U_{i\uparrow\uparrow} &= -V \mathbf{h}_\uparrow^T(i) f(-\mathcal{H}) \mathbf{h}_\downarrow(i) \\ U_{i\downarrow\downarrow} &= -V \mathbf{e}_\uparrow^T(i) f(\mathcal{H}) \mathbf{e}_\uparrow(i) \\ U_{i\uparrow\downarrow} &= V \mathbf{e}_\downarrow^T(i) f(\mathcal{H}) \mathbf{e}_\uparrow(i) \\ U_{i\downarrow\uparrow} &= V \mathbf{e}_\uparrow^T(i) f(\mathcal{H}) \mathbf{e}_\downarrow(i), \end{aligned} \quad (4.2.38)$$

where we used the symmetry $\Delta_{i\uparrow\downarrow} = -\Delta_{i\downarrow\uparrow}$ together with $\mathbf{e}_\downarrow^T(i) f(\mathcal{H}) \mathbf{h}_\uparrow(i) = -\mathbf{e}_\uparrow^T(i) f(\mathcal{H}) \mathbf{h}_\downarrow(i)$ to simplify the gap expression. In this case, the matrix \mathcal{H} reads

$$\mathcal{H} = \begin{pmatrix} h_\uparrow & 0 & 0 & \Delta_{\uparrow\downarrow} \\ 0 & h_\downarrow & \Delta_{\downarrow\uparrow} & 0 \\ 0 & \Delta_{\downarrow\uparrow}^\dagger & -h_\uparrow^T & 0 \\ \Delta_{\uparrow\downarrow}^\dagger & 0 & 0 & -h_\downarrow^T \end{pmatrix}, \quad (4.2.39)$$

which is block diagonal and composed by the two sub-matrices

$$\mathcal{H}_1 = \begin{pmatrix} h_\uparrow & \Delta_{\uparrow\downarrow} \\ \Delta_{\uparrow\downarrow}^\dagger & -h_\downarrow^T \end{pmatrix}, \quad \mathcal{H}_2 = \begin{pmatrix} h_\downarrow & \Delta_{\downarrow\uparrow} \\ \Delta_{\downarrow\uparrow}^\dagger & -h_\uparrow^T \end{pmatrix}. \quad (4.2.40)$$

These two sub-matrices have the same set of eigenvalues, and are completely decoupled, which means that it is enough to utilize one to fully solve Eq. 4.2.33, in the mean field approximation. The block structure of \mathcal{H} is maintained by $f(\mathcal{H})$ which allows us to quickly deduce which self consistency equations, among those in Eq. 4.2.38, are necessary to solve the problem. To do so, let us see which sub-matrix the different $\mathbf{e}_\sigma(i)$ and $\mathbf{h}_\sigma(i)$ act upon

$$\left(\begin{array}{c|cccc} & \mathbf{e}_\uparrow(i) & \mathbf{e}_\downarrow(i) & \mathbf{h}_\uparrow(i) & \mathbf{h}_\downarrow(i) \\ \hline \mathbf{e}_\uparrow^T(i) & h_\uparrow & 0 & 0 & \Delta_{\uparrow\downarrow} \\ \mathbf{e}_\downarrow^T(i) & 0 & h_\downarrow & \Delta_{\downarrow\uparrow} & 0 \\ \mathbf{h}_\uparrow^T(i) & 0 & \Delta_{\downarrow\uparrow}^\dagger & -h_\uparrow^T & 0 \\ \mathbf{h}_\downarrow^T(i) & \Delta_{\uparrow\downarrow}^\dagger & 0 & 0 & -h_\downarrow^T \end{array} \right). \quad (4.2.41)$$

As a first thing, we notice terms $U_{\uparrow\downarrow}, U_{\downarrow\uparrow}$ in equation 4.2.38 are identically zero. Moreover, by choosing to work with \mathcal{H}_1 , we can summarize the self-consistency equations with

$$\Delta_{i\uparrow\downarrow} = -V \mathbf{e}_\uparrow^T(i) f(\mathcal{H}_1) \mathbf{h}_\downarrow(i) \quad (4.2.42)$$

$$U_{i,\uparrow\uparrow} = -V \mathbf{h}_\uparrow^T(i) f(-\mathcal{H}_1) \mathbf{h}_\downarrow(i) \quad (4.2.43)$$

$$U_{i,\downarrow\downarrow} = -V \mathbf{e}_\uparrow^T(i) f(\mathcal{H}_1) \mathbf{e}_\uparrow(i). \quad (4.2.44)$$

These equations are equivalent to the well-known BdG relations written as a function of the eigenvalues and eigenvectors, see [117] for an example. However, the formulation in Eqs. 4.2.42-4.2.44 is particularly useful to optimize the numerical solution of the model. In fact, Eqs. 4.2.42-4.2.44 do not require the calculation of the eigenvalues and eigenvectors, factor which dramatically reduces the computational time. To conclude this section, we report the formulas for the current density and for the free energy $\Omega(H, \rho_{MF})$. The current density, which is defined on the lattice links, from site j to site i results

$$J_{ij} = - \left\langle \frac{\partial H}{\partial A_{ij}} \right\rangle = 2q \text{Im} [\varepsilon_{ij} \mathbf{e}_\uparrow^T(j) f(\mathcal{H}_1) \mathbf{e}_\uparrow(i) + \varepsilon_{ij}^* \mathbf{h}_\downarrow^T(j) f(\mathcal{H}_1) \mathbf{h}_\downarrow(i)]. \quad (4.2.45)$$

The free energy reads

$$\begin{aligned} \Omega = & \sum_{ij} \varepsilon_{ij} \mathbf{e}_\uparrow^T(j) f(\mathcal{H}_1) \mathbf{e}_\uparrow(i) - \sum_i \left(\frac{|\Delta_{i\uparrow\downarrow}|^2}{V} + \frac{U_{i\uparrow\uparrow} U_{i\downarrow\downarrow}}{V} \right) \\ & + T \sum_i [\mathbf{e}_\uparrow^T(i) f(\mathcal{H}_1) \ln(\mathcal{H}_1) \mathbf{e}_\uparrow(i) + \mathbf{h}_\downarrow^T(i) f(\mathcal{H}_1) \ln(\mathcal{H}_1) \mathbf{h}_\downarrow(i)], \end{aligned} \quad (4.2.46)$$

which can be reformulated in the more compact form³:

$$\Omega = \sum_i \left[\frac{|\Delta_i|^2}{V} + \frac{U_{i\uparrow\uparrow}U_{i\downarrow\downarrow}}{V} + U_{i\downarrow\downarrow} \right] - \frac{1}{\beta} \text{Tr} \ln (e^{-\beta\mathcal{H}_1} + 1). \quad (4.2.47)$$

Magnetic self consistency equations

The hopping parameter used in our model, reported in Eq. 4.2.34 contains the vector potential through the Peierls phase substitution. At each self-consistent iteration, after computing the gap and the Hartree fields, we compute the current density. Then we utilize the current density, to compute a new vector potential. Using a gradient descent method we minimise the standard magnetic Hamiltonian

$$H_M = \int_S d^2x \left[\frac{1}{2} (\nabla \times \mathbf{A}')^2 - \mathbf{J} \cdot \mathbf{A}' \right], \quad (4.2.48)$$

where $\mathbf{A}' = \mathbf{A} - \mathbf{A}_0$ with $\nabla \times \mathbf{A} = \mathbf{B}$ and $\nabla \times \mathbf{A}_0 = \mathbf{B}_{\text{ext}}$. By taking the functional derivative with respect to \mathbf{A}' , one obtains Maxwell's equation

$$\nabla \times (\nabla \times \mathbf{A}') = \mathbf{J} \quad \text{with} \quad \oint_{\partial S} (\mathbf{B} - \mathbf{B}_{\text{ext}}) \times \delta \mathbf{A}' \cdot d\ell = 0. \quad (4.2.49)$$

Since the variation $\delta \mathbf{A}'$ is arbitrary, at each boundary point we have $\mathbf{B} = \mathbf{B}_{\text{ext}}$. Moreover, Eq. 4.2.49 maintains the gauge invariance. Then, given a certain current density and external magnetic field, we can use a gradient descent method to find \mathbf{A}' . By iterating

$$\mathbf{A}'_{n+1} = \mathbf{A}'_n - \gamma d\mathbf{A}', \quad (4.2.50)$$

where n indicates the iteration, $\gamma > 0$ is a constant coefficient and $d\mathbf{A}' = \delta H_M / \delta \mathbf{A}'$, we reach the vector potential configuration which minimizes Eq. 4.2.48. Since the Hamiltonian \mathcal{H}_1 , we consider, is defined on a two-dimensional square lattice, we need to discretize⁴ the magnetic Hamiltonian in Eq. 4.2.48 accordingly. The discretization we use on the lattice is shown in Fig. 4.1. While the gap and the Hartree fields are defined on the sites, labeled by (l, m) , the current density and the vector potential are defined on the links between sites. The magnetic field is defined on the plaquettes, and is related to the magnetic flux by $\Phi_{lm} = B_{lm}^z a^2$. Assuming unitary lattice length, i.e., $a = 1$, the discretized curl operation becomes

$$\nabla \times \mathbf{A} \rightarrow (A_{l+1,m}^y - A_{l,m}^y - A_{l,m+1}^x + A_{l,m}^x) = B_{lm}^z, \quad (4.2.51)$$

³Here we neglected the term $\text{Tr}(h_{\downarrow})$ since it is constant.

⁴The discretization effectively corresponds to a finite-difference discretization scheme.

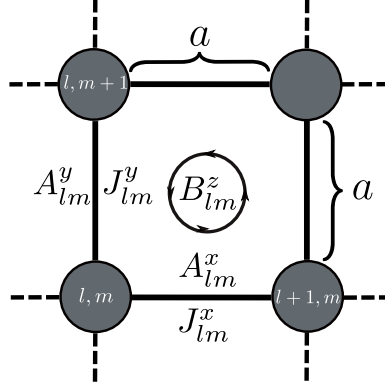


Figure 4.1: Illustration of a two dimensional lattice model. The vector potential A_{lm}^x, A_{lm}^y and the current density J_{lm}^x, J_{lm}^y are defined on the links connecting the sites, while the magnetic field B_{lm}^z is defined on the lattice plaquettes. Finally, the model is rescaled such that $a = 1$.

which leads to the discrete version of \mathbf{dA}'

$$\begin{aligned} dA_{l,m}^x &= -J_{l,m}^x \\ &+ \left(A_{l,m}^x - A_{l,m+1}^x + A_{l+1,m}^y - A_{l,m}^y - B_{\text{ext}}^z \right) \Theta_{l+1,m+1} \\ &- \left(A_{l,m-1}^x - A_{l,m}^x + A_{l+1,m-1}^y - A_{l,m-1}^y - B_{\text{ext}}^z \right) \Theta_{l+1,m-1} \end{aligned} \quad (4.2.52)$$

$$\begin{aligned} dA_{l,m}^y &= -J_{l,m}^y \\ &+ \left(A_{l,m}^y - A_{l-1,m}^y + A_{l-1,m}^x - A_{l-1,m+1}^x - B_{\text{ext}}^z \right) \Theta_{l-1,m+1} \\ &- \left(A_{l,m}^y - A_{l,m+1}^y + A_{l+1,m}^x - A_{l,m}^x - B_{\text{ext}}^z \right) \Theta_{l+1,m+1}. \end{aligned} \quad (4.2.53)$$

The function $\Theta_{l,m}$ takes care of the boundaries, i.e., if the site at the coordinates (l, m) does not exist, it goes to zero, otherwise its value is one. Using the discrete version of the curl defined in Eq. 4.2.51, we obtain

$$dA_{l,m}^x = -J_{l,m}^x + (B_{l,m}^z - B_{\text{ext}}^z) \Theta_{l+1,m+1} - (B_{l,m-1}^z - B_{\text{ext}}^z) \Theta_{l+1,m-1} \quad (4.2.54)$$

$$dA_{l,m}^y = -J_{l,m}^y - (B_{l,m}^z - B_{\text{ext}}^z) \Theta_{l+1,m+1} + (B_{l-1,m}^z - B_{\text{ext}}^z) \Theta_{l-1,m+1}. \quad (4.2.55)$$

Given the self consistent nature of the BdG model, it is not efficient to find the vector potential that minimizes the magnetic Hamiltonian at each iteration. Instead we follow the scheme:

1. Perform a self-consistent iteration computing the gap and Hartree term.
2. Compute the current densities J_{lm}^x and J_{lm}^y .

3. Compute $\mathbf{A}'_{lm}(n+1) = \mathbf{A}_{lm}(n) - \gamma \delta H_M / \delta \mathbf{A}'$.
4. Update the hopping parameters
5. Restart the procedure.

4.3 Multiband superconductivity

A consistent part of my research using Bogoliubov de Gennes Hamiltonians is carried out for multiband superconductors. Multiband superconductors are an extremely active field of research, which so far is generally modeled using macroscopic theories such as Ginzburg Landau, e.g., [5, 39, 84, 88, 98, 100]. In this section, we show how to obtain the mean field BdG model outlined above, for a multiband Hubbard model. In this case, we use a different approach based on the path integral formulation and the Hubbard-Stratonovich transformation.

Let us consider the C -band Hubbard Hamiltonian, defined on a two-dimensional lattice with N points as:

$$H = \sum_{ij\sigma\alpha} \psi_{i\sigma\alpha}^\dagger h_{ij\sigma\alpha} \psi_{j\sigma\alpha} - \sum_{i\alpha\beta} V_{\alpha\beta} \psi_{i\uparrow\alpha}^\dagger \psi_{i\downarrow\alpha}^\dagger \psi_{i\downarrow\beta} \psi_{i\uparrow\beta}, \quad (4.3.1)$$

with $h_{ij\sigma\alpha} = h_{ji\sigma\alpha}^*$ and $V_{\alpha\beta} = V_{\beta\alpha}^* \in \mathbb{R}$, while $\psi_{i\sigma\alpha}^\dagger, \psi_{i\sigma\alpha}$ are the fermionic fields. The index $i, j = 1, \dots, N$ label the position on the lattice, $\sigma = \uparrow, \downarrow$ labels the particle spin and $\alpha, \beta = 1, \dots, C$ indicates the superconducting component. In this model, Cooper pairs are allowed to tunnel from one band to the other, with tunneling probability proportional to the potential coefficient $V_{\alpha\beta}$, with $\alpha \neq \beta$, which we call *interband* coupling. The diagonal terms $V_{\alpha\alpha}$ are the pairing amplitudes within a band, or *intra-band* coupling. Moreover, we assume that the $C \times C$ matrix V is non singular, hence V^{-1} is well defined. The quantum mechanical action, in imaginary time, for Eq. 4.3.1 is

$$S = \int_0^{\frac{1}{T}} d\tau \left[\sum_{i\sigma\alpha} \psi_{i\sigma\alpha}^\dagger (\delta_{ij} \partial_\tau + h_{ij\sigma\alpha}) \psi_{j\sigma\alpha} - \sum_{i\alpha\beta} V_{\alpha\beta} \psi_{i\uparrow\alpha}^\dagger \psi_{i\downarrow\alpha}^\dagger \psi_{i\downarrow\beta} \psi_{i\uparrow\beta} \right], \quad (4.3.2)$$

and the partition function reads

$$Z = \int \mathcal{D}[\psi^\dagger \psi] e^{-S(\psi^\dagger \psi)}. \quad (4.3.3)$$

We can now introduce the Hubbard-Stratonovich identity⁵

$$\exp \left[\int d\tau \sum_{i\alpha\beta} V_{\alpha\beta} \rho_{i\alpha}^\dagger \rho_{i\beta} \right] = \int \mathcal{D}[\phi^\dagger \phi] \exp \left\{ - \int d\tau \sum_{i\alpha\beta} \left[(V^{-1})_{\alpha\beta} \phi_{i\alpha}^\dagger \phi_{i\beta} + \phi_{i\alpha}^\dagger \rho_{i\alpha} + \phi_{i\alpha} \rho_{i\alpha}^\dagger \right] \right\}, \quad (4.3.4)$$

where $\rho_{i\alpha} = \psi_{i\downarrow\alpha} \psi_{i\uparrow\alpha}$ and where we decoupled the four-interaction in the Cooper channel, as we are mainly interested in the superconducting effects. $\phi_{i\alpha}$ is the auxiliary bosonic field for the α -component, and V^{-1} the inverse of the potential matrix. The bosonic fields $\phi_{i\alpha}$ are equivalent to the variational parameters Δ_{ij} introduced in the previous section, therefore we expect them be determined through a self consistency equation and to play the role of the superconducting gaps. The partition function then becomes

$$Z = \int \mathcal{D}[\psi^\dagger \psi] \mathcal{D}[\phi^\dagger \phi] \exp \left\{ - \int d\tau \left[\sum_{ij\alpha} \Psi_{i\alpha}^\dagger (\delta_{ij} \partial_\tau + \mathcal{H}_{ij\alpha}) \Psi_{j\alpha} + \sum_{i\alpha\beta} (V^{-1})_{\alpha\beta} \phi_{i\alpha}^\dagger \phi_{i\beta} \right] \right\}, \quad (4.3.5)$$

where we introduced the Nambu spinors

$$\Psi_{i\alpha} = \begin{pmatrix} \psi_{i\uparrow\alpha} \\ \psi_{i\downarrow\alpha}^\dagger \end{pmatrix} \quad \Psi_{i\alpha}^\dagger = \begin{pmatrix} \psi_{i\uparrow\alpha}^\dagger & \psi_{i\downarrow\alpha} \end{pmatrix}, \quad (4.3.6)$$

and the matrix elements

$$\mathcal{H}_{ij\alpha} = \begin{pmatrix} h_{ij\uparrow\alpha} & \delta_{ij} \phi_{i\alpha} \\ \delta_{ji} \phi_{i\alpha}^* & -h_{ij\downarrow\alpha} \end{pmatrix}. \quad (4.3.7)$$

We are now ready to integrate out the fermionic degrees of freedom $\Psi_{i\alpha}, \Psi_{i\alpha}^\dagger$. In doing so, let us Fourier transform the Nambu spinors according to

$$\Psi_{i\alpha}(\tau) = \sum_{m=-\infty}^{\infty} \tilde{\Psi}_{i\alpha m} e^{i\omega_m \tau}, \quad \tilde{\Psi}_{i\alpha m} = \frac{1}{\beta} \int_0^\beta d\tau \Psi_{i\alpha}(\tau) e^{-i\omega_m \tau}, \quad (4.3.8)$$

where $\omega_m = 2\pi T(m + 1/2)$ are the fermionic Matsubara frequencies. After using the exponential properties to turn the sum over m in the exponent into an overall

⁵More details on Hubbard-Stratonovich transformations can be found in [69]

product, we solve the Gaussian integral

$$\begin{aligned} & \prod_{\alpha} \prod_m \int \mathcal{D}[\psi^\dagger \psi] \exp \left\{ - \sum_{ij} \tilde{\Psi}_{i\alpha m}^\dagger (\delta_{ij} i\omega_m + \mathcal{H}_{ij\alpha}) \tilde{\Psi}_{j\alpha m} \right\} \\ & = \prod_{\alpha} \prod_m \det(\mathbf{1}i\omega_m + \mathcal{H}_\alpha) = \exp \left\{ \sum_{\alpha} \sum_m \ln \det(\mathbf{1}i\omega_m + \mathcal{H}_\alpha) \right\}. \end{aligned} \quad (4.3.9)$$

By inserting it into the partition function of Eq. 4.3.5, we obtain

$$Z = \int \mathcal{D}[\phi^\dagger \phi] \exp \left\{ - \int d\tau \sum_{i\alpha\beta} (V^{-1})_{\alpha\beta} \phi_{i\alpha}^\dagger \phi_{i\beta} + \sum_{\alpha m} \ln \det(\mathbf{1}i\omega_m + \mathcal{H}_\alpha) \right\}. \quad (4.3.10)$$

At this point, we assume $\phi_{i\alpha}, \phi_{i\alpha}^\dagger$ are classical mean fields and therefore do not depend on the imaginary time τ , which means that we can integrate it out, namely

$$\int_0^{\frac{1}{T}} d\tau \sum_{i\alpha\beta} (V^{-1})_{\alpha\beta} \phi_{i\alpha}^\dagger \phi_{i\beta} \rightarrow \frac{1}{T} \sum_{i\alpha\beta} (V^{-1})_{\alpha\beta} \phi_{i\alpha}^\dagger \phi_{i\beta}, \quad (4.3.11)$$

obtaining the partition function

$$Z = \int \mathcal{D}[\phi^\dagger \phi] e^{-S'(\phi_\alpha^\dagger, \phi_\alpha)}, \quad (4.3.12)$$

with

$$S' = \frac{1}{T} \sum_{i\alpha\beta} (V^{-1})_{\alpha\beta} \phi_{i,\alpha}^* \phi_{i\beta} - \sum_{\alpha m} \ln \det(\mathbf{1}i\omega_m + \mathcal{H}_\alpha). \quad (4.3.13)$$

Moreover, we assume that the mean fields have no thermal fluctuations as well, which means we can consider only the minimal action configuration, allowing us to write the free energy as $F = TS'$. Before going further, let us develop the logarithmic term. Let us start by rewriting the Hamiltonian matrix as $\mathcal{H}_\alpha = U_\alpha^\dagger \mathcal{D}_\alpha U_\alpha$, where U is a unitary transformation ($\det U_\alpha = 1$). Then, we have

$$\sum_{\alpha m} \ln \det(\mathbf{1}i\omega_m + H_\alpha) = \sum_{\alpha m} \ln \det(\mathbf{1}i\omega_m + D_\alpha) \quad (4.3.14)$$

$$= \sum_{\alpha m} \ln \prod_{n=1}^{n=2N} (i\omega_m + \epsilon_{n\alpha}) \quad (4.3.15)$$

$$= \sum_{\alpha=1}^C \sum_{m=-\infty}^{\infty} \sum_{n=1}^{2N} \ln(i\omega_m + \epsilon_{n\alpha}), \quad (4.3.16)$$

where $\epsilon_{n\alpha}$ are the eigenvalues on the diagonal of D_α . Using the relation

$$\sum_{n=1}^{n=2N} \sum_{m=-\infty}^{m=\infty} \ln(i\omega_n + \epsilon_{m\alpha}) = - \sum_{n=1}^{n=2N} \ln f(\epsilon_{m\alpha}) = - \text{Tr} \ln f(\mathcal{H}_\alpha), \quad (4.3.17)$$

with $f(\epsilon) = (e^{\beta\epsilon} + 1)^{-1}$ the Fermi-Dirac distribution, we can re-write the free energy as

$$F = \sum_{i\alpha\beta} (V^{-1})_{\alpha\beta} \phi_{i\alpha}^* \phi_{i\beta} + T \sum_{\alpha} \text{Tr} \ln f(\mathcal{H}_{\alpha}). \quad (4.3.18)$$

To find the self consistency equations, we minimize the free energy with respect to the mean fields $\phi_{i\alpha}^*$. The detailed calculation is reported in the Appendix and the result reads:

$$\frac{\partial F}{\partial \phi_{i\alpha}^*} = \sum_{\beta} (V^{-1})_{\alpha\beta} \phi_{i\beta} + \mathbf{e}^T(i) f(\mathcal{H}_{\alpha}) \mathbf{h}(i) = 0. \quad (4.3.19)$$

By multiplying both terms by $V_{\gamma\alpha}$ and summing over α we obtain

$$\phi_{i\alpha} = - \sum_{\beta} V_{\alpha\beta} \mathbf{e}^T(i) f(\mathcal{H}_{\beta}) \mathbf{h}(i). \quad (4.3.20)$$

We can notice that, following the fermionic fields decoupling in the Cooper channel, the different bands in the model are described by decoupled Hamiltonians \mathcal{H}_{α} , one for each components. The interband interactions enter into play in the self consistency equations, where each gap is coupled to all the others by the coefficient of the potential matrix V .

To conclude this section, we provide an alternative way to write the free energy in 4.3.18, which is useful in the numerical computations. By rewriting

$$\begin{aligned} \text{Tr} \ln f(\mathcal{H}_{\alpha}) &= \text{Tr} \ln \left(\frac{e^{-\beta\mathcal{H}_{\alpha}}}{e^{-\beta\mathcal{H}_{\alpha}} + 1} \right) \\ &= - \text{Tr} \ln (e^{-\beta\mathcal{H}_{\alpha}} + 1) - \underbrace{\beta \text{Tr} \mathcal{H}_{\alpha}}_{\text{const}}, \end{aligned} \quad (4.3.21)$$

hence, up to a constant shift, the free energy reads

$$F = \sum_{i\alpha\beta} (V^{-1})_{\alpha\beta} \phi_{i\alpha}^* \phi_{i\beta} - T \text{Tr} \ln (e^{-\beta\mathcal{H}_{\alpha}} + 1). \quad (4.3.22)$$

4.4 Chebyshev polynomial expansion

One of the most significant limitations in the numerical calculation of Bogoliubov de Gennes Hamiltonians is the matrix diagonalization. In fact, the self-consistency equation is essentially a fixed-point iteration procedure, which, depending on the model's parameters, can require thousands of iterations. If we add that, on average, a $N \times N$ matrix diagonalization algorithm has a complexity of $\mathcal{O}(N^3)$, we can see how the time needed to solve the model rapidly increase. In fact, if we consider two dimensional system of with $N_x \times N_y$ sites, we need to numerically diagonalize a $(2N_x N_y) \times (2N_x N_y)$ BdG Hamiltonian, whose diagonalization time scales as $\mathcal{O}[(N_x N_y)^3]$. With some specific implementations it is possible to achieve some marginal improvement, but the simulation time remains extremely time sensitive and requires massive amounts of memory.

A particularly effective strategy to solve large-sized BdG models consists of not diagonalizing the Hamiltonian, and relies on the spectral decomposition method which utilizes Chebyshev polynomials [119–121]. In what follows, we outline the fundamentals of this method.

4.4.1 Chebyshev polynomials

The Chebyshev polynomials of the first kind are defined as

$$T_n(x) = \cos(n \arccos x), \quad (4.4.1)$$

where $x \in [-1, 1]$ and n is an integer number. Using de Moivre's identity $\cos n\theta + i \sin n\theta = (\cos \theta + i \sin \theta)^n$, one can write

$$T_n(x) = \cos(n \arccos x) = \operatorname{Re} \left\{ \left(x + i \sqrt{1 - x^2} \right)^n \right\}, \quad (4.4.2)$$

which allows a rapid calculation. Up to the forth order we have

$$\begin{aligned} T_0(x) &= 1 \\ T_1(x) &= x \\ T_2(x) &= 2x^2 - 1 \\ T_3(x) &= 4x^3 - 3x \\ T_4(x) &= 8x^4 - 8x^2 + 1, \end{aligned} \quad (4.4.3)$$

with the recursion relation

$$T_{n+1}(x) = 2xT_n(x) - T_{n-1}(x) \quad n \geq 1. \quad (4.4.4)$$

The Chebyshev polynomials are complete in the interval $[-1, 1]$ over the weight function $W(x) = 1/\sqrt{1 - x^2}$, i.e.,

$$\int_{-1}^1 dx \frac{W(x)}{w_n} T_m(x) T_n(x) = \delta_{mn}, \quad (4.4.5)$$

with $w_n = \frac{\pi}{2}$ if $n \neq 0$ and $w_n = \pi$ for $n = 0$. Each $T_n(x)$ is characterized by n zeros and $n + 1$ extrema, which all lie within $[-1, 1]$. Following the steps in [122], one can show that, given an arbitrary smooth function $f(x)$, the approximation formula

$$f(x) \simeq \sum_{k=1}^{N-1} c_k T_k(x) + \frac{1}{2} c_0 \quad (4.4.6)$$

$$c_j = \frac{2}{N} \sum_{k=1}^N f \left[\cos \left(\frac{\pi k - \frac{\pi}{2}}{N} \right) \right] \cos \left[\frac{\pi j (k - \frac{1}{2})}{N} \right] \quad (4.4.7)$$

holds, and is precise already at low values of the polynomial order N . In fact, the bound nature of the Chebyshev polynomial yields highly accurate approximations thanks to the error distribution over the domain. To clarify this further, let us consider the difference between Eq. 4.4.6 and the following formula

$$f(x) \simeq \sum_{k=1}^{m-1} c_k T_k + \frac{1}{2} c_0, \quad (4.4.8)$$

where $m \ll N$ and N yields a virtually perfect approximation. Since the Chebyshev polynomials are bound between $[-1, 1]$, the maximal value of the difference between Eq. 4.4.6 and Eq. 4.4.8, i.e., the approximation error, is given by

$$\varepsilon_{\max} = \sum_{j=m}^{N-1} c_j. \quad (4.4.9)$$

Since the c_j coefficients are rapidly decreasing as the order increases, the error is dominated by

$$\varepsilon_{\max} \sim c_m T_m(x), \quad (4.4.10)$$

which has $m + 1$ extrema and m zeros. Given the oscillatory nature of $T_m(x)$, the error ε_{\max} is distributed over the entire domain. It is this smooth spreading of the error, which enables the Chebyshev polynomials to be extremely close to the *minimax polynomial*, i.e., the approximating polynomial with the lowest possible error from the original function $f(x)$. Since the minimax polynomial computation is considerably challenging, the Chebyshev polynomials are a great tool to perform accurate spectral decompositions. Finally, it is possible to expand in Chebyshev polynomials functions with a domain exceeding $[-1, 1]$ by rescaling the domain of the function to expand.

4.4.2 BdG-Chebyshev decomposition

Here we explain how to utilize the Chebyshev polynomial expansion to improve the computational performance in solving BdG Hamiltonians. We show this for the single component case, but the extension to multicomponent superconductors is straightforward. Let us consider the gap self-consistency equation⁶ in Eq. 4.2.42

$$\Delta_{i\uparrow\downarrow} = -V\mathbf{e}_{\uparrow}^T(i)f(\mathcal{H})\mathbf{h}_{\downarrow}(i) = -V\mathbf{e}_{\uparrow}^T(i)Uf(\mathcal{D})U^{\dagger}\mathbf{h}_{\downarrow}(i). \quad (4.4.11)$$

Using the expansion in Eq. 4.4.6, we can write the term $Uf(\mathcal{D})U^{\dagger}$ as:

$$\begin{aligned} [Uf(\mathcal{D})U^{\dagger}]_{ij} &= \sum_n U_{in}f(\varepsilon_n)U_{nj}^{\dagger} \\ &\simeq U_{in} \left[\sum_{k=1}^{N-1} c_k T_k(\varepsilon_n) + \frac{1}{2}c_0 \right] U_{nj}^{\dagger} \\ &= \sum_{m=1}^{N-1} c_m [T_m(\mathcal{H})]_{ij} + \frac{1}{2}c_0\delta_{ij}, \end{aligned} \quad (4.4.12)$$

where c_m are given by 4.4.7, the function $f(x) = (e^{\beta x} + 1)^{-1}$ is the Fermi-Dirac distribution and the Hamiltonian \mathcal{H} is rescaled to ensure that all the eigenvalues are within $[-1, 1]$. The Chebyshev polynomials become

$$\begin{aligned} T_0(\mathcal{H}) &= \mathbf{1} \\ T_1(\mathcal{H}) &= \mathcal{H} \\ T_2(\mathcal{H}) &= 2\mathcal{H}^2 - \mathbf{1} \\ &\dots \end{aligned} \quad (4.4.13)$$

$$T_{n+1}(\mathcal{H}) = 2\mathcal{H}T_n(\mathcal{H}) - T_{n-1}(\mathcal{H}) \quad n \geq 1. \quad (4.4.14)$$

By substituting Eq. 4.4.12 in Eq. 4.4.11, and considering that $\mathbf{e}_{\uparrow}^T(i)\mathbf{h}_{\downarrow}(i) = 0$, we obtain

$$\Delta_{i\uparrow\downarrow} = -V\mathbf{e}_{\uparrow}^T(i) \sum_{m=1}^{N-1} c_m T_m(\mathcal{H})\mathbf{h}_{\downarrow}(i). \quad (4.4.15)$$

At this point, we can directly define $\mathbf{h}_{\downarrow m}(i) = T_m(\mathcal{H})\mathbf{h}_{\downarrow}(i)$, with the recursion relation $\mathbf{h}_{\downarrow m+1}(i) = 2\mathcal{H}\mathbf{h}_{\downarrow m}(i) - \mathbf{h}_{\downarrow m-1}(i)$, obtaining

$$\Delta_{i\uparrow\downarrow} = -V\mathbf{e}_{\uparrow}^T(i) \sum_{m=1}^{N-1} c_m \mathbf{h}_{\downarrow m}(i). \quad (4.4.16)$$

⁶We dropped the subscript 1 for the Hamiltonian matrix to simplify the notation.

Similarly, we can express the remaining self consistent relations as

$$U_{i,\uparrow\uparrow} = -V \mathbf{h}_{\downarrow}^T(i) f(-\mathcal{H}) \mathbf{h}_{\downarrow}(i) = V \left[\mathbf{h}_{\downarrow}^T(i) \sum_{m=1}^{N-1} c_m \mathbf{h}_{\downarrow m}(i) - \left(1 - \frac{c_0}{2}\right) \mathbb{1} \right] \quad (4.4.17)$$

$$U_{i,\downarrow\downarrow} = -V \mathbf{e}_{\uparrow}^T(i) f(\mathcal{H}) \mathbf{e}_{\uparrow}(i) = -V \left[\mathbf{e}_{\uparrow}^T(i) \sum_{m=1}^{N-1} c_m \mathbf{e}_{\uparrow m}(i) + \frac{1}{2} c_0 \mathbb{1} \right], \quad (4.4.18)$$

where $\mathbf{e}_{\uparrow m}(i)$ is defined in the same way as $\mathbf{h}_{\downarrow m}(i)$. Following a similar approach, we can compute the free energy reported in Eq. 4.3.22.

With this procedure, at each self consistent iteration, the number of matrix-vector multiplications that we need to perform, to compute all the $\mathbf{e}_{\uparrow m}, \mathbf{h}_{\downarrow m}$, scales with N_C , which indicates the chosen order for the Chebyshev expansion. Given the simple structure of \mathcal{H} each matrix-vector multiplication scales with the number of sites N . Then, we perform this procedure for every site, hence the time per iteration scales as $\mathcal{O}(N_C N^2)$. Considering a 2d system with $N = N_x N_y$ sites, the time per iteration follows $\mathcal{O}(N_C N_x^2 N_y^2)$. Moreover, by performing these calculations on graphical processing units (GPUs), up to the memory bandwidth saturation, the time per iteration is significantly reduced.

The choice of N_C is mostly influenced by the temperature of the system, i.e., the smoother the Fermi-Dirac distribution, the fewer Chebyshev polynomials are needed to approximate it accurately. In our simulations we generally use $N_C = 600$. For temperatures above $T > 0.01$, the error produced by the approximation is extremely small, and temperature independent, as shown in Fig. 4.2. However, if we decrease the temperature further, e.g., $T = 0.001$, we obtain Fig. 4.3. In this case, the error around $\varepsilon = 0$ is significantly higher, and we can notice non-negligible oscillations produced by the Chebyshev polynomials. These phenomena are called *Gibbs oscillations* and arise due to the Heaviside-like profile which the Fermi-Dirac distribution acquires at very low temperatures. To decrease them, one can substantially increase the number of polynomials, with a consequent loss in performances, or utilize filtering kernels in the computation of the coefficient c_j . A detailed analysis of the most effective kernels can be found in [121]. In this thesis, we employed the Chebyshev polynomial method only to simulate physical systems sufficiently far from the zero temperature limit, hence where Gibbs oscillations did not pose a threat.

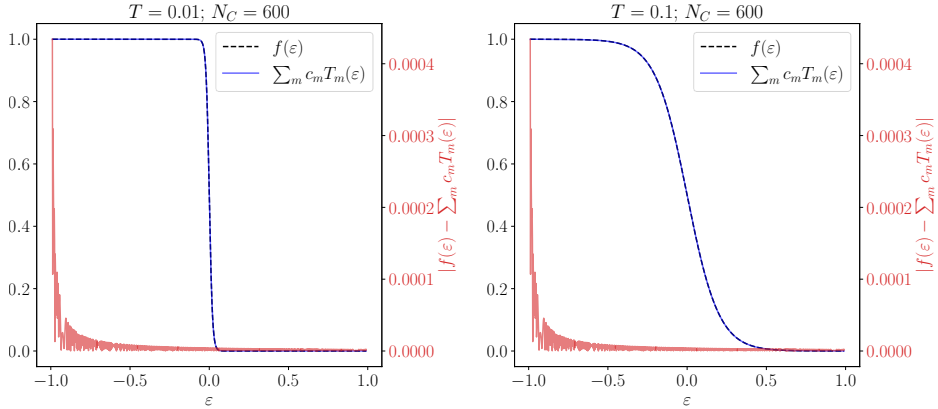


Figure 4.2: Fermi-Dirac distribution (dashed black line) and its approximation by Chebyshev polynomial expansion (blue line) as a function of the energy ε . The absolute value of the error produced by the approximation is plotted in red. Both panels are obtained with $N_C = 600$, the left panel with $T = 0.01$, while the right one with $T = 0.1$. On the x axis we have the energies of the system ε .

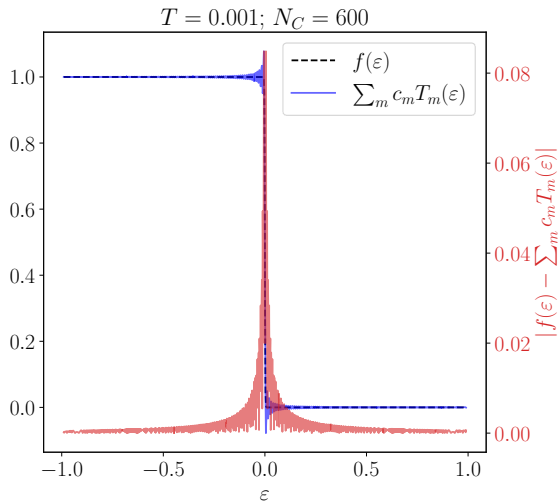


Figure 4.3: Fermi-Dirac distribution (dashed black line) and its approximation by Chebyshev polynomial expansion (blue line) as a function of the energy ε . The absolute value of the error produced by the approximation is plotted in red. This plot is obtained for $T = 0.001$, and we can notice the presence of Gibbs oscillation in the vicinity of $\varepsilon = 0$.

4.5 Research activity

Paper 4

As we presented in Chapter 2, most of the superconductors of current interest are multiband [1, 2], and present a wide range of interband couplings, from weak interactions to very strong ones. Moreover, as demonstrated in [37, 38], the boundary conditions introduced by Cairoli, de Gennes and Matricon [35, 36, 123] are not correct, as they do not take into account the presence of surface, or more generally, boundary states. As shown in [9, 12, 37], surface states are associated with an higher critical temperature than bulk states. Hence, microscopically understanding how the boundary effects influence the high temperature regimes in multiband superconductor is of crucial importance today. In fact, the behavior of the gaps near the boundaries plays an important role in small superconducting devices, such as nanowires or single photon detectors [124]. Moreover, multiband superconductors are candidate materials to realize superconducting qubits [125], which constitutes a significant motivation to deepen the understanding of their boundary physics. The experimental work in [82, 126] suggest that ZrB_{12} is multiband with weak interband coupling, and [127–129] claim that its superconducting gap present a significantly different structure near the boundaries than in the bulk. Moreover, these effects appear to be stronger than in other multiband superconductors [130–135]. A potential explanation for these phenomena proposes a different type of electron-phonon interaction near the sample’s boundaries [136]. However, in light of the existence of surface states [12, 37], we provide an alternative candidate explanation using a microscopic tight-binding BdG Hamiltonian to describe a two band superconductor with weak interband coupling. We find that, surface states are present and we demonstrate that the relative difference between the bulk critical temperature and the surface critical temperature is a non trivial function of the interband coupling. When the interband coupling is weak, we find that spatial variation of the two superconducting gaps occurs with multiple characteristic length scales. We analyze this behavior for one-dimensional superconductors, and show its existence in two-dimensional systems as well.

Paper 5

In this work, we study the properties of time reversal symmetry breaking states from a microscopic perspective. Recent experiments claimed to find $s + is$ states occurring in Fe-based multiband superconductors such as $\text{Ba}_{1-x}\text{K}_x\text{Fe}_2\text{As}_2$ [1, 2, 33]. The $s + is$ state [84, 89, 91, 94] is a spin-singlet superconducting state, which brakes time reversal symmetry, yielding a ground state that breaks $U(1) \times Z_2$. The experimental signatures of time reversal symmetry breaking states can be associated with the presence of spontaneous magnetic fields, which can be observed through muon spin rotation experiments [84, 89, 94, 137]. Previous theoretical works, done within the macroscopic Ginzburg Landau model [6, 88, 93, 95, 96, 98, 99] associated spontaneous magnetic fields in the vicinity of certain types of defects, such as domain walls and

lattice impurities. While superconducting states breaking time reversal symmetry have been studied for decades, the recent works on surface states [9, 12, 37, 38] clarified that standard quasi-classical theoretical approaches neglect important boundary physics. A microscopic study of superconducting models breaking time reversal symmetry is therefore needed. In this work, we consider a microscopic tight-binding BdG Hamiltonian describing a three component s -wave superconductor, exhibiting phase frustration, i.e., $s + is$ states. Within the current classification schemes, an $s + is$ state is not chiral and does not exhibit topological surface states, and therefore no superconducting currents are expected to arise spontaneously. We employ a two dimensional Bogoliubov de Gennes numerical solver, which computes superconducting gaps and magnetic field self consistently. We show the presence of a non-spatially-uniform $s + is$ state, which yield spontaneous superconducting currents and magnetic signatures. In these states, the order parameter breaks time reversal symmetry only in the vicinity of the corners, while the bulk transitions to an s_{++} state, i.e., zero phase difference between the three bands. Then, we study the structure of the spontaneous magnetic field generated by these states, and how it changes as a function of the temperature. Moreover, we show that it is possible to enhance the spontaneous magnetic field by acting on the geometry of the sample. Finally, we emphasize that these states are not a generic property of superconductors breaking time reversal symmetry, due to the sensitivity of the magnetic field intensity to the model parameters. What we show, is the theoretical existence of spontaneous-current-carrying boundary states in $s + is$ superconductors. As of now, such states were thought to exist only in materials with chiral superconductivity, such as $p + ip$ [70, 138–140].

Paper 6

In this work we study the skyrmion topological excitations occurring in three band superconductors breaking time reversal symmetry, modeled using a fully microscopic tight binding BdG Hamiltonian. Skyrmions are topological excitations, which were initially utilized as an effective description of nucleons [141]. Recently, the interest on skyrmions occurring in condensed matter systems with a high degree of symmetry breaking increased [4, 5, 142–147]. It was shown that $\mathbb{C}P^{N-1}$ are, generally, metastable in N -components superconducting models where the presence of potential terms breaks the $U(1)^N$ symmetry down to a $U(1) \times Z_2$ discrete symmetry [4]. In this work, we study a three component $s + is$ superconducting system where a Josephson interaction breaks the $U(1)^N$ symmetry down to $U(1) \times Z_2$. The Ginzburg-Landau based study of such systems [4, 5] suggests the metastable formation of $\mathbb{C}P^2$ skyrmions, with a slightly higher energy per flux quanta compared to the one of composite vortices. However, the recent experimental discovery of $s + is$ superconductivity in $\text{Ba}_{1-x}\text{K}_x\text{Fe}_2\text{As}_2$ [1, 2, 33] motivates the investigation of the existence of skyrmion solutions in fully microscopic models. In fact, the Ginzburg-Landau model, is quantitatively valid near the superconducting critical temperature and retains only coarse-grained degrees of freedom. In this work, we

model the $s+is$ three band superconductor using a tight binding BdG Hamiltonian, with self-consistent superconducting gaps and magnetic field. In this way, we are able to study the stability of the skyrmionic solutions, determine their magnetic field and local density of states.

Paper 7

In this work we study boundary effects in Fulde-Ferrell-Larkin-Ovchinnikov (FFLO) superconductors. We provide both a macroscopic description, by employing the Ginzburg Landau formalism and a microscopic description using a tight binding BdG Hamiltonian with Zeeman splitting. We begin by presenting a sequence of phase transitions in a three dimensional Ginzburg Landau model for an FFLO superconductor. Then, we perform the same type of simulations for within the Bogoliubov de Gennes formalism, limited to two-dimensional samples. We show that when the temperature exceeds the bulk critical temperature the superconducting state remains localized along the edges and corners of the sample. As the temperature is increased further, the order parameter remains non-zero only in the vicinity of the corners. We therefore define, on top of the bulk critical temperature, an edge critical temperature and a corner critical temperature.

Paper 8

In this paper we consider an interface between a superconductor, described with a tight-binding mean field Hamiltonian and a non-superconducting band insulator. We limit this study to a simple one-dimensional lattice model, and show that within certain parameter ranges, it is possible to have an enhancement of the critical temperature in the vicinity of the interface, without increasing the strength of the superconducting-pairing interaction. Finally, we present in which regimes, the critical temperature near the surface exceeds the critical temperature of a standard superconductor-vacuum interface.

Chapter 5

Conclusion

The physical systems and models we presented in the Chapter 2-4 lay the ground for the research activity I carried out throughout my PhD. Most of the physical problems of current interest in superconductivity require non-linear descriptions. In most cases, they are not amenable to analytical treatments, and represent complicated cases for numerical approaches. This creates the need to develop new and advanced numerical approaches, to investigate the phenomenology of systems that cannot be treated by other means. The study of inhomogeneous solutions in large-sized systems entails numerous difficulties, since is not only computationally intensive but also memory heavy, which often make conventional CPUs insufficient, and, in practise, require the acceleration provided by Graphic Processing Units (GPUs). The majority of the numerical algorithms I developed during my PhD are GPU-based, and provide a reliable approach to study inhomogeneous solutions in fully non-linear models. This allows us to answer open questions in the field of superconductivity, which are of great current interest. We summarize them in the following:

1. How can we determine the free energy barriers to vortex nucleation in single band and multiband superconductors without relying on uncontrolled approximations?
2. What are the properties of time reversal symmetry breaking superconducting states from a microscopic and macroscopic perspective?
3. Do microscopic models for time reversal symmetry breaking superconductors allow skyrmion solutions? What is their structure and dependence on the model parameters?
4. Can boundary states in a superconductor have higher critical temperature than bulk states?

In Part II, the results I obtained are presented in the form of eight papers.

Chapter 6

Appendix

6.1 Details on Eq. 4.3.19

Here we provide the details for the calculation of Eq. 4.3.19. The first term is

$$\partial_{\phi_{i\alpha}^*} \sum_{j\gamma\beta} (V^{-1})_{\gamma\beta} \phi_{j\gamma}^* \phi_{j\beta} = (V^{-1})_{\alpha\beta} \phi_{i\beta}. \quad (6.1.1)$$

Let us now focus on the derivation of $\mathbf{e}^T(i) f(H_\alpha) \mathbf{h}(i)$. For the sake of notation, let us drop the band index, keeping in mind that the calculations and quantities that follow are relative to the superconducting band α . Let us start by considering

$$\begin{aligned} \partial_{\phi_i^*} \text{Tr} \ln f(\mathcal{H}) &= \sum_n \partial_{\phi_i^*} \ln(f(\epsilon_n)) \\ &= \sum_n \frac{1}{f(\epsilon_n)} \frac{\partial f}{\partial \epsilon_n} \frac{\partial \epsilon_n}{\partial \phi_i^*} \\ &= \{f'(x) = -\beta f(x) f(-x) \quad \text{and} \quad \epsilon_n = \mathcal{D}_{nn}\} \\ &= -\beta \sum_n f(-\mathcal{D})_{nn} \frac{\partial \mathcal{D}_{nn}}{\partial \phi_i^*}, \end{aligned}$$

with $\beta = 1/T$. Using the relations

$$\mathcal{H} = U \mathcal{D} U^\dagger \quad \text{and} \quad f(\mathcal{H}) = U f(\mathcal{D}) U^\dagger, \quad (6.1.2)$$

together with the Einstein summation on repeated indices, we have

$$\begin{aligned}
-\frac{1}{\beta} \partial_{\phi_i^*} \text{Tr} \ln f(\mathcal{H}) &= f(-\mathcal{D})_{nm} \delta_{mp} \frac{\partial \mathcal{D}_{pq}}{\partial \phi_i^*} \delta_{qn} \\
&= \left\{ U_{ml}^\dagger U_{lp} = \delta_{mp} \right\} \\
&= f(-\mathcal{D})_{nm} U_{ml}^\dagger U_{lp} \frac{\partial \mathcal{D}_{pq}}{\partial \phi_i^*} U_{qs}^\dagger U_{sn} \\
&= \left(U_{sn} f(-\mathcal{D})_{nm} U_{ml}^\dagger \right) \left(U_{lp} \frac{\partial \mathcal{D}_{pq}}{\partial \phi_i^*} U_{qs}^\dagger \right) \\
&= \left\{ \partial_{\phi_i^*} (UU^\dagger) = 0 \quad \text{and} \quad U_{lp} \mathcal{D}_{pq} U_{qs}^\dagger = \mathcal{H}_{ls} \right\} \\
&= \left\{ U_{lp} \frac{\partial \mathcal{D}_{pq}}{\partial \phi_i^*} U_{qs}^\dagger = \frac{\partial (U_{lp} \mathcal{D}_{pq} U_{qs}^\dagger)}{\partial \phi_i^*} \right\} \\
&= f(-\mathcal{H})_{sl} \frac{\partial \mathcal{H}_{ls}}{\partial \phi_i^*}.
\end{aligned}$$

Given the following structure for \mathcal{H}

$$\mathcal{H} = \left(\begin{array}{ccc|ccc} & & & \phi_1 & & \\ & (h)_{ij} & & & \ddots & \\ & & & & & \phi_N \\ \hline \phi_1^* & & & & & \\ & \ddots & & & & \\ & & & \phi_N^* & & \\ & & & & -(h)_{ji} & \end{array} \right) \Rightarrow \frac{\partial \mathcal{H}_{ls}}{\partial \phi_i^*} = \delta_{li} \delta_{s, i+N}.$$

Hence, we have that:

$$-\frac{1}{\beta} \partial_{\phi_i^*} \text{Tr} \ln f(\mathcal{H}) = \sum_{sl} f(-\mathcal{H})_{sl} \frac{\partial \mathcal{H}_{ls}}{\partial \phi_i^*} \quad (6.1.3)$$

$$= (\mathbf{1} - f(\mathcal{H}))_{sl} \delta_{si} \delta_{l, i+N} \quad (6.1.4)$$

$$= -\delta_{is} f(\mathcal{H})_{sl} \delta_{l, i+N}. \quad (6.1.5)$$

Introducing the notation $[\mathbf{e}(i)]_l = \delta_{il}$ and $[\mathbf{h}(i)]_s = \delta_{s, i+N}$ we obtain:

$$\partial_{\phi_i^*} \text{Tr} \ln f(\mathcal{H}) = \beta \mathbf{e}(i)^T f(\mathcal{H}) \mathbf{h}(i), \quad (6.1.6)$$

which gives Eq. 4.3.19.

Bibliography

- [1] V. Grinenko *et al.*, *Superconductivity with broken time-reversal symmetry in ion-irradiated $Ba_{0.27}K_{0.73}Fe_2As_2$ single crystals*, Phys. Rev. B **95**, 214511 (2017).
- [2] V. Grinenko *et al.*, *Superconductivity with broken time-reversal symmetry inside a superconducting s -wave state*, Nature Physics **16**, 789 (2020).
- [3] E. Weinan, W. Ren and E. Vanden-Eijnden, *Simplified and improved string method for computing the minimum energy paths in barrier-crossing events*, Journal of Chemical Physics **126**, 164103 (2007).
- [4] J. Garaud, J. Carlström and E. Babaev, *Topological solitons in three-band superconductors with broken time reversal symmetry*, Phys. Rev. Lett. **107**, 197001 (2011).
- [5] J. Garaud *et al.*, *Chiral CP^2 skyrmions in three-band superconductors*, Phys. Rev. B **87**, 014507 (2013).
- [6] A. Benfenati *et al.*, *Magnetic signatures of domain walls in $s + is$ and $s + id$ superconductors: Observability and what that can tell us about the superconducting order parameter*, Phys. Rev. B **101**, 054507 (2020).
- [7] A. Benfenati *et al.*, *Vortex nucleation barrier in superconductors beyond the Bean-Livingston approximation: A numerical approach for the sphaleron problem in a gauge theory*, Phys. Rev. B **101**, 220505 (2020).
- [8] A. Maiani, A. Benfenati and E. Babaev, *Vortex nucleation barriers and stable fractional vortices near boundaries in multicomponent superconductors*, arXiv preprint arXiv:2111.01061 (2021).
- [9] A. Benfenati, A. Samoilenka and E. Babaev, *Boundary effects in two-band superconductors*, Phys. Rev. B **103**, 144512 (2021).
- [10] A. Benfenati and E. Babaev, *Spontaneous edge and corner currents in $s + is$ superconductors and time reversal symmetry breaking surface states*, Phys. Rev. B **105**, 134518 (2022).

- [11] A. Benfenati, M. Barkman and E. Babaev, *Demonstration of $\mathbb{C}P^2$ skyrmions in three-band superconductors by self-consistent solutions to a Bogoliubov-de-Gennes model*, arXiv preprint arXiv:2204.05242 (2022).
- [12] A. Samoilenka *et al.*, *Pair-density-wave superconductivity of faces, edges, and vertices in systems with imbalanced fermions*, Phys. Rev. B **101**, 054506 (2020).
- [13] M. Barkman *et al.*, *Elevated critical temperature at BCS superconductor-band insulator interfaces*, arXiv preprint arXiv:2201.11614 (2022).
- [14] H. Kamerlingh Onnes, *The resistance of pure mercury at helium temperatures*, Commun. Phys. Lab. Univ. Leiden, b **120** (1911).
- [15] W. Meissner and R. Ochsenfeld, *Ein neuer effekt bei eintritt der supraleitfähigkeit*, Naturwissenschaften **21**, 787 (1933).
- [16] M. Tinkham, *Introduction to superconductivity* (Courier Corporation, 2004).
- [17] F. London and H. London, *The electromagnetic equations of the supraconductor*, Proceedings of the Royal Society of London. Series A-Mathematical and Physical Sciences **149**, 71 (1935).
- [18] E. Maxwell, *Isotope effect in the superconductivity of mercury*, Phys. Rev. **78**, 477 (1950).
- [19] C. Reynolds *et al.*, *Superconductivity of isotopes of mercury*, Phys. Rev. **78**, 487 (1950).
- [20] V. L. Ginzburg and L. D. Landau, *To the theory of superconductivity*, Zh. Eksp. Teor. Fiz. **20** (1950).
- [21] J. Bardeen, L. N. Cooper and J. R. Schrieffer, *Theory of superconductivity*, Phys. Rev. **108**, 1175 (1957).
- [22] L. P. Gor'kov, *Microscopic derivation of the Ginzburg-Landau equations in the theory of superconductivity*, Sov. Phys. JETP **9**, 1364 (1959).
- [23] H. Suhl, B. Matthias and L. Walker, *Bardeen-Cooper-Schrieffer theory of superconductivity in the case of overlapping bands*, Phys. Rev. Lett. **3**, 552 (1959).
- [24] V. Moskalenko, *Superconductivity in metals with overlapping energy bands*, Fiz. Metal. Metalloved **8**, 2518 (1959).
- [25] J. Nagamatsu *et al.*, *Superconductivity at 39 K in magnesium diboride*, nature **410**, 63 (2001).

- [26] A. Y. Liu, I. Mazin and J. Kortus, *Beyond Eliashberg superconductivity in MgB_2 : anharmonicity, two-phonon scattering, and multiple gaps*, Phys. Rev. Lett. **87**, 087005 (2001).
- [27] S. Souma *et al.*, *The origin of multiple superconducting gaps in MgB_2* , Nature **423**, 65 (2003).
- [28] T. Yildirim *et al.*, *Giant anharmonicity and nonlinear electron-phonon coupling in MgB_2 : a combined first-principles calculation and neutron scattering study*, Phys. Rev. Lett. **87**, 037001 (2001).
- [29] Y. Kamihara *et al.*, *Iron-based layered superconductor $La[O_{1-x}F_x]FeAs$ ($x = 0.05 - 0.12$) with $T_c = 26K$* , Journal of the American Chemical Society **130**, 3296 (2008).
- [30] P. Hirschfeld, M. Korshunov and I. Mazin, *Gap symmetry and structure of Fe-based superconductors*, Reports on Progress in Physics **74**, 124508 (2011).
- [31] P. C. Chu *et al.*, *Superconductivity in iron-pnictides*, Physica. C. Superconductivity **469** (2009).
- [32] A. Kreisel, P. J. Hirschfeld and B. M. Andersen, *On the remarkable superconductivity of FeSe and its close cousins*, Symmetry **12**, 1402 (2020).
- [33] V. Grinenko *et al.*, *Quartic metal: Spontaneous breaking of time-reversal symmetry due to four-fermion correlations in $Ba_{1-x}K_xFe_2As_2$* , Nature Physics **17**, 1254–1259 (2021).
- [34] L. Schubnikow *et al.*, *Magnetische Eigenschaften supraleitender Metalle und Legierungen*, Phys. Z. Sowiet **10**, 165 (1936).
- [35] P. de Gennes, *Boundary effects in superconductors*, Rev. Mod. Phys. **36**, 225 (1964).
- [36] C. Caroli, P. G. de Gennes and J. Matricon, *Sur certaines propriétés des alliages supraconducteurs non magnétiques*, J. phys. radium **23**, 707 (1962).
- [37] A. Samoilenka and E. Babaev, *Boundary states with elevated critical temperatures in Bardeen-Cooper-Schrieffer superconductors*, Phys. Rev. B **101**, 134512 (2020).
- [38] A. Samoilenka and E. Babaev, *Microscopic derivation of superconductor-insulator boundary conditions for Ginzburg-Landau theory revisited: Enhanced superconductivity at boundaries with and without magnetic field*, Phys. Rev. B **103**, 224516 (2021).
- [39] B. Svistunov, E. Babaev and N. Prokof'ev, *Superfluid States of Matter* (Taylor & Francis, 2015).

- [40] V. V. Schmidt *et al.*, *The physics of superconductors: Introduction to fundamentals and applications* (Springer Science & Business Media, 1997).
- [41] C. Bean and J. Livingston, *Surface barrier in type-II superconductors*, Phys. Rev. Lett. **12**, 14 (1964).
- [42] P. De Gennes, *Vortex nucleation in type II superconductors*, Solid State Communications **3**, 127 (1965).
- [43] L. Kramer, *Stability limits of the meissner state and the mechanism of spontaneous vortex nucleation in superconductors*, Phys. Rev. **170**, 475 (1968).
- [44] L. Kramer, *Breakdown of the superheated meissner state and spontaneous vortex nucleation in type ii superconductors*, Zeitschrift für Physik A Hadrons and nuclei **259**, 333 (1973).
- [45] H. Fink and A. Presson, *Stability limit of the superheated Meissner state due to three-dimensional fluctuations of the order parameter and vector potential*, Phys. Rev. **182**, 498 (1969).
- [46] P. V. Christiansen, *Magnetic superheating of high- κ superconductors*, Solid State Communications **7**, 727 (1969).
- [47] A. J. Dolgert, S. J. Di Bartolo and A. T. Dorsey, *Superheating fields of superconductors: Asymptotic analysis and numerical results*, Phys. Rev. B **53**, 5650 (1996).
- [48] G. Catelani and J. P. Sethna, *Temperature dependence of the superheating field for superconductors in the high- κ London limit*, Phys. Rev. B **78**, 224509 (2008).
- [49] M. K. Transtrum, G. Catelani and J. P. Sethna, *Superheating field of superconductors within Ginzburg-Landau theory*, Phys. Rev. B **83**, 094505 (2011).
- [50] C. Bolech, G. C. Buscaglia and A. Lopez, *Numerical simulation of vortex arrays in thin superconducting films*, Phys. Rev. B **52**, R15719 (1995).
- [51] S. Kim *et al.*, *Effects of sample geometry on the dynamics and configurations of vortices in mesoscopic superconductors*, Phys. Rev. B **76**, 024509 (2007).
- [52] A. R. Pack *et al.*, *Vortex nucleation in superconductors within time-dependent Ginzburg-Landau theory in two and three dimensions: role of surface defects and material inhomogeneities*, Phys. Rev. B **101**, 144504 (2020).
- [53] V. Rubakov, *Classical theory of gauge fields* (Princeton University Press, 2009).
- [54] N. Manton and P. Sutcliffe, *Topological solitons* (Cambridge University Press, 2004).

- [55] H. Năstase, *Classical field theory* (Cambridge University Press, 2019).
- [56] E. W. Kolb and M. S. Turner, *The early universe* (CRC press, 2018).
- [57] M. Shifman, *Advanced topics in quantum field theory: A lecture course* (Cambridge University Press, 2012).
- [58] C. M. Natarajan, M. G. Tanner and R. H. Hadfield, *Superconducting nanowire single-photon detectors: physics and applications*, *Superconductor science and technology* **25**, 063001 (2012).
- [59] I. Esmaeil Zadeh *et al.*, *Single-photon detectors combining high efficiency, high detection rates, and ultra-high timing resolution*, *Apl Photonics* **2**, 111301 (2017).
- [60] A. Y. Kitaev, *Unpaired Majorana fermions in quantum wires*, *Physics-uspekhi* **44**, 131 (2001).
- [61] C. Nayak *et al.*, *Non-Abelian anyons and topological quantum computation*, *Reviews of Modern Physics* **80**, 1083 (2008).
- [62] J. D. Bommer *et al.*, *Spin-orbit protection of induced superconductivity in Majorana nanowires*, *Phys. Rev. Lett.* **122**, 187702 (2019).
- [63] R. M. Lutchyn, J. D. Sau and S. D. Sarma, *Majorana fermions and a topological phase transition in semiconductor-superconductor heterostructures*, *Phys. Rev. Lett.* **105**, 077001 (2010).
- [64] S. Vaitiekėnas *et al.*, *Flux-induced topological superconductivity in full-shell nanowires*, *Science* **367**, eaav3392 (2020).
- [65] A. Maiani, *Minimum Free Energy Paths of Vortices Nucleation in Superconductors*, PhD thesis, 2019.
- [66] D. Tilley, *The Ginzburg-Landau equations for pure two band superconductors*, *Proceedings of the Physical Society (1958-1967)* **84**, 573 (1964).
- [67] M. Silaev and E. Babaev, *Microscopic derivation of two-component Ginzburg-Landau model and conditions of its applicability in two-band systems*, *Phys. Rev. B* **85**, 134514 (2012).
- [68] A. Gurevich, *Limits of the upper critical field in dirty two-gap superconductors*, *Physica C: Superconductivity* **456**, 160 (2007).
- [69] A. Altland and B. D. Simons, *Condensed matter field theory* (Cambridge university press, 2010).
- [70] M. Sigrist and K. Ueda, *Phenomenological theory of unconventional superconductivity*, *Reviews of Modern physics* **63**, 239 (1991).

- [71] P. W. Anderson and J. M. Rowell, *Probable observation of the Josephson superconducting tunneling effect*, Phys. Rev. Lett. **10**, 230 (1963).
- [72] B. D. Josephson, *Possible new effects in superconductive tunnelling*, Physics Lett. **1**, 251 (1962).
- [73] P. Jones, *Type I and two-gap superconductivity in neutron star magnetism*, Monthly Notices of the Royal Astronomical Society **371**, 1327 (2006).
- [74] E. Babaev, A. Sudbø and N. Ashcroft, *A superconductor to superfluid phase transition in liquid metallic hydrogen*, Nature **431**, 666 (2004).
- [75] E. Babaev, *Vortices with fractional flux in two-gap superconductors and in extended Faddeev model*, Phys. Rev. Lett. **89**, 067001 (2002).
- [76] M. Silaev, *Stable fractional flux vortices and unconventional magnetic state in two-component superconductors*, Phys. Rev. B **83**, 144519 (2011).
- [77] D. F. Agterberg, E. Babaev and J. Garaud, *Microscopic prediction of skyrmion lattice state in clean interface superconductors*, Phys. Rev. B **90**, 064509 (2014).
- [78] E. Babaev and M. Speight, *Semi-Meissner state and neither type-I nor type-II superconductivity in multicomponent superconductors*, Phys. Rev. B **72**, 180502 (2005).
- [79] E. Babaev, *Neither a type-I nor a type-II superconductivity in a two-gap system*, arXiv preprint cond-mat/0302218 (2003).
- [80] V. Moshchalkov *et al.*, *Type-1.5 Superconductivity*, Phys. Rev. Lett. **102**, 117001 (2009).
- [81] S. Ray *et al.*, *Muon-spin rotation measurements of the vortex state in Sr₂RuO₄: Type-1.5 superconductivity, vortex clustering, and a crossover from a triangular to a square vortex lattice*, Phys. Rev. B **89**, 094504 (2014).
- [82] P. Biswas *et al.*, *Coexistence of type-I and type-II superconductivity signatures in ZrB₁₂ probed by muon spin rotation measurements*, Phys. Rev. B **102**, 144523 (2020).
- [83] N. Bolotina *et al.*, *Checkerboard patterns of charge stripes in the two-gap superconductor ZrB₁₂*, Phys. Rev. B **105**, 054511 (2022).
- [84] J. Carlström, J. Garaud and E. Babaev, *Length scales, collective modes, and type-1.5 regimes in three-band superconductors*, Phys. Rev. B **84**, 134518 (2011).
- [85] J. Carlström, E. Babaev and M. Speight, *Type-1.5 superconductivity in multi-band systems: Effects of interband couplings*, Phys. Rev. B **83**, 174509 (2011).

- [86] E. Babaev, J. Carlström and M. Speight, *Type-1.5 superconducting state from an intrinsic proximity effect in two-band superconductors*, Phys. Rev. Lett. **105**, 067003 (2010).
- [87] M. Silaev and E. Babaev, *Microscopic theory of type-1.5 superconductivity in multiband systems*, Phys. Rev. B **84**, 094515 (2011).
- [88] J. Garaud and E. Babaev, *Domain Walls and Their Experimental Signatures in $s + is$ Superconductors*, Phys. Rev. Lett. **112**, 017003 (2014).
- [89] V. Stanev and Z. Tešanović, *Three-band superconductivity and the order parameter that breaks time-reversal symmetry*, Phys. Rev. B **81**, 134522 (2010).
- [90] W. C. Lee, S. C. Zhang and C. Wu, *Pairing state with a time-reversal symmetry breaking in FeAs-based superconductors*, Phys. Rev. Lett. **102**, 217002 (2009).
- [91] J. Böker *et al.*, *$s + is$ superconductivity with incipient bands: Doping dependence and STM signatures*, Phys. Rev. B **96**, 014517 (2017).
- [92] C. Platt *et al.*, *Mechanism for a pairing state with time-reversal symmetry breaking in iron-based superconductors*, Phys. Rev. B **85**, 180502 (2012).
- [93] V. Vadimov and M. Silaev, *Polarization of the spontaneous magnetic field and magnetic fluctuations in $s + is$ anisotropic multiband superconductors*, Phys. Rev. B **98**, 104504 (2018).
- [94] S. Maiti and A. V. Chubukov, *$s + is$ state with broken time-reversal symmetry in Fe-based superconductors*, Phys. Rev. B **87**, 144511 (2013).
- [95] S. Maiti, M. Sigrist and A. Chubukov, *Spontaneous currents in a superconductor with $s + is$ symmetry*, Phys. Rev. B **91**, 161102 (2015).
- [96] S. Z. Lin, S. Maiti and A. Chubukov, *Distinguishing between $s + id$ and $s + is$ pairing symmetries in multiband superconductors through spontaneous magnetization pattern induced by a defect*, Phys. Rev. B **94**, 064519 (2016).
- [97] M. Silaev, J. Garaud and E. Babaev, *Unconventional thermoelectric effect in superconductors that break time-reversal symmetry*, Phys. Rev. B **92**, 174510 (2015).
- [98] J. Garaud, M. Silaev and E. Babaev, *Thermoelectric signatures of time-reversal symmetry breaking states in multiband superconductors*, Phys. Rev. Lett. **116**, 097002 (2016).
- [99] J. Garaud *et al.*, *Properties of dirty two-band superconductors with repulsive interband interaction: Normal modes, length scales, vortices, and magnetic response*, Phys. Rev. B **98**, 014520 (2018).

- [100] J. Garaud, M. Silaev and E. Babaev, *Microscopically derived multi-component Ginzburg–Landau theories for $s + is$ superconducting state*, Physica C: Superconductivity and its Applications **533**, 63 (2017).
- [101] P. G. Björnsson *et al.*, *Scanning magnetic imaging of Sr_2RuO_4* , Phys. Rev. B **72**, 012504 (2005).
- [102] C. W. Hicks *et al.*, *Limits on superconductivity-related magnetization in Sr_2RuO_4 and $PrOs_4Sb_{12}$ from scanning SQUID microscopy*, Phys. Rev. B **81**, 214501 (2010).
- [103] T. Nishio *et al.*, *Scanning SQUID microscopy of vortex clusters in multiband superconductors*, Phys. Rev. B **81**, 020506 (2010).
- [104] F. Hecht, *New development in FreeFem++*, J. Numer. Math. **20**, 251 (2012).
- [105] D. B. Liarte *et al.*, *Theoretical estimates of maximum fields in superconducting resonant radio frequency cavities: stability theory, disorder, and laminates*, Superconductor Science and Technology **30**, 033002 (2017).
- [106] S. A. Kivelson *et al.*, npj Quantum Mater .
- [107] J. D. Gunton and M. Droz, *Introduction to the theory of metastable and unstable states* (Springer, 1983).
- [108] M. Laine and A. Vuorinen, *Basics of thermal field theory*, Lect. Notes Phys **925**, 1701 (2016).
- [109] J. S. Langer, *Statistical theory of the decay of metastable states*, Annals of Physics **54**, 258 (1969).
- [110] A. Berezhkovskii and V. Y. Zitserman, *Solvent slow-mode influence on chemical reaction dynamics: a multidimensional Kramers-theory treatment*, Chemical physics letters **172**, 235 (1990).
- [111] A. M. Berezhkovskii, V. Y. Zitserman and A. Polimeno, *Numerical test of Kramers reaction rate theory in two dimensions*, The Journal of chemical physics **105**, 6342 (1996).
- [112] H. Jónsson, G. Mills and K. W. Jacobsen, *Nudged elastic band method for finding minimum energy paths of transitions*, (1998).
- [113] G. Henkelman, G. Jóhannesson and H. Jónsson, *Methods for finding saddle points and minimum energy paths*, Theoretical methods in condensed phase chemistry, pp. 269–302, Springer, 2002.
- [114] E. Weinan, W. Ren and E. Vanden-Eijnden, *String method for the study of rare events*, Phys. Rev. B **66**, 052301 (2002).

- [115] T. Qian, W. Ren and P. Sheng, *Current dissipation in thin superconducting wires: A numerical evaluation using the string method*, Phys. Rev. B **72**, 014512 (2005).
- [116] G. Henkelman, B. P. Uberuaga and H. Jónsson, *A climbing image nudged elastic band method for finding saddle points and minimum energy paths*, The Journal of chemical physics **113**, 9901 (2000).
- [117] J. X. Zhu, *Bogoliubov-de Gennes method and its applications* (Springer, 2016).
- [118] E. Blomquist, *Strong Correlation Effects in Bosonic and Fermionic Systems Through an Unbiased Quantum Monte Carlo Approach*, PhD thesis, 2021.
- [119] Y. Nagai, Y. Ota and M. Machida, *Efficient numerical self-consistent mean-field approach for fermionic many-body systems by polynomial expansion on spectral density*, Journal of the Physical Society of Japan **81**, 024710 (2012).
- [120] L. Covaci, F. Peeters and M. Berciu, *Efficient numerical approach to inhomogeneous superconductivity: the Chebyshev-Bogoliubov-de Gennes method*, Phys. Rev. Lett. **105**, 167006 (2010).
- [121] A. Weiße *et al.*, *The kernel polynomial method*, Reviews of modern physics **78**, 275 (2006).
- [122] W. H. Press *et al.*, 1992. numerical recipes in fortran 77: the art of scientific computing, 1986.
- [123] P. De Gennes and E. Guyon, *Superconductivity in "normal" metals*, Phys. Lett. **3** (1963).
- [124] H. Shibata, T. Akazaki and Y. Tokura, *Fabrication of MgB_2 nanowire single-photon detector with meander structure*, Applied Physics Express **6**, 023101 (2013).
- [125] A. Bouhon and M. Sigrist, *Current inversion at the edges of a chiral p -wave superconductor*, Phys. Rev. B **90**, 220511 (2014).
- [126] V. Gasparov, N. Sidorov and I. Zver'Kova, *Two-gap superconductivity in ZrB_{12} : temperature dependence of critical magnetic fields in single crystals*, Phys. Rev. B **73**, 094510 (2006).
- [127] M. Tsindlekht *et al.*, *Tunneling and magnetic characteristics of superconducting ZrB_{12} single crystals*, Phys. Rev. B **69**, 212508 (2004).
- [128] M. Belogolovskii, I. Felner and V. Shaternik, *Zirconium dodecaboride, a novel superconducting material with enhanced surface characteristics*, Boron Rich Solids, pp. 195–206, Springer, 2010.

- [129] R. Khasanov *et al.*, *Anomalous electron-phonon coupling probed on the surface of superconductor ZrB_{12}* , Phys. Rev. B **72**, 224509 (2005).
- [130] H. Fink and W. Joiner, *Surface nucleation and boundary conditions in superconductors*, Phys. Rev. Lett. **23**, 120 (1969).
- [131] R. Lortz *et al.*, *On the origin of the double superconducting transition in overdoped $YBa_2Cu_3O_x$* , Physica C: Superconductivity **434**, 194 (2006).
- [132] E. Janod *et al.*, *Split superconducting transitions in the specific heat and magnetic susceptibility of $YBa_2Cu_3O_x$ versus oxygen content*, Physica C: Superconductivity **216**, 129 (1993).
- [133] I. Khlyustikov, *Critical magnetic field of surface superconductivity in lead*, Journal of Experimental and Theoretical Physics **113**, 1032 (2011).
- [134] I. Khlyustikov, *Surface superconductivity in lead*, Journal of Experimental and Theoretical Physics **122**, 328 (2016).
- [135] I. Mangel *et al.*, *Stiffnessometer: A magnetic-field-free superconducting stiffness meter and its application*, Phys. Rev. B **102**, 024502 (2020).
- [136] V. Ginzburg, *On surface superconductivity*, Phys. Lett. **13** (1964).
- [137] M. A. Müller *et al.*, *Short-time dynamics in $s + is$ -wave superconductor with incipient bands*, Phys. Rev. B **98**, 024522 (2018).
- [138] A. Bouhon and M. Sigrist, *Influence of the domain walls on the Josephson effect in Sr_2RuO_4* , New Journal of Physics **12**, 043031 (2010).
- [139] S. B. Etter, A. Bouhon and M. Sigrist, *Spontaneous surface flux pattern in chiral p -wave superconductors*, Phys. Rev. B **97**, 064510 (2018).
- [140] Y. Tada, W. Nie and M. Oshikawa, *Orbital angular momentum and spectral flow in two-dimensional chiral superfluids*, Phys. Rev. Lett. **114**, 195301 (2015).
- [141] T. H. R. Skyrme, *A unified field theory of mesons and baryons*, Nuclear Physics **31**, 556 (1962).
- [142] D. L. Kovrizhin, B. Douçot and R. Moessner, *Multicomponent Skyrmion Lattices and Their Excitations*, Phys. Rev. Lett. **110**, 186802 (2013).
- [143] Y. Lian and M. O. Goerbig, *Spin-valley skyrmions in graphene at filling factor $\nu = -1$* , Phys. Rev. B **95**, 245428 (2017).
- [144] Y. Akagi *et al.*, *Isolated skyrmions in the CP^2 nonlinear sigma model with a Dzyaloshinskii-Moriya type interaction*, Phys. Rev. D **103**, 065008 (2021).

- [145] H. Zhang *et al.*, $\mathbb{C}P^2$ Skyrmions and Skyrmion Crystals in Realistic Quantum Magnets, arXiv preprint arXiv:2203.15248 (2022).
- [146] Y. Akagi *et al.*, Fractional Skyrmion molecules in a $\mathbb{C}P^{N-1}$ model, Journal of High Energy Physics **2021**, 1 (2021).
- [147] Y. Amari *et al.*, $\mathbb{C}P^2$ Skyrmion Crystals in an $SU(3)$ Magnet with a Generalized Dzyaloshinskii-Moriya Interaction, arXiv preprint arXiv.2204.01476 (2022).

Part II

Scientific Papers

